Vapor Transport Deposition for Perovskite Solar Cells

by

Ella Louise Wassweiler

B.S., University of Iowa (2015)

S.M., Massachusetts Institute of Technology (2019)

Submitted to the Department of Electrical Engineering and Computer Science

In Partial Fulfillment of the Requirements for the Degree of

Doctor of Philosophy

at the

MASSACHUSETTS INSTITUTE OF TECHNOLOGY

February 2023

Author……...…….……

Department of Electrical Engineering and Computer Science

October 25, 2022

Certified by……...……

Vladimir Bulović

Professor of Electrical Engineering and Computer Science

Thesis Supervisor

Accepted by……..……

Leslie A. Kolodziejski

Professor of Electrical Engineering and Computer Science

Chair, Department Committee on Graduate Students

Vapor Transport Deposition for Perovskite Solar Cells
by
Ella Louise Wassweiler
Submitted to the Department of Electrical Engineering and Computer Science
on October 25, 2023 in Partial Fulfillment of the
Requirements for the Degree of
Doctor of Philosophy in Electrical Engineering and Computer Science

Abstract

As perovskite solar cells move closer to commercialization, vapor transport deposition (VTD) has emerged as one of the potential routes for large-scale film growth of photoactive and charge transport layers for these solar cells. As a low-cost alternative to thermal evaporation, VTD has the potential to deposit organic and inorganic perovskite precursor materials either sequentially or via co-deposition. Co-deposition can benefit film formation by increasing the deposition speed and improving film conversion. However, current co-deposition techniques can struggle to produce high quality perovskite films, impacted by challenges associated with the thermal stability of organic precursors and by effectively using the broad deposition parameter space for controlling perovskite film growth.

Here, we use methylammonium lead iodide ($MAPbI_3$) as an archetype perovskite to identify degradation patterns and determine conditions for high-quality film growth. We show that material degradation during sublimation affects methylammonium iodide precursor powders and their contribution to the formation of $MAPbI_3$ films differently than is observed for degradation that is solely due to material transport through a high-temperature zone. By identifying degradation products and film formation, we identify the degradation components that most affect $MAPbI_3$ film performance. With these considerations, we design and construct a custom VTD system for co-deposition of perovskites with a wide range of deposition parameters available for studying film growth and optimizing performance. Additional investigation systematically builds from deposition on glass to an initial demonstration of solar cells. With these results we give recommendations for improved VTD reactor design and a systematic description of conditions that aid in optimization of high-performing VTD perovskite solar cells.

Acknowledgements

A whole host of mentors paved the way to grad school at MIT. Starting with Prof. Phil Cohen at University of Minnesota, who took a chance the summer after my freshman year and let me work in his lab. Other professors at the University of Iowa such as Mona Garvin, Anton Kruger, and David Andersen deepened my understanding of a wide variety of research fields. Prof. Chris Rudell at University of Washington and Prof. Fatima Toor at University of Iowa continue to be mentors even after completing my work in their respective labs.

Thank you to my committee members, Prof.s Jing Kong and Klavs Jensen for their guidance in wrapping up my research into a full story. A massive thank you to Prof. Vladimir Bulovic for being my advisor over these last years and his patience with all the wild ideas I decide to undertake.

I would be remiss if I did not give a massive thank you to my fellow VTD researchers. Especially Anurag Panda, who was my partner in envisioning, designing, and constructing this new VTD system. I learned so much from and with him. I would also like to thank Tamar, who is the next VTD generation researcher. Her excitement for the work and life in general is contagious. Finally, thank you to all the VTD undergrads, including Quentin, Deepta, Thienan, and Deniz.

My Boston/MIT friends made this process so much easier and fun. Melany, thank you for being my first student mentor and friend, who may also have been the only reason I survived the pandemic. Maddie, it has been amazing to start with founding not one, but two different student organizations and to grow that into a friendship. In school, it is always important to have that one sanity check who is outside of the system. Karyn, thank

you for always being my sanity check. Esther, your kindness and honesty was the perfect combination to survive the last experiments of grad school.

My heart has always belonged to Iowa and the friends I found there. Jamie (and little Graham!), Jess, Lauren, and Sarah, thank you all for your excitement and support throughout this entire process.

My family is the one element I can't do anything without. My grandparents since a young age valued education and it's those values that helped propel me to considering grad school. All my aunts, uncles, and cousins have always been the most enthusiastic celebrators and attenders to each milestone. My parents and siblings are there for me day in and day out, no matter the time in our varied time zones. Martha and Joe not only take time to do the fun things (like go to Nova Scotia for a week) but also to help with the hard things. My parents do the impossible every day by encouraging and supporting all of us. They inspire and empower me every day.

Finishing my PhD wouldn't have been possible without my family and friends. You all carried me across the finish line and for that I am forever grateful.

Table of Contents

Figure List

Equation List

Table List

Introduction

Factors such as climate change[1,2], energy security[3,4], and economics[5] drive the shift from fossil fuels to renewable energy[6]. One of the main renewable technologies is solar due to its current market share and equitable distribution around the globe[7]. However, current applications can be limited because the dominant technology, silicon (Si) solar panels, are heavy and inflexible. Flexible technologies such as cadmium telluride (CdTe)[8] are inexpensive to produce but lower in efficiency than Si panels. Expanding flexible, lightweight, and cost-effective solar panel technology would expand the potential commercial markets[9,10] and allow for a more rapid scale-up to an even larger market share.

One potential technology that can be deposited on flexible and lightweight substrates is organic-inorganic halide perovskites. As organic-inorganic halide perovskite solar cells reach power conversion efficiencies comparable to those of current market technology[11], researchers have begun investigating how to deposit perovskite solar cells over larger areas for manufacturing[12–14].

One technique under investigation, vapor-processing, is already a familiar technology to solar cell manufacturers in CdTe and organic optoelectronic lines[15,16]. Vapor-based deposition allows for precise film thickness control and does not require hazardous solvents, enabling fabrication of complex, multi-layer device structures. Additionally, vapor deposition is conformal, allowing perovskite films to be fabricated on rough surfaces. This benefit is leveraged in tandem technologies, in which a conformal perovskite film is deposited on top of a textured silicon substrate through a vapor-processed base coat later converted to perovskite[17–19].

Although record efficiencies in research-scale perovskite solar cells have been achieved with solution-processed films, these devices are made through spin-coating which is not a scalable process. Vapor-deposited and solution-deposited perovskite solar cells reach similar efficiencies when fabricated using scalable, manufacturing-compatible techniques[20–22].

A variety of vapor-based deposition techniques have been used to produce perovskite solar cells, including thermal evaporation[22,23], flash evaporation[24], close-space sublimation[25], and variations in hybrid deposition[26,27]. However, the most efficient vapor-deposited perovskite solar cells make use of a thermally evaporated perovskite layer and have attained device efficiencies 24.1%[22]. While most papers describe a co-deposition process with two separate precursors, triple cation devices with more sources have also been demonstrated[28]. Recent advances in large area deposition increase the achievable active areas of these devices to $4cm^2$ and initiate development of mini-modules[29]. Thermally evaporated perovskite solar cells were also the first technique to achieve all-vacuum-processed device layers[30]. Although favored for its ability to produce high-efficiency perovskite solar cells using established manufacturing practices, thermal evaporation is a slow deposition technique (0.1-10 A/s) with less than 50% of the precursor material depositing into the film[31].

Another popular technique in literature is called hybrid chemical vapor deposition (CVD). In this process, an underlying lead halide film is deposited by either solution or vacuum-based methods. The film is then converted to perovskite in a CVD chamber using either methylammonium iodide (MAI) or formamidinium iodide (FAI) as the organic cation source. This technique has produced large-area solar cells up to $22.8cm^2$ [32]. However, the cost-effectiveness of hybrid CVD on a manufacturing line is questionable since transitions

between ambient and vacuum require additional infrastructure and processing time, which increases the cost and decreases the speed of manufacturing[15,16].

VTD uses a carrier gas to transfer sublimed material from source to substrate. The material deposition rate for VTD (driven by the carrier gas flow) is decoupled from material temperature, allowing for orders of magnitude higher deposition rates and material utilization when compared to thermal evaporation. Device fabrication by VTD also allows for independent control of both chamber pressure and the resulting crystallization kinetics of the perovskite film. VTD is performed solely under vacuum so avoids the manufacturing difficulties associated with hybrid CVD.

In this thesis, we focus on VTD systems for the development of co-deposition of perovskite films for solar cells. To this end, we investigate the potential degradation mechanisms for the organic precursors and their interaction with inorganic precursors. We design and construct a co-deposition VTD system to be compatible with a wide range of deposition parameters. With this system, we independently study the deposition of MAI and PbI_2 precursors and then combine to grow co-depositional perovskite films. Finally, we study film growth on different substrates and provide an initial demonstration of solar cells.

1. Fundamentals of Vacuum-Based Deposition

Thin film manufacturing combines film deposition at high rates with precise control over film quality. Researchers and engineers are continuously pushing the boundaries of deposition technologies and compatible materials. Historically, industrial deposition techniques, such as evaporation and close-space sublimation, have been applied to new sets of materials and applications.

The techniques used for vapor deposition can be broken down into two general categories: physical vapor deposition and chemical vapor deposition. Physical vapor deposition (PVD) transports a precursor material under vacuum to form a thin film on a substrate. Typical PVD techniques include sputtering, thermal evaporation, and electron-beam evaporation. In contrast, chemical vapor deposition (CVD) relies on a single or series of chemical reactions under vacuum to form a thin film on a substrate. While most CVD processes are referred to as CVD, other common techniques include atomic layer deposition (ALD), close-space sublimation (CSS), and metal-organic (MOCVD), among others. However, deposition of perovskites under vacuum challenges the notion of a strict PVD or CVD process. Hence, the term vapor transport deposition (VTD) is used. In VTD, precursor materials are sublimed at individualized, optimal temperatures and a heated carrier gas is used to transport the material from source to chilled substrate. While the deposition of a precursor on a substrate fits the PVD description, when depositing two or more precursors at the same time, the formation energy for perovskite is so low that the precursors will form a perovskite film on the substrate, which is more CVD-like.

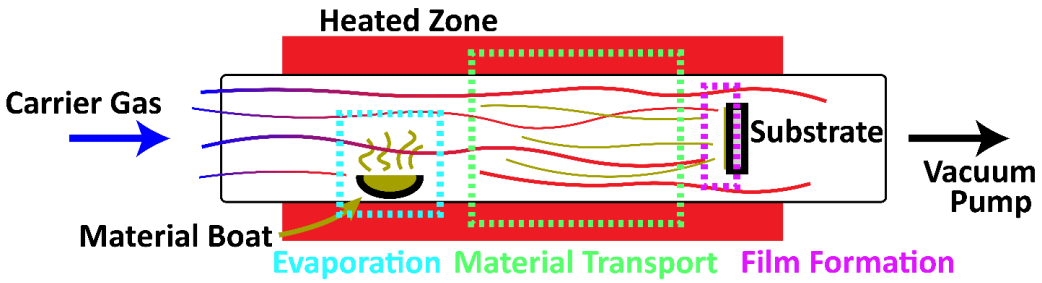

Figure 1. A VTD deposition process broken down into three main components; evaporation (blue), material transport (green), and film formation (purple).

Therefore, when we build a description of vacuum systems that can be applied to VTD, we may draw from many deposition fields depending on the situation. In general, vapor deposition can be divided into three major steps: evaporation, material transport, and film formation. We will devote a general section to each. Then, in Chapter 4, we will discuss these fundamentals as they apply to the VTD chamber used in the rest of the thesis.

1.1 Evaporation/Sublimation

The starting point of VTD is precursor sublimation into a hot carrier gas stream. Sublimation or evaporation of precursor materials has been extensively studied for thermal evaporation systems, which in this regard are very similar to VTD systems. Since in thermal evaporation the dominant mechanism of material transport is line-of-sight ballistic transport, the evaporation rate has direct influence on the film growth rate.

The evaporation rate itself is frequently described through the Hertz-Knudsen equation:

$$\frac{r_{evap}}{A_{eff}} = \alpha \frac{P_{mat}^{sat} - P_{cell}}{\sqrt{2\pi M R T_{mat}}}$$

Equation 1. Hertz-Knudsen Equation.

Where:

r_{evap} (mol/s) is the evaporation rate

A_{eff} (m^2) is the effective surface area of the precursor material

P_{mat}^{sat} (Pa) is the saturation pressure of precursor material

P_{cell} (Pa) is the pressure of the chamber

M (kg/mol) is the precursor's molar mass

T_{mat} (K) is the precursor temperature

The term α refers to the re-adsorption probability of the sublimed precursor and can be thought of as an evaporation efficiency term. It is greatly influenced by the type of boat used in the evaporation process. In a Langmuir evaporation process the precursor is evaporated from an open-source boat while in effusion processes the precursor is confined within the boat and released through a small hole. Knudsen cells and baffled boats make use of effusion in order to drive the α term to 1. Limitations to the Hertz-Knudsen equation come from errors induced by using simplified empirical coefficients within the re-adsorption probability parameter. Increased accuracy can be found through coupling the Hertz-Knudsen equation with statistical rate theory as shown by Persad *et al*[3].

Variations in boat design are driven by the type of precursor material used. Two common but distinct classes of evaporated materials are metals and organic compounds. For metals, open-source boats are used as metals are melted down and evaporated onto the substrate in a Langmuir evaporation process. However, organic compounds and other materials with low partial pressure use Knudsen cells or baffled boats to more tightly control the precursor temperature and resulting evaporation rate.

While the Hertz-Knudsen equation is a good place to start, theories surrounding thermal evaporation do not fully describe processes within VTD. Although precursor sublimation is where the process starts, now it needs to enter a heated carrier gas and the resulting transport mechanism is much different than thermal evaporation. Looking to equations

derived for organic vapor phase deposition (OVPD)[31], a modified version of the Hertz-Knudsen equation describes the influence of the hot carrier gas and gives the complete equation for the output from the precursor source section:

$$r_{out} = \frac{P_o \exp\left(\frac{-\Delta H_{vap}}{RT}\right)}{\frac{\alpha A_{eff} RT}{\bar{V}} + \sqrt{2\pi M R T_{mat}}}$$

Equation 2. Modified Hertz-Knudsen Equation using the Clausius-Clapeyron Relation.

Where the numerator term is the Clausius-Clapeyron relation which describes the liquid/solid transition to gas on a material's phase diagram. As this equation has also been derived in the OVPD field, its complete derivation here is found in Appendix A.

Techniques with both a carrier gas and a source cell temperature define growth regimes to describe influences to material flux. Growth rates can either be limited by the evaporation rate (called kinetic), by the reaction rate on the substrate surface, or by the carrier gas flow rate (called equilibrium or mass-transport controlled)[34]. Commonly, vacuum designers work to develop processes within the equilibrium regime although some notable alternative examples will be discussed in Chapter 4.

1.2 Material Transport

Full careers are dedicated to studying material transport in specific types of deposition techniques. As VTD for perovskites is a novel approach, we will only briefly review the fundamental underlying processes used and let future VTD engineers further expand the field.

1.2.a Definitions and Assumptions

Material transport as a field has a rich and deep history and understanding. Therefore, in order to discuss material transport as it pertains to VTD in a clear and straightforward manner, we need to first define a couple of assumptions about a hypothetical system that we will use through the entirety of the thesis. The basic assumptions and definitions at the beginning of any material transport problem are often as follows:

- *System Geometry:* Simplifies equations and the calculations of constants. We will assume a **cylindrical geometry** for all discussions.
- *Reynolds Number:* Defines the fluid flow regime of a system. In particular, systems can be dominated by laminar or turbulent flow regimes. In a laminar flow regime all particle within a fluid are flowing in the same direction. In contrast, a turbulent flow regime is defined by particles moving in irregular motions. The onset of turbulent flow is defined by the Reynolds Number which is (for a cylindrical system):

$$Reynolds\ Number = \frac{(Mass\ Density) * (Cross\ Section\ Mean\ Fluid\ Velocity) * (Diameter)}{Viscosity}$$

Equation 3. Reynold's Number Calculation.

If the Reynolds Number is greater than 2,300 the system is transitioning and/or in turbulent flow. For our discussions, we will use the **laminar flow regime** and assume we can design a system to fit this description.

- *Compressible Flow:* Defined by fluid flow that allows for changes in gas density throughout a system. The Mach Number defines whether the gas is in a compressible regime or not, and is defined by:

$$Mach\ Number = \sqrt{(Specific\ Heat\ Ratio) * (Gas\ Constant) * (Temperature)}$$

Compressible if $velocity > Mach\ Number * 0.3$

Equation 4. Mach Number Calculation

We will once again assume we can design a system that operates with an **incompressible flow**.

- *Knudsen Number:* Defined as a ratio of the mean free path to the physical length scale. If molecules are traveling a mean free path close to the physical length scale of the system then statistical mechanics must be used. In most VTD systems we can safely assume fluid **continuity**.

$$Knudsen\ Number = \frac{Mean\ Free\ Path}{Representative\ Physical\ Length}$$

Equation 5. Knudsen Number Calculation.

- *Flow Independent of Time:* We will perform all of our analysis at steady state and assume a **flow independent of time**, except where noted.
- *Precursor Concentration:* In VTD systems a carrier gas is used to transport precursor materials from source to substrate. The relative amount of each type of molecule in the system could influence interactions and fundamental properties of the system itself. As we design systems to be in the equilibrium regime the carrier gas flow rate is much larger than the evaporation rate and the system is in a **dilute precursor concentration** regime.
- *Prandtl Number:* Approximates the ratio of momentum diffusivity to thermal diffusivity. In vacuum systems it helps to define heat transfer when a carrier gas is present.

$$Prandtl\ Number = \frac{(Specific\ Heat\ at\ Constant\ Pressure) * (Viscosity)}{Thermal\ Conductivity}$$

Equation 6. Prandtl Number Calculation.

- *Péclet Number:* It is a ratio of the precursor diffusion to the convection of that precursor.

$$Péclet\ Number = (Reynold's\ Number) * (Prandtl\ Number)$$

Equation 7. Péclet Number Calculation.

With these fundamental assumptions and definitions, we are ready to probe the three main parts of material transport: momentum, energy, and mass.

1.2.b Momentum

The Law of Conservation of Momentum states that momentum is neither created nor destroyed except through the input of force. Momentum in a VTD system primarily comes from carrier gas movement, since we assume dilute precursor material contributions. That means the primary momentum transport is through convection momentum transport which is described by the bulk flow of fluid.

An important point of consideration for a carrier gas-based system is the length required for the carrier gas flow to become steady across the diameter of the system. This length is defined by the hydrodynamic entry length and follows the equation:

$$Hydrodynamic\ Entry\ Length = (0.05) * (Reynolds\ Number) * (Tube\ Diameter)$$

Equation 8. Hydrodynamic Entry Length Calculation.

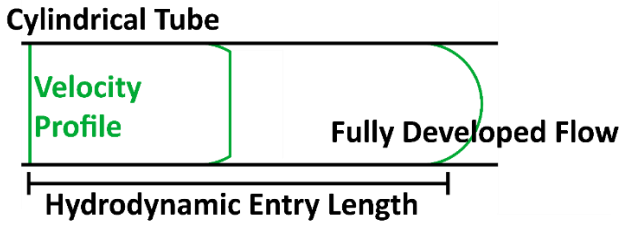

Figure 2. Diagram of a gas input advancing into a fully developed flow and the resulting hydrodynamic entry length.

Figure 2 demonstrates how a gas stream input become a fully developed flow at a certain distance within a cylindrical chamber. Once in fully developed flow, the gas would interact evenly with a perpendicular substrate and is therefore desirable. Determining the length required to enter fully developed flow depends on the Reynolds Number (Equation 3) which accounts for the gas velocity and type. Understanding the concept of an entry length and the influential parameters is a good starting step for the two other components of mass transport.

1.2.c Energy

Energy within a vacuum system, especially a VTD system, comes from thermal sources. Therefore, similar to the Law of Conservation of Momentum, a reactor can be analyzed via the First Law of Thermodynamics – energy can neither be created nor destroyed. Accordingly, it is useful to study how heat is transferred through conductive, convective, and radiative methods. In conduction, heat diffuses through a single medium. In convection, heat is transferred between a solid and a moving fluid. Finally, radiation is heat transferred via electromagnetic waves.

Within each type are subdivisions which further help to analyze thermodynamic systems:

A. In convection, customarily there are two different broad classes defined, one pertaining to the bulk transfer of heat due to fluid motion, called advection, and the

other due to diffusion of materials which is called convection. In CVD or VTD systems this is forced convection because of the use of mass flow controllers and vacuum pumps to drive the gas flow. Our system also contains both latent (causing phase changes) and sensible (material's internal thermal energy) heat transfers.

B. Radiation occurs most effectively within a vacuum, however gasses are considered transparent to its effects. Therefore, radiative heat transfer is most frequently used for heating of substrates or other surfaces within a vacuum, not the carrier gas as is necessary in most CVD or VTD systems where the substrates need to be actively cooled not heated.

Looking at a standard CVD or VTD system we find a variety of heat transfers that occur as shown in Figure 3.

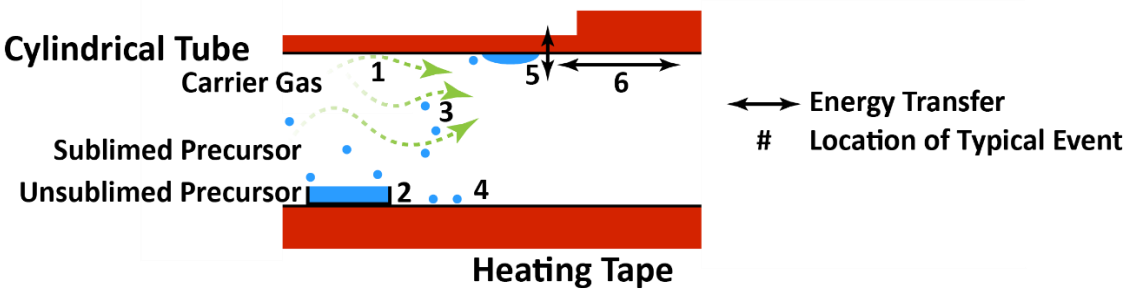

Figure 3. Highlighting the different forms of heat transfer within a CVD/VTD chamber with a precursor boat.

1. Convective heat transfer from cylindrical tube to carrier gas.
2. Conductive heat transfer from cylindrical tube to precursor boat causing sublimation of the precursor.
3. Conductive heat transfer from carrier gas to sublimed precursor material.
4. Convective heat transfer from cylindrical tube to sublimed precursor material.

5. Convective heat transfer from colder cylindrical tube to precursor material, causing parasitic deposition on the cylindrical tube.
6. Conductive heat transfer from a region of higher temperature to lower temperature on the cylindrical tube.

Each of these heat transfer events dramatically shift the deposition process and a couple in particular are important in the initial vacuum system design. Example 5 (Figure 3) demonstrates how parasitic deposition occurs on the chamber's sidewalls. In contrast, examples 1-3 are desired processes for VTD film growth.

If we look deeper into these desired processes, we find that similar to momentum transfer, thermal entry lengths can be defined by the equation:

$$Thermal\ Entry\ Length = (0.05) * (Reynolds\ Number) * (Prandtl\ Number) * (Tube\ Diameter)$$

Equation 9. Thermal Entry Length Calculation.

The thermal entry length corresponds to the distance required to form a complete thermal boundary layer with a flowing gas. However, an additional consideration for vacuum systems with a carrier gas is the heating of that gas to deposition temperature before interaction with the precursor. This length can be found by an expanded form of Newton's Law of Cooling rearranged to focus on the tube length[35]:

$$L = -\frac{(\dot{m}) * (c_p)}{(\overline{U}) * \left(2 * \pi * \left(\frac{D}{2}\right)\right)} * \ln\left(\frac{T_x - T_{out}}{T_x - T_{in}}\right)$$

Equation 10. Calculation for the Length Required to Heat a Gas Under Vacuum.

Where:

T_x (K) is the temperature at a point within the tube

T_{in} (K) is the temperature at the inlet

T_{out} (K) is the temperature at the outlet

$\overline{U}$ ($\frac{\mathrm{W}}{\mathrm{m^2K}}$) average convection heat transfer coefficient

$\dot{m}$ $\left(\frac{kg}{s^3}\right)$is the mass flow rate

c_p $\left(\frac{J}{kg*K}\right)$ is the specific heat at constant pressure

D (m) is the diameter of the tube

L (m) is the length of tube

From this we get a logarithmic curve as the tube temperature goes to the deposition temperature which then can be used to further design a vacuum system carrier gas inlet. However, if we want to examine how deposition parameters influence the length required to heat the carrier gas, we need to first define when the gas has reached its target temperature (where the natural log has converged). The average overall heat transfer coefficient for this system can be assumed to be the heat transfer coefficient of stainless steel or quartz to the carrier gas at the deposition pressure.

Using these concepts, a VTD, or more generally a CVD, reactor can be designed for a specific precursor or set of precursors.

1.2.d Mass

To round out the discussion of material transport, we end with the Law of Conservation of Mass – that mass, similar to momentum and energy, can neither be created nor destroyed. From this comes the mass balance equation, determining for a defined area the movement of molecules in and out and chemical reactions combining/disassociating

new molecules. In its simplest form, we can think of the flux of material A through material B in a single direction (y) as[36]:

$$N_A = -cD_{AB}\frac{\partial x_A}{\partial y} + x_A(N_A + N_B)$$

Equation 11. Equation for the Flux of Material A through Material B.

Where:

N_A $\left(\frac{mol}{cm^2 * s}\right)$ is the flux of material A

N_B $\left(\frac{mol}{cm^2 * s}\right)$ is the flux of material B

c $\left(\frac{mol}{m^3}\right)$ is the molar concentration of precursor A

D_{AB} $\left(\frac{m^2}{s}\right)$ is the diffusivity of precursor A through B

$\frac{\partial x_A}{\partial y}$ is the change in concentration of precursor A as a function of location

x_A $\left(\frac{mol}{cm^2}\right)$ is the concentration of precursor A at a given location

The first term in blue corresponds to the molecular flux and the second term in red to the convective flux. The molecular flux is the flow of material is due to diffusion while in contrast the convective flux is the flow of material due to the bulk motion of the second component (material B in this case). Therefore, the flow of material in these vacuum systems are dependent on both the energy of the system and the momentum as described in previous sections.

Specifically, for many vacuum depositions using a carrier gas, researchers study uniformity and precursor flow in a laminar flow regime through Taylor Dispersions. In these style studies, investigators pulse a single precursor in a reactor tube and examine what happens after. Researchers study the axial (along the direction of motion) and radial (perpendicular to the direction of motion) motion of precursors[37].

In his studies, Taylor defined an equation that can be used to determine the precursor waveform after an initial pulse[38]:

$$\langle \rho_A \rangle = \frac{m_A}{2\pi R^2 \sqrt{\pi K t}} e^{-\frac{(z-\langle v_z \rangle t)^2}{4Kt}}$$

Equation 12. Taylor's Equation for the Precursor Waveform

Where:

$\rho_A \left(\frac{kg}{m^3}\right)$ is density of precursor A

$m_A \ (kg)$ is the mass of precursor A

$R \ (m)$ is the radius of the tube

$K \left(\frac{m^2}{s}\right)$ is the axial dispersion coefficient

$t \ (s)$ is time

$z \left(\frac{m}{s}\right)$ is the specific velocity at that area along the length of the tube

$v_z \left(\frac{m}{s}\right)$ is the average velocity along the length of the tube

With this equation, the velocity changes to the initial pulse of precursor A can be tracked, as well as experimentally deriving the diffusion coefficient as a subcomponent of the axial dispersion coefficient.

As in extension Aris continued to expand Taylor's equations and found molecular diffusion enhances axial dispersion for small Péclet numbers and inhibits at larger numbers[39]. Many others have continued to build on Taylor's findings to more thoroughly explain phenomena[40,41] and to build specific solutions for different materials[42].

With multicomponent systems, as in the case of more than one precursor and a carrier gas, these equations are expanded as more than one term is needed to explain the presence of an additional precursor.

Particularly in the perovskite field, methods for controlling MAI during evaporation are heavily debated[43]. Some argue to control via the partial pressure[44] and others assert that using a quartz crystal monitor[45] is the most reproducible method. The origin of this debate may be due to the unknown behavior of sublimed MAI under vacuum. It remains unknown whether MAI sublimes as one molecule or if deposition conditions influence its sublimation chemistry. Additionally, it is unknown if MAI interacts with PbI_2 in vacuum or in an inert gas stream. These uncertainties challenge the notion of optimizing deposition conditions since no one knows exactly for what process we are optimizing conditions. Further research is critical to truly understanding these precursors, and as a result, gaining systematic control in a co-deposition process.

1.3 Film Growth

The simplest way to think of film growth is it occurs wherever the precursor goes from the gas phase to the solid phase. Transitions from one phase to another are often defined through a phase diagram. Defining how these transitions are controlled can be described through the Gibbs Phase Rule:

$$Degree\ of\ Freedom = Components - Phases + 2$$

Equation 13. Gibbs' Phase Rule.

Degrees of freedom correspond to the number of variables that can be used to control the number of phases present. In crystal growth the Gibbs Phase Rule holds if the growth process is slow enough for the system to be close to equilibrium and if the user has

enough knowledge about the chemical reactions in the system to define them accurately[46].

For example, in $MAPbI_3$ perovskites with no gas-based interactions or intermediate phases around the surface of the substrate, there are three components and two phases. Therefore, the number of degrees of freedom of the system is three, meaning three different variables can be used to control the system. In this example, the three variables are likely pressure, temperature, and composition.

A complicating factor to phase diagrams occurs when two or more component mixtures contain materials with very different vapor pressures. In this case, the phase diagram becomes much more complex as composition and phase of components change greatly with small changes in variables.

Knowing the limiting factor in the film growth rate can help to illuminate which deposition parameters will be most influential. The three main options are thermodynamics (limited by temperatures within the system), mass transport (limited by reaction rate), or surface kinetics (limited by surface properties). For example, if the system is in a surface kinetics growth limiting state, changing the surface orientation of the substrate would influence the film growth rate.

In VTD systems, the location of film growth is determined by both hydrodynamic and thermodynamic forces. Similar to the situations presented previously, a hydrodynamic boundary layer is formed on the substrate surface depending on the specific orientation of the substrate. An additional thermal boundary layer develops as both diffusive and convective forces further highlight the desired film growth region.

Film growth is commonly launched through nucleation where small clusters of solid cause the initial transition point between gas to solid on a surface. This effect was initially described by Classical Nucleation Theory. For this transition to occur, it has to be thermodynamically favored, which in CVD processes is frequently purposefully set up through a temperature gradient to induce a chemical potential by chilling the substrate. The temperature gradient causes thermodynamic supersaturation which is the nucleation driving force. Additionally, it is important to note that the two phases do not have a strict interface, rather, the interface bonding is weaker than in the bulk crystal and as a result requires energy to form.

Where nucleation occurs is described by the Gibbs Free Energy which helps to define an activation energy required for nuclei to form on the substrate's surface. It characterizes the system energy that can be added or removed without becoming an irreversible process. In this understanding, while low energy states are favored, it is also understood that even when a material is physically on the substrate's surface there is still energy required to be incorporated into the crystal lattice before reaching the lowest state. Only when those conditions are satisfied do you get nucleation and film growth.

While Classical Nucleation Theory is a good place to start when discussing film growth, it has some significant drawbacks such as using macroscopic quantities and observations to describe atomic processes. However, from there others have gone on to define different growth modes (Frank-van der Merve, Volmer-Weber, Stranski-Krastanov, etc.) and general nucleation processes (Ostwald Ripening, etc.) that are studied in many different materials to this day[47,48].

Applying this understanding to a basic PVD process, thermal evaporation, it can be shown just how complicated and material specific growth under vacuum can be on an atom-by-

atom understanding. Since thermal evaporation is a line-of-sight process, the material flux on the surface can be thought of as having a normal incidence. These atoms are coming in with a certain amount of thermal and kinetic energy and once they impact the surface they can reflect, diffuse across the surface, or remain in that spot. Once on the surface but still yet to be fully incorporated into the film they are known as adatoms. Similarly, vacancies on the surface of a film are known as advacancies. Different deposition parameters (such as substrate heating) can influence the amount of energy which these adatoms have on the substrate and thus the likelihood of diffusion and resulting crystallinity of the film.

At this time, the nucleation processes and growth modes for solar perovskite materials under vacuum is relatively unknown. Much care has been taken to determine the sticking coefficients[43,49] and influence of parameters such as substrate[44,50,51] but the nucleation process and controlling that process remains elusive.

1.4 Conclusion

Much of the fundamental deposition processes, from sublimation to material transport to film growth, remain unknown for perovskites. Nonetheless, researchers have grown films to great solar cell performance while slowly building on the foundation of physics principles that guide perovskite material control under vacuum. This chapter serves to illustrate those fundamentals while highlighting the areas in need of further research. Moving forward, we will use these fundamentals to design a co-deposition VTD system and deposit our first perovskite films.

1.5 Further Reading

These textbooks were instrumental in the preparation of this chapter and provide further information on the concepts presented.

Fundamentals of Heat and Mass Transfer

Bergman, T., Lavine, A., Incropera, F. & Dewitt, D. *Fundamentals of Heat and Mass Transfer*. (John Wiley and Sons Inc, 2011).

The Handbook of Crystal Growth

Handbook of Crystal Growth. (Elsevier B.V., 2015).

Organometallic Vapor-Phase Epitaxy

Stringfellow, G. *Organometallic Vapor-Phase Epitaxy*. (Academic Press Inc., 1999).

Transport Phenomena

Bird, R. B., Stewart, W. & Lightfoot, E. *Transport Phenomena*. (John Wiley and Sons Inc, 2007).

2. Flexible, Lightweight Solar Cells – From Films to Devices

Many different types of materials have been used for optoelectronics, and specifically solar cells. Some use thick, rigid, crystalline semiconductors such as GaAs or Si. Others use a wide-ranging class of solar materials within thin, flexible films that include CdTe[52], organics[53,54], quantum dots (QDs)[55,56], dye-sensitized, and perovskites[11]. Even with such a broad range of materials that can be used in solar applications, there are a few fundamental physics principles that connect them all. In this chapter we will start by discussing the basic principles of both solar films and devices, then move on to discussing how perovskites fit within those principles.

2.1 Film Operation is Key to Successful Solar Cell Operation

Fundamentally, solar cells work by absorbing sunlight to generate electricity. In order to make a good solar cell we need to generate charges through absorbing sunlight and then extract those charges to the electrical contacts. To do this, we need to use a series of optimized materials that have different functions during each step in the process.

2.1.a Basics of Electronic Materials

Carriers within a material are made of both electrons and holes (absence of electrons). Current is the movement of electrons and holes in opposite directions within a material. Depending on material properties, electrons, and holes, even as linked as they are defined, need to be treated differently. There are three fundamental types of electronic materials, conductors (lowest resistance to the movement of carriers), insulators (highest resistance to the movement of carriers), and semiconductors (intermediate resistance to carrier movement).

Semiconductors are defined by their density of states, or the allowed energy levels that carriers can occupy within the electronic structure. In order to be a semiconductor, these materials must have a bandgap, or a region where no electronic states can be found. The shallower energy levels above the bandgap are known as the conduction band and the deeper energy levels below the bandgap are known as the valence band. Within semiconductors there are intrinsic materials (equal concentrations of electrons and holes), p-type materials (dominated by holes), and n-type materials (dominated by electrons). The Fermi level shows where the doping level moves the energetic bands within the base material. With these key concepts in mind, we can start to build a picture of the physics behind solar cells.

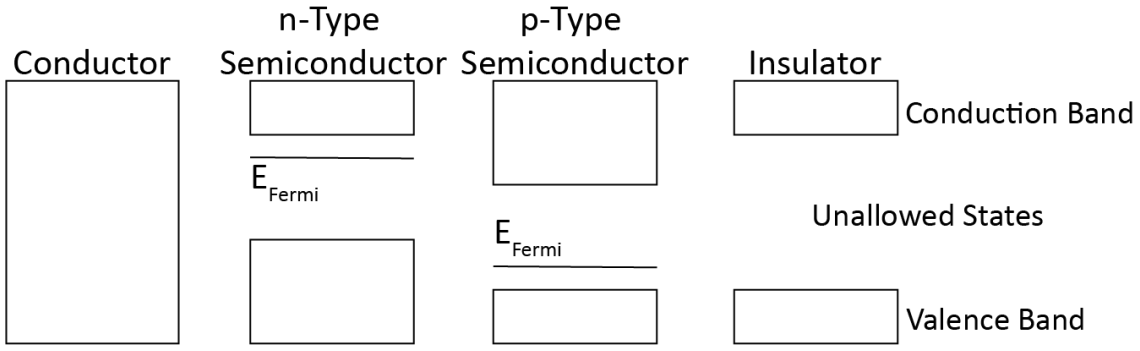

Figure 4. Band structure of different types of electronic materials.

2.1.b Absorption

One key characteristic of solar materials is the ability to absorb sunlight and generate carriers as a result. Sunlight is a broad spectrum of different wavelengths of light that correspond to different photon energies. For a semiconductor to absorb a certain wavelength the bandgap of the material needs to be smaller in energy than the wavelength of light. For example, in Figure 5 we show the wavelengths corresponding to AM1.5 sunlight. Three different solar absorber materials are pointed out, with their

respective bandgap energies are converted into wavelengths. Each material can absorb wavelengths below their respective bandgap wavelengths.

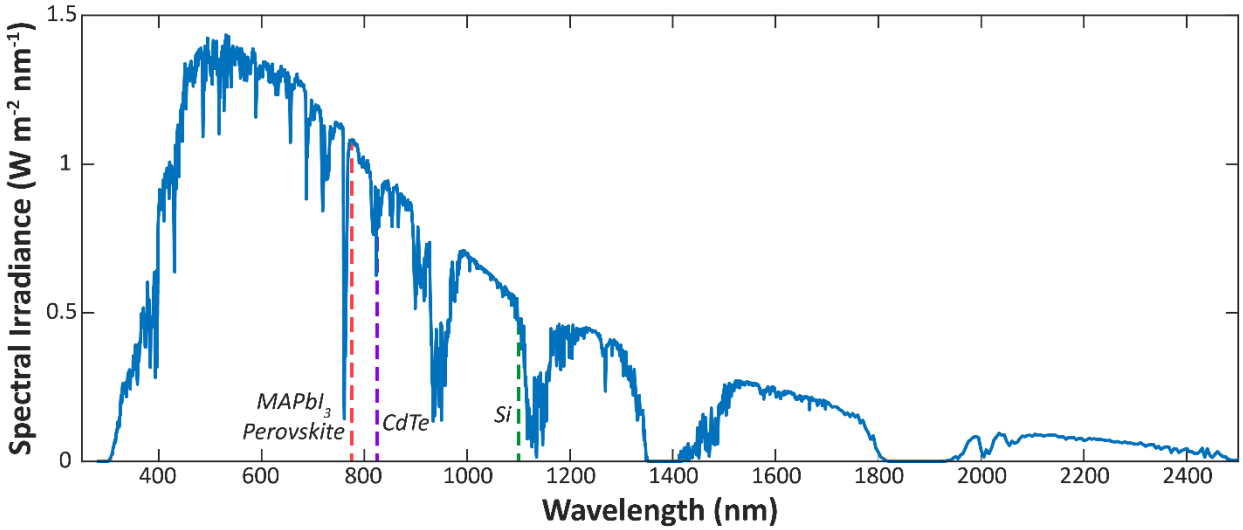

Figure 5. The standard wavelengths of light incident upon the earth. The bandgap of typical solar materials is also highlighted.

In this simplistic picture, it seems that all solar absorbing materials should target bandgaps well above the energy in sunlight. However, in these materials there is a tradeoff between absorbing sunlight and extracting the carriers, further described by the Shockley-Quiesser Limit. For example, smaller bandgap solar cells absorb more light but larger bandgap solar cells attain greater voltages. Therefore, there is a balance in order to achieve and overall high efficiency. Nevertheless, some solar cell architectures play with multiple bandgap materials to absorb and extract more carriers from sunlight[57–59].

2.1.c Recombination

Solar materials absorb sunlight which sends an electron from the valence band to the conduction band thus additionally freeing a hole in the conduction band. These carriers need to be extracted from the absorber material before they recombine in order to generate power from the device. Other optoelectronic materials, such as in LEDs, use radiative recombination to generate light. Radiative recombination is when an electron

from the valence band directly recombines with a hole from the conduction band. However, other types of unwanted recombination methods exist, such as non-radiative recombination which adds thermalization losses to optoelectronic devices or defect-based recombination where intermediate states in the bandgap are added by defects in the crystal lattice. These unwanted types of recombination lower the efficiency of devices and are symptomatic of flaws within the deposited solar material. As a result, oftentimes researchers measure carrier lifetimes in films to analyze their potential within a solar cell.

2.1.d Perovskite as a Solar Material

In general, any bulk material can be classified as amorphous (without an underlying repeating structure) or crystalline (with a definable repeating structure). Perovskite is actually a general crystalline structure defined as ABX_3. Therefore, there are a wide variety of atoms or compounds that can be placed in the A, B, and X sites with varying degrees of stability[60]. Previous to discovering the optoelectronic variety, perovskites were a rich field focusing on versions with oxygen in the X site, termed perovskite oxides. Perovskite oxides found interest in the scientific community due to physical properties such as ferroelectricity, superconductivity, ferromagnetism, and insulator-to-metal transitions depending on the subtype[61]. As a result, perovskite oxides have been used as catalysts in a wide range of chemistry research for energy development[62], gas sensors[63], batteries, and fuel cells[64].

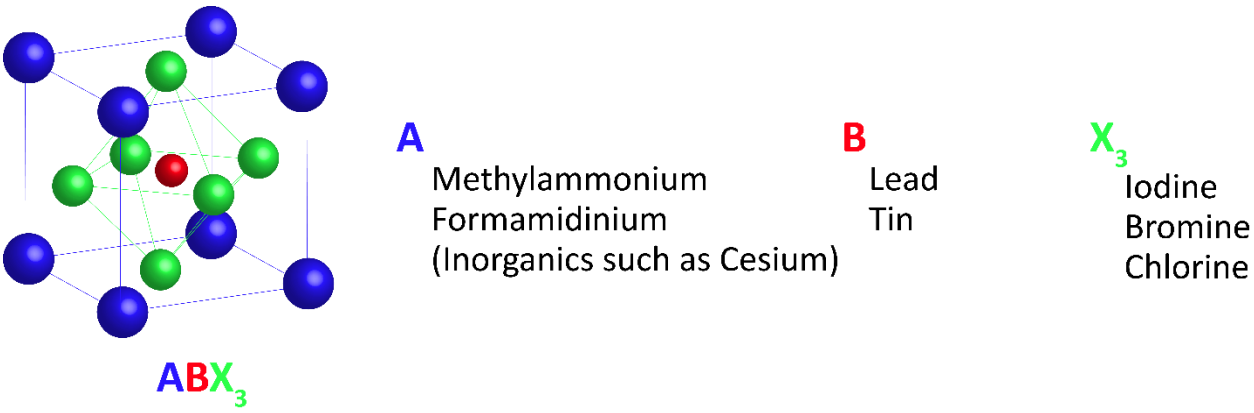

Figure 6. The crystalline structure of perovskites along with typical molecules found at the different lattice sites.

The perovskite variations used in solar applications are noteworthy for their high light absorption and carrier properties. While metal-organic varieties are most popular, all-inorganic[65–67] and Sn-based perovskites[68,69] are noteworthy for their potential stability and non-toxicity respectively. In all cases, perovskites are grown using either solvents or vacuum processes. Therefore, different crystal phases appear in the films, creating significant grain boundaries that can be the centers for defects to inhibit carrier movement. The growth of optimized crystal phases and grain boundaries has significant implications for both device efficiency in promoting carrier lifetimes and stability[70]. Understanding how processing conditions influence crystal phase and grain boundaries helps researchers to understand how to control defects for optimized films[71,72].

2.2 Basics of Solar Cell Operation

Electrical devices are defined by how the electrical carriers within them behave. Optoelectronic devices are those whose electrical carriers are greatly influenced by optical elements such as illumination or emitting light. Most electrical devices perform rather complex operations, for example, solar cells take incoming light, translate that light into carriers, and remove those carriers from the device (which is termed electricity). In order to perform these complex operations, oftentimes there needs to be more than one

material within an electrical device. The energetics of carriers behaving within electrical devices are defined by band diagrams.

2.2.a Band Diagrams

In many electrical device discussions, the simplest version given is the P-N Junction. In a P-N junction there is one material that is N-type directly connected to another material that is P-type as shown in Figure 7.

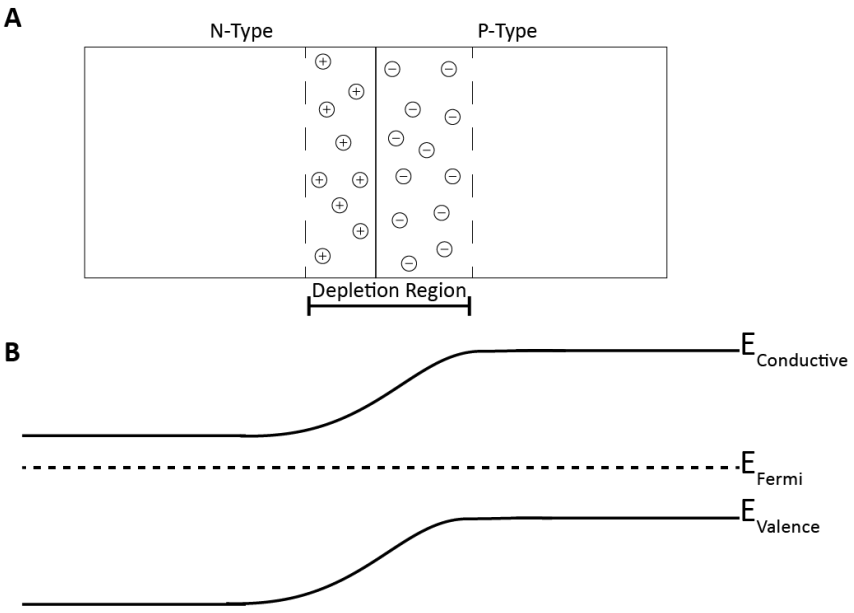

Figure 7. The physical representation and band diagram of a P-N junction. A. A physical description of the junction caused by placing a N-Type material in contact with a P-Type material. Included is the Depletion Region which is defined by the diffusion of majority carriers. B. The band diagram resulting from placing the N-Type and P-Type material in contact. In the absence of an external voltage, the Fermi level must be constant.

Connecting a material with an excess of electrons to one with an excess of holes will cause diffusion of these majority carriers from one side of the junction to the other. This diffusion sets up an electric field across the junction where the width is referred to as the depletion region. Another way to look at the connection is through the energy band diagrams. When two different materials connect the Fermi level must be flat since the majority

carriers will diffuse into the depletion region. This causes shifts in the band diagrams of the two materials at the junction, which is another way to visualize the electric field set up across the depletion region. This simplest form of an electrical devices is referred to as a diode.

However, most electrical devices have more than one P-N junction within them. Solar cells, for example, have multiple differently doped layers to assist in charge extraction. In Figure 7, with the built-in electric field there is energy required for an electron in the conduction band to move from the N-type region up to the P-type region. Similarly, there would be energy required for a hole to move from the P-type region to the N-type region in the valence band because of the built-in field at the interface. Engineers use these built-in fields to separate the electrons from the holes and prevent them from recombining. In this way using hole-selective and electron-selective layers can increase the efficiency of a solar cell.

2.2.b Current-Voltage Curves

The performance of a diode can be described through a graph of current density vs voltage (JV curve). Since a solar cell simplistically is a diode which reacts to light, a similar graph can describe the performance of a solar cell.

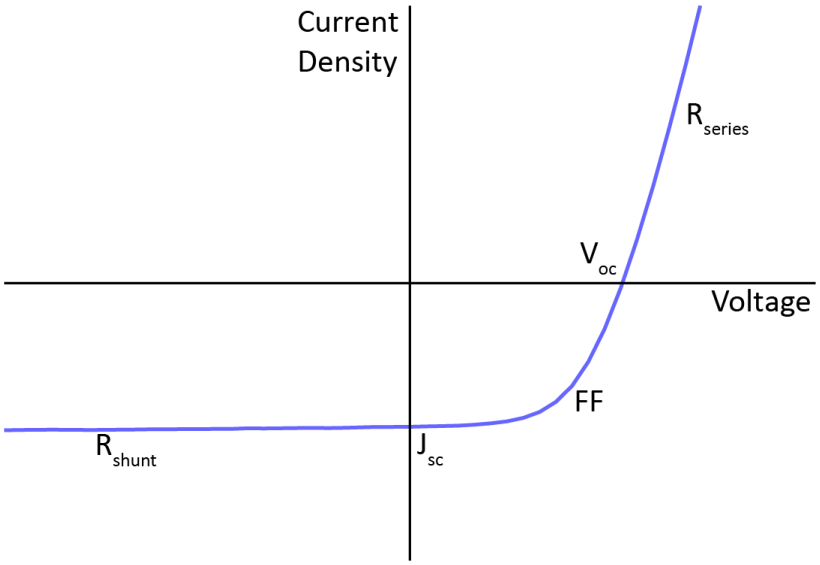

Figure 8. Example JV curve showing all of the different subcomponents including those that directly contribute to the power conversion efficiency (V_{OC}, J_{SC}, FF) and those that do not (R_S, R_{SH}).

JV curves break down the performance of a solar cell and as a result describe different aspects of how it is behaving. From a JV curve you get the power conversion efficiency (PCE) which is the efficiency with which the solar cell is converting sunlight to electrical power. Within that metric there is the short-circuit current (J_{SC}) which describes solar cell operation if both electrodes were shorted together. It describes the effectiveness of the device at extracting carrier and depends greatly on the absorber layer thickness and incident light. The open-circuit voltage (V_{OC}) by contrast describes the solar cell if both electrodes were open, without any load. It describes the internal voltage the solar cell can generate and depends on the absorber layer bandgap among other properties. Finally, the fill factor (FF) is a calculation of how close to angular the JV curve is. It is dependent on a large range of solar cell properties and can be hard to define what causes a high or low FF. Other parameters such as series resistance (R_S) and shunt resistance (R_{SH}) define the resistance to carriers being extracted and potential short circuit pathways through the device respectively. Looking to R_S and R_{SH} can help describe different effects seen in J_{SC} and V_{OC}.

2.3 Practical Considerations

For any solar cell material to be integrated into a device and then to become a product there are a number of interrelated practical considerations involving the fundamental physics within the device.

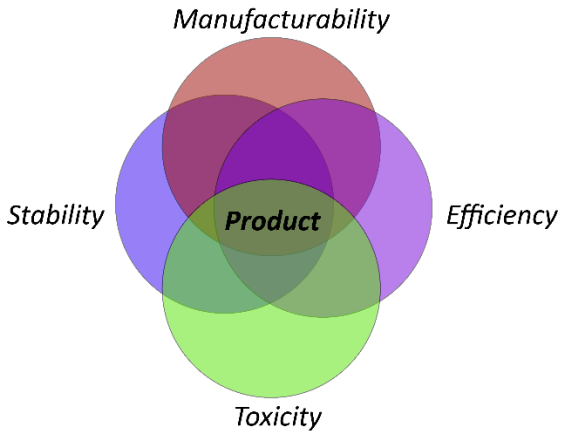

Figure 9. The four major components that contribute to the formation of a complete commercial product.

Perovskite solar cells initially gained notoriety through their extremely rapid rate of device efficiency improvements. They improved from 13% to >25% PCE in less than 10 years, virtually unheard of for any single junction solar cell[11]. However, even with this rapid increase in PCE, it was only recently that perovskites became competitive (based solely on efficiency) with other single junction solar cells on the market based on silicon.

One area of research to improve both device efficiency and stability is at the interfaces. Interfacial engineering can improve the charge carrier dynamics at the junctions with each transport layer[73], defect mitigation, and preventing ion migration[74,75]. Commonly, defects are the origin of instability within perovskite solar cells. Even with significant recent progress towards improving the stability of perovskite solar cells, it remains one of the largest barriers to commercialization. As a result, many researchers are focusing on passivation strategies to mitigate defects destabilizing devices[76]. Many have turned to

lower dimensional perovskites as passivation and encapsulation on top of the bulk perovskite absorber layer to improve stability[77].

Another technique is to develop perovskite specific encapsulation to mitigate stability issues[78] such as moisture ingression. These barrier films can play dual roles as the most efficient and stable perovskite solar cells contain lead levels that could raise toxicity concerns[79] at all life stages. As a result, many researchers have developed both chemical[80,81] and adhesive layers[82] for preventing lead leaching. Others focus on developing solvent systems less toxic than the ones currently used in the solution-processing field[83,84].

All these advances contribute towards the manufacturability of perovskite solar cells. However, in order for perovskite solar cells to be commercialized, all these advances need to be translated from the research scale to a much larger scale. Techniques for depositing solar cells on larger substrates are dividing into solution-processing methods such as slot-die coating and vapor-processing methods such as CVD and thermal evaporation[85,86].

Finally, the true metric of any technology is the cost structure. Improving the efficiency and stability while mitigating toxicity concerns over large areas all contribute to a favorable cost structure. One area that can quickly become cost prohibitive for many different solar technologies is the non-transparent electrode. Frequently for many materials, gold is favored since it is very non-reactive. However, gold electrodes are prohibitively expensive for commercialization and can be difficult to replace.

2.3.a Lower Cost Electrodes – PbS QDPVs as an Example

Prior to focusing on perovskite, we looked to another solar absorbing material that serves as a great example of how device architecture tuning can impact the overall cost structure.

With their tunable band properties and sharp absorption onset[87], PbS quantum dots (QDs) are one promising candidate for thin film photovoltaics (PVs). Many recent reports on the QD active layer build on developing ink-based deposition[88]. Replacing layer by layer spincoating by designing a single step QD layer deposition enables reductions in the cost to synthesize QD solutions and increases power conversion efficiencies (PCE) to 13.3%[89]. Other advances focus on engineering QD surface states[90,91] or ligand treatments[92].

These advances are centered around the state-of-the-art architecture of ITO/ZnO/PbS-TBAI/PbS-EDT/Au. Already, some researchers are scaling PbS QD deposition to larger areas[93,94]. However, significant issues remain when considering scaling these advances in PCE to larger area devices for manufacturing. One of the major disadvantages to the state-of-the-art QD solar cell is the reliance on a gold electrode.

Here, we focus on nickel oxide (NiOx) as an interlayer to facilitate lower cost electrodes. As a wide bandgap, p-type metal oxide, NiOx has historically been used as a HTL in a variety of devices including QDLEDs[95], organic PVs[96], and perovskite PVs[97]. Hyun *et. al.*[98] demonstrated both p-n and n-p QD device architectures using NiOx as a hole transport layer. Using only PbS QDs treated with EDT as the QD absorption layer, they reached 5.3% PCE when depositing NiOx on top of the QD layer. Additionally, a recent report uses a thin spin-coated layer of NiOx to improve PbS QDPV device stability when exposed to heat or oxygen plasma[99].

By adding a NiOx interlayer into the state-of-the-art QD solar cell architecture we allow both aluminum and copper electrodes, thus permitting less expensive device architectures and added flexibility in design. Additionally, we investigate the effect of

lower cost electrodes on the shelf-life stability and find that a thin buffer layer between the NiOx and electrode improves stability.

Lower cost electrodes such as aluminum, chromium, or copper are prone to oxidation and other chemical reactions that can limit use in devices. Therefore, to enable these new electrode materials an interlayer must be introduced that enables more reactive materials without significantly adding to material prices. Sputtering (compared to thermal evaporation for the electrode materials) is not expected to significantly add to the total manufacturing cost since it uses higher deposition pressures. Additionally, in the long-term lower cost electrode materials can also be sputtered, decreasing manufacturing costs even more.

In the beginning NiOx enables lower cost electrodes, however to enable this QD architecture to move closer to manufacturing, it needs to be stable over the long term. After about a month of shelf-life storage the solar cells start to degrade[100]. Table 1 shows the variable time scale with which devices start to display a characteristic S-curve shape indicating an energy barrier within the device stack.

Device Run	Time	NiOx Thickness	PCE Decrease
A	56days	10nm	72%
		20nm	51%
B	62days	10nm	<1%
		20nm	76%
C	70days	10nm	17%
		20nm	11%
D	34days	5nm	<1%
		10nm	16%
		15nm	60%

Table 1. Timescales required for PbS QDPVs with aluminum electrodes to develop an electronic barrier and lose power conversion efficiency.

Only when the electrode material changes to aluminum (or copper) does the PCE of the devices starts to degrade over time. Although bare aluminum will oxidize in a couple of minutes in air, device degradation occurs on average in one to two months. Additionally, the formation of an energy barrier happens at multiple NiOx film thicknesses without a correlation in the time it takes the device PCE to decay. This seems to indicate that it is the interface between the NiOx and aluminum electrode that is degrading with time. Furthermore, NiOx thickness does not determine length of time required for degradation. If NiOx were acting as a diffusion barrier for chemicals from within the device stack, thicker NiOx layers would improve device stability.

If chemical diffusion originating within the QD layers is not the most likely cause of degradation, another possibility is that the aluminum and NiOx is reacting. Aluminum oxide (Al_2O_3) has a lower free energy of formation than NiOx therefore any loosely bound

oxygen in the NiOx would preferentially oxidize the underside of the electrode. Although J. Li *et. al.*[101] recently reported an increase in PCE with a passivating Al_2O_3 layer in QDPVs, the layer thicknesses used were around 0.5nm with significant ingress into the PbS-EDT layer. An oxidation reaction at the aluminum/NiOx border would not reach the PbS layers and be significantly thicker, thus preventing efficient charge extraction. In fact, oxidation at the electrode/NiOx interface is an effect commonly seen in resistive switching memory devices[102,103] and oxidation at the electrode/polymer interface is a common reason for degradation in OPVs[104,105].

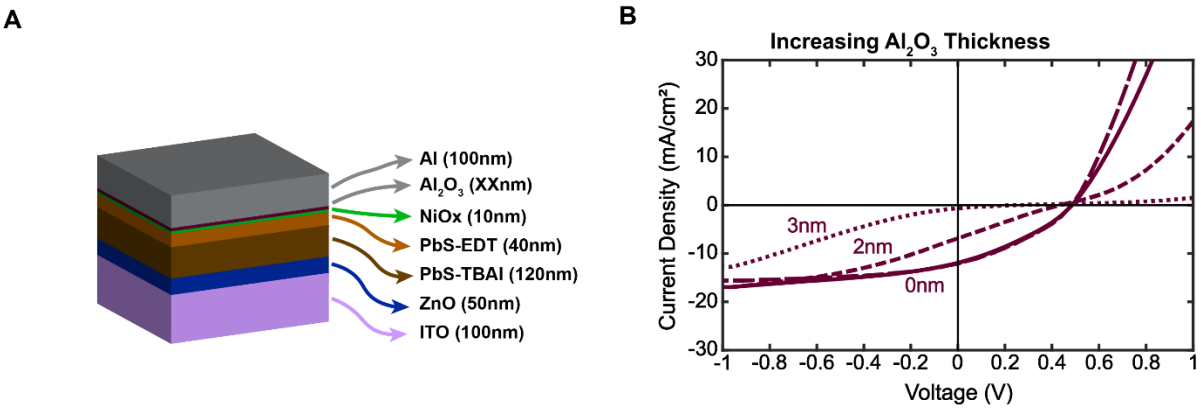

Figure 10. Decrease in device efficiency due to the formation of an Al_2O_3 barrier between NiOx/Al. (A) Growth of an electronic barrier in JV curves of a single device over 2 months. (B) Tracking shelf-life stability of different device architectures. (C) Sputtering and Al_2O_3 layer into the device stack. Increase in Al_2O_3 thickness corresponds to the growth of an electrical barrier in the JV curves.

Oxidation of the aluminum/NiOx interface would produce up to 4nm of Al_2O_3. By purposefully adding a 0-3nm thick Al_2O_3 at the NiOx/Al interface (Figure 10.B), we can replicate the degradation profile. One way to increase the stability of these more reactive electrodes is to insert an oxygen resistant layer between NiOx and the electrode.

Two buffer layers that could assist in preventing oxidation at the NiOx/electrode interface are chromium and ITO. In OPVs, the addition of a chromium oxide layer was found to prevent oxidation at the organic/Al interface[105]. In perovskite solar cells, ITO is oftentimes

used to prevent underlying materials from reacting with the electrodes[106]. These materials act best as ultra-thin buffer layers due to higher material costs than aluminum and since they lack the potential to be used as HTLs.

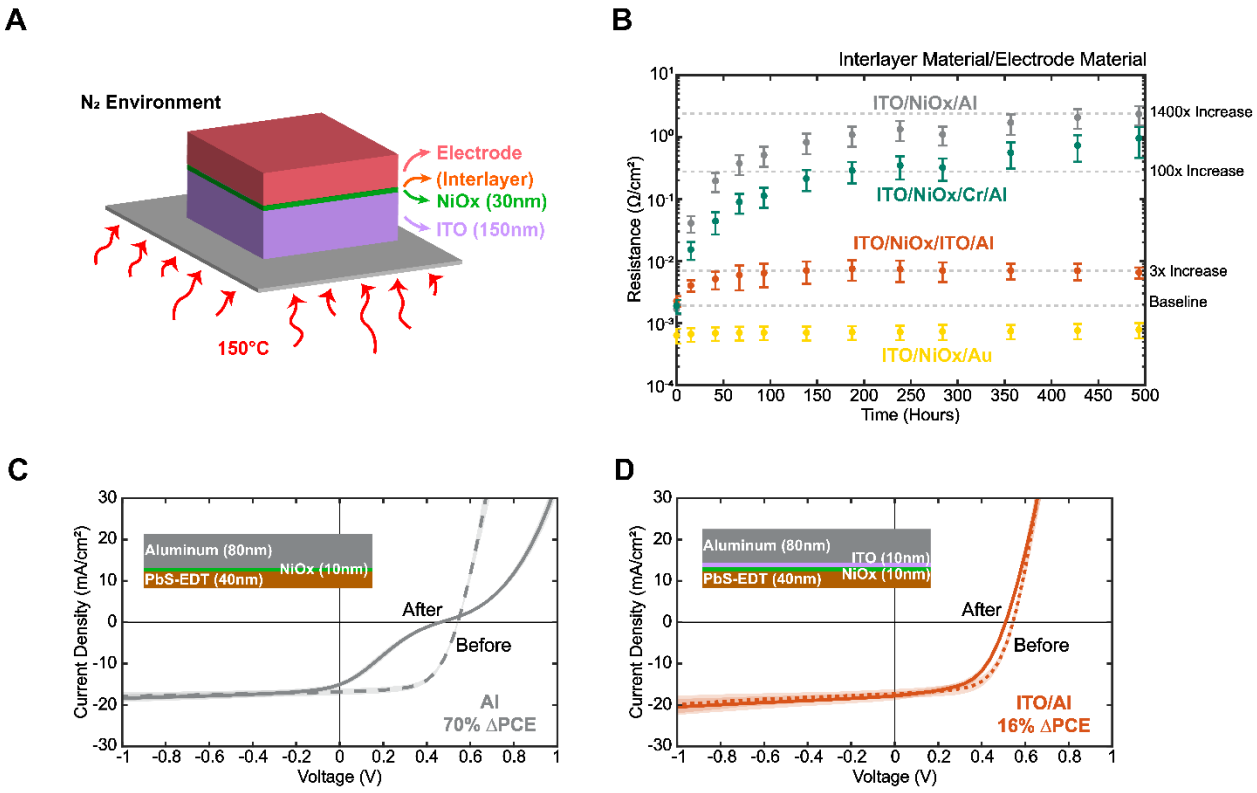

Figure 11. Influence of a buffer layer between the NiOx and electrode. (A) Experimental setup for accelerated lifetime testing of NiOx films. 30nm thickness is used to ensure film completeness. (B) Resistances of film stacks using testing setup shown in A. Different buffer layers and electrode materials are shown. (C) QD device stability over six weeks without a buffer layer. (D) QD device stability over six weeks with an ITO buffer layer.

To investigate ITO or Cr as a potential buffer layer between NiOx and aluminum electrode we first used accelerated testing on films alone. NiOx films were deposited on top of ITO electrodes with either ITO or Cr as a buffer layer or no buffer layer at all. Aluminum or gold electrodes deposited on top allowed for resistance measurements over time and after accelerated lifetime testing. To increase the speed at which these films degraded, they were annealed at 150ºC in inert conditions. Since it is likely interstitial oxygen that is

reacting with the underside of the aluminum electrodes, the additional heat helps with oxygen diffusion and increases the rate of aluminum oxidation.

At regular intervals these films were measured for through-film resistance in an inert atmosphere. Films with no buffer layers and gold electrodes did not significantly change in performance, indicating that the NiOx itself is quite stable under these accelerated lifetime testing conditions. Under heat treatments the films with aluminum electrodes and no buffer layer quickly increase in resistance. Films with either an ITO or Cr buffer layer also show some initial increase in resistance that stabilizes over time.

Based on the accelerated testing of films, an ITO buffer layer was integrated into devices with aluminum electrodes and compared to devices without buffer layers. Figure 11C shows device performance after a month in the dark under a nitrogen environment. Each type of device is the state-of-the-art architecture with a 10nm NiOx interlayer, optional 10nm ITO buffer layer, and 80nm aluminum electrode with the inset highlighting the changes. For devices with a NiOx interlayer and aluminum electrode 70% of the PCE was lost over the course of a month in a dark, inert atmosphere, originating from the creation of a barrier in the device. In contrast, with an ITO buffer layer the device only loses 16% in device efficiency thus slowing down the degradation and allowing the use of an aluminum electrode.

In summation, NiOx interlayers paired with an ITO or Cr buffer layer allow for the use of a variety of lower cost electrodes such as aluminum. Substituting NiOx interlayers with buffer layers allows for flexibility in device architectures with comparable PCEs to the state-of-the-art. Additionally, the aluminum-based architecture facilitates the move towards QDPV manufacturing through an over 130,000 reduction in material costs. While this work focused on enabling low-cost electrodes for QDPVs, it also shows the potential

for lowering device architecture costs for other PV materials such as organics or perovskites.

2.4 Further Reading

These textbooks were instrumental in the preparation of this chapter and provide further information on the concepts presented.

Physics of Photonic Devices

Chuang, S. L. *Physics of Photonic Devices.* (John Wiley & Sons, Inc, 2009).

Semiconductor Device Fundamentals

Pierret, R. F. *Semiconductor Device Fundamentals.* (Addison-Wesley Publishing Company, Inc, 1996).

3. Influence of Vapor Co-Deposition on Methylammonium Iodide Degradation

3.1 Motivation

An exciting but challenging aspect of perovskites is the wide variety of compositions that can be successfully used in optoelectronic films[107]. Although many researchers are looking to replace MAI due to stability issues[108], $MAPbI_3$ perovskites are a relatively simple organic-inorganic framework compared to other perovskite formulations and are still widely studied. Therefore, we will continue to use $MAPbI_3$ and compare our findings to current literature understanding.

Understanding the role that MAI has in $MAPbI_3$ inherently needs to include investigations using solution-processing due to the high volume of literature. However, the two general deposition techniques have very different origins for introducing defects. In solution-processing, the solvents and surfactants dictate film formation and are often the origin of defects. However, vapor-processing does not use solvents, rather it can introduce defects through the heat used during deposition.

The MAI amount in $MAPbI_3$ perovskite films necessary to produce high performing solar cells remains an active area of research. Some researchers advocate for using a MAI interlayer, which prevents unwanted reactions with transport layers[109] and its dissociative products can alter energy levels to better align with transport layers[110,111]. However, MAI provides an inroad for which moisture can penetrate the entire $MAPbI_3$ film[112]. While moisture can aid in conversion to perovskite and some moisture penetration is reversible, after a long time or with enough water perovskite films permanently degrade[113,114]. Thus,

there is a fine balance between favorable energy level manipulation and inducing stability problems.

Additionally, the presence of defects within the bulk $MAPbI_3$ film partially determines film properties[115], including stability. Although stability for vacuum-deposited solar cells has only started to be investigated, promising results demonstrate how CVD and thermally evaporated perovskites are quite different from solution-processed perovskite[116,117]. Therefore, as we proceed, we will reference solution-processed results but acknowledge the potential differences due to processing technique.

Under vacuum, lead-based metal halides have sublimation temperatures ranging from around 300°C to well over 500°C. In contrast, organic components such as MAI and formamidinium iodide (FAI) have sublimation temperatures under 200°C. The new VTD system needs to balance co-deposition with one precursor material (MAI) subliming around 170°C and another (PbI_2) subliming around 370°C. These differences in sublimation temperatures are significant, since organic precursors degrade under PbI_2 temperatures[118,119].

One unique and currently understudied aspect of vapor-based depositions is how depositional stresses integrate into the surface and bulk properties of films. There are debates surround the degradation of MAI powders exposed to high temperatures. The two dominant theories are that MAI decomposes into either iodomethane (CH_3I) and ammonia (NH_3) or hydroiodic acid (HI) and methylamine (CH_3NH_2). Although the decomposition into iodomethane and ammonia has been repeatedly calculated to be the thermodynamically favorable pathway, many experiments clearly demonstrate the presence of hydroiodic acid and methylamine products[118,120]. These discrepancies could be due to experimental factors that influence the degradation pathway, including

temperature, surrounding atmosphere, pressure, catalyst presence, and source boat configurations. The results from these experiments assist in understanding potential degradation that occurs during sublimation during thermal evaporation.

In contrast, VTD contains two decoupled heating processes as shown in Figure 12.B: sublimation temperature and deposition zone temperature.

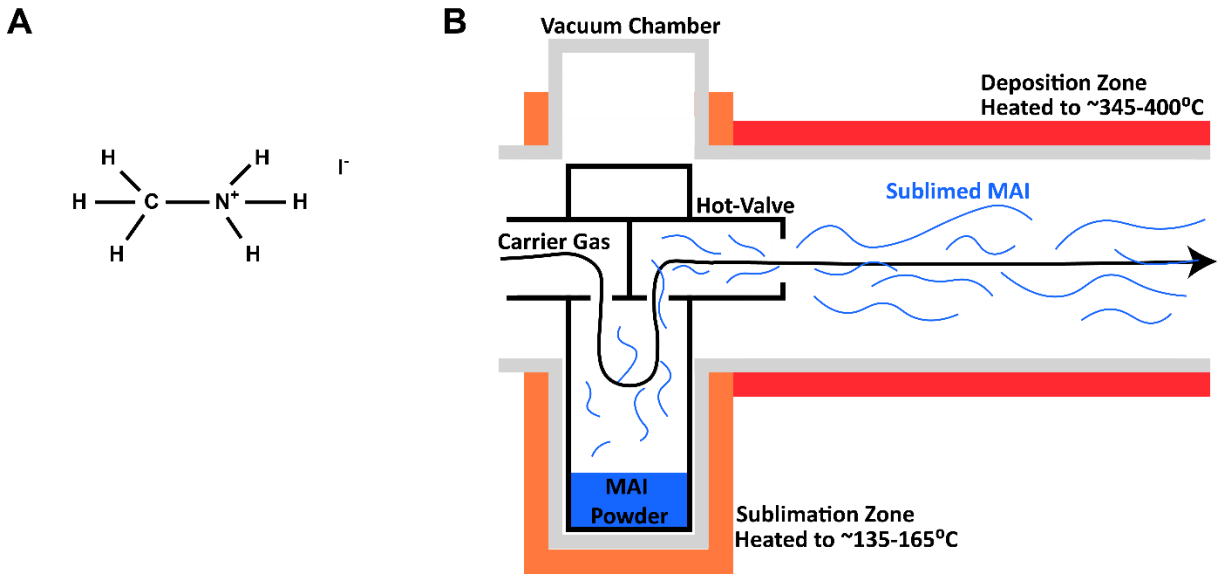

Figure 12. Methylammonium iodide structure and deposition process. A) Molecular structure of methylammonium iodide. B) Diagram of the separate temperatures that methylammonium iodide experiences during VTD.

Sublimation zone temperature provides the thermal stresses the MAI powder experiences during sublimation. Building up a partial pressure of sublimed material is a balance between using a high enough temperature to get a high rate of sublimation but not so high that MAI degrades due to thermal stress. In contrast, the deposition zone temperature is set by the temperature needed to keep PbI_2 sublimed, and MAI only needs to survive a brief period of transit in this zone. Thoroughly understanding the degradation that can come from both zones would assist in identifying and healing defects to create high quality $MAPbI_3$ films.

Here, we investigate the influence of sublimation temperature and deposition temperature to determine the process parameters that contribute to the degradation of MAI and better understand the integration of MAI defects into the final perovskite film. By using Fourier Transform- Infrared – Attenuated Total Reflection (FTIR-ATR), we catalogue how different temperatures change the bonds within MAI powders and films. Then, we use X-Ray Diffraction (XRD) to determine how different deposition techniques influence the structure of perovskite films. By starting with our system as an example and then expanding into a more generalized system, we can make recommendations regarding the use of co-deposition and the role that deposition temperature has in MAI degradation.

3.2 Sublimation Temperature Influence

The first potential degradation region during the MAI deposition process is due to the sublimation temperature. To create a baseline, we first investigate the precursor powders before they enter the vacuum system.

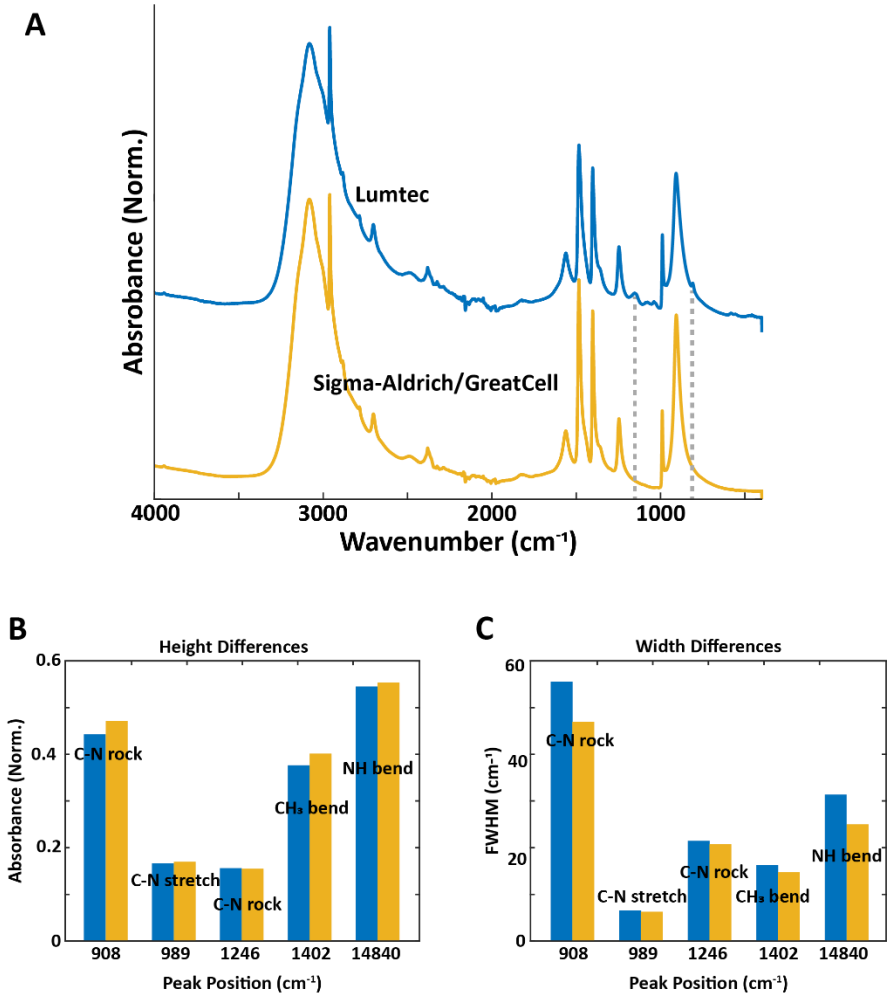

Figure 13. FTIR-ATR spectra of different MAI precursor powders. Note: Sigma-Aldrich and GreatCell use the same manufacturer for their powders. A) Normalized FTIR-ATR spectra of both powders. B) Difference in the relative heights of peaks in the fingerprint region. C) Differences in the full-width half-max of the peaks from A).

Compared to Sigma Aldrich/GreatCell MAI powders, Lumtec precursor powders contain two minor peaks at 809cm^{-1} and 1154cm^{-1} with expansions of the full-width half-max (FWHM) of the peaks at 908cm^{-1} and 14840cm^{-1}. The additional peaks suggest organic contaminants consistent with the recent findings that lower purity MAI has better adhesion properties and film performance[43,121] which is consistent with the high level of use with Lumtec MAI precursor powders in the QCM-controlled thermal evaporation discussion[29,122]. The peak broadening suggests additional hydrogen bonding or other differences in the bonding structure of the Lumtec powder compared to the Sigma

Aldrich/GreatCell powder. With this baseline, next we can look into how the Lumtec MAI powder specifically evolves as a function of sublimation temperature.

To investigate the influence of sublimation temperature, MAI powder was loaded into the VTD system and sublimed at a range of temperatures. We used sublimation temperatures at the lowest and highest consistently-depositing temperatures and removed the leftover powder from the material arms. Through this experiment we can see how precursor powder ages with respect to its sublimation temperature without exposing it to an additional deposition temperature and film growth process.

Figure 14.A shows the evolution of MAI powder as it experiences a variety of sublimation temperatures. We focus on the fingerprint region, as it determines the molecule present, and use previous literature reports to label the different bonds[123,124].

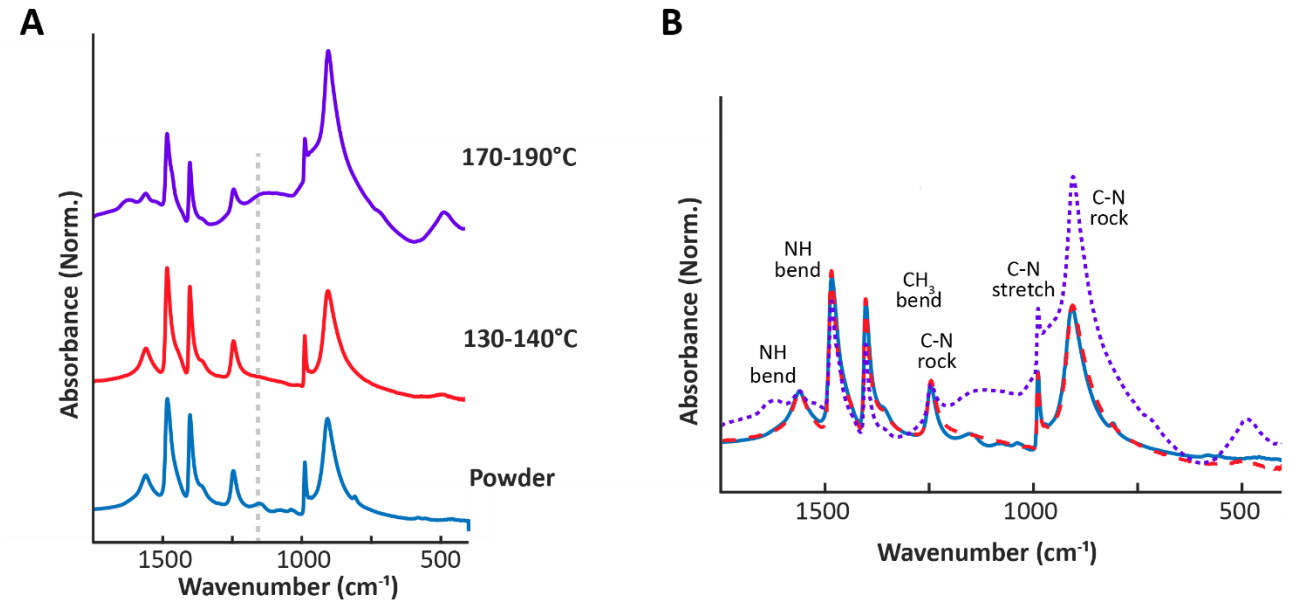

Figure 14. FTIR-ATR spectra of Lumtec MAI powders after experiencing a range of sublimation temperatures. A) Normalized fingerprint region for the raw precursor powder, powder after experiencing 130-140°C sublimation temperatures, and powder after experiencing 170-190°C sublimation temperatures. The grey, dotted line highlights the presence of an organic contaminant in the precursor powder. B) Overlapping FTIR spectra to demonstrate the changes to peak heights and full-width half-max. Each peak is labeled with its corresponding MAI bond.

The bottom blue line corresponds to a fresh precursor powder before any sublimation treatments. The next two lines represent powders from sublimation boats after experiencing two different zones of sublimation temperatures. The red, lower 130-140°C curve is relatively similar to the baseline powder curve. The only dramatic appearance/disappearance of a peak is at 1153cm^{-1} which appears in the baseline powder but not in the 130-140°C sublimation curve. Additionally, the relative intensities, locations, and FWHMs of the two curves are identical, demonstrating <1% variation between the two powders, which is the instrumental limit for FTIR-ATR.

Meanwhile, the 170-190°C and precursor powder show significant deviations from each other. For the 170-190°C powder, the peaks at C-N stretch and C-N rock combine indicating either peak broadening or formation of a new structure. A similar convergence

of these two peaks was found in a sample that contained a $CH_3NH_3I{\cdot}xCH_3N_2$ complex of MAI and methylamine gas, from a paper where amine complex precursors and pressure were used to create perovskite films[124]. This would be consistent with the growth of a potentially additional peak around 1120cm^{-1}. However not all the peaks documented in the pressure-based deposition technique appear here, potentially due to the low amount of the highly volatile methylamine gas. Other degradation products could also be forming, such as hydroiodic acid, ammonia, or iodomethane which would show broadening of the peaks due to new hydrogen bonds within the molecule or appearance of new peaks with organic byproducts not attached to a full MAI molecule. The appearance of these peaks at generally higher wavenumbers than intact MAI indicates that the overall mass of that molecule (and therefore peak appearance) has been lowered, further confirming some degradation process.

Overall, combining current literature with the results found here indicate that if we chose both the best MAI precursor powder and the lowest sublimation temperature compatible with our system, we should see a minimal amount of degradation for our precursor powder. However, as the next section shows, this only one process by which our MAI powder may degrade during deposition.

3.3 Deposition Zone Temperature Influence

One benefit to VTD is the ability to use an optimal MAI sublimation temperature to minimize degradation while not greatly influencing the deposition rate. However, the deposition zone temperature must be set by the highest sublimation temperature for the precursors within the system. Therefore, MAI must be exposed to a period of higher chamber and carrier gas temperatures. This aspect of MAI degradation is rarely studied since most vapor-processes focus on using thermal evaporation where this type of degradation would not occur.

Figure 15 shows how a powder evolves if it is sublimed at the lower temperature but then experiences a brief period in a deposition zone at a range of temperatures.

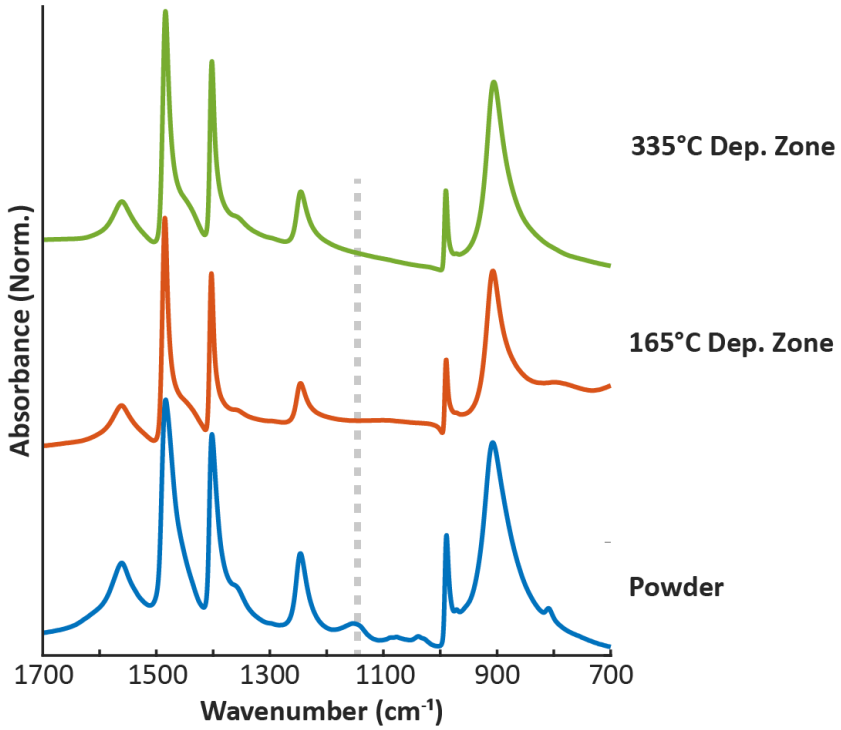

Figure 15. FTIR-ATR spectra of MAI powder sublimed at 130-140°C and experiencing a range of deposition zone temperatures.

Here, we see no significant peak appearances/disappearances in any of the films or powders other than the aforementioned 1153cm^{-1} peak. In these FTIR spectra we do not see consistent or significant changes in either peak position, relative intensity, or FWHM indicating minimal changes to MAI bonding during a heated deposition process (additional peaks presented in SI). This may indicate that the degradation experienced by MAI is more significant in the sublimation zone than the deposition zone.

3.4 Expanding MAI Degradation Results to General VTD Systems

Previously, we decoupled sublimation and deposition temperature to inspect the MAI degradation caused in our VTD system. However, to generalize these findings, we expand temperature ranges to correspond with a wider set of metal halide sublimation temperatures. In the next series of experiments, we use a tube furnace with two different heated zones to learn about the joint degradation effects of sublimation temperature and deposition temperature.

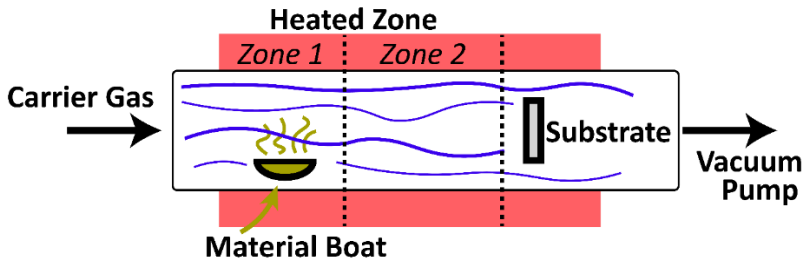

Figure 16. Diagram of a Three Zone Tube Furnace which is used for the VTD chamber of simplified MAI degradation experiments. Only Zone 1 and Zone 2 are actively heated.

The MAI sublimes at a lower temperature of 270°C in Zone 1. Then the MAI is transported with a heated carrier gas through Zone 2 to the substrate. We start by depositing MAI through a range of Zone 2 temperatures, from a lower co-deposition temperature to a higher one, corresponding to a range of metal halide sublimation temperatures.

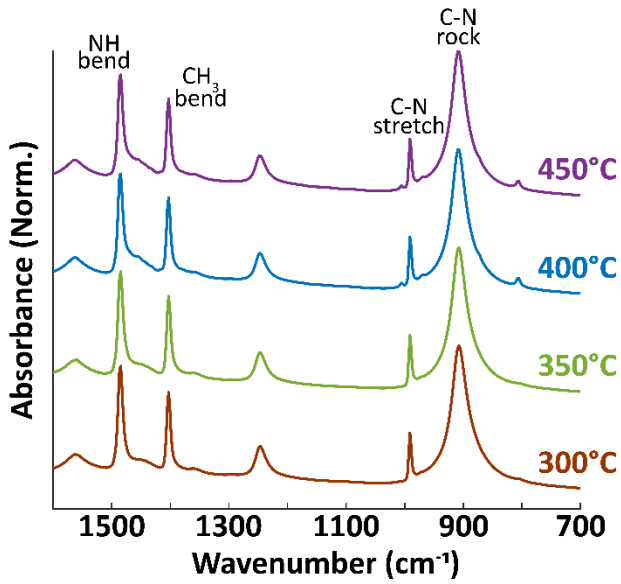

Figure 17. FTIR-ATR spectra of MAI powders after experiencing both an elevated sublimation temperature and a range of deposition temperatures.

FTIR-ATR results show a change in bonding structure at Zone 2 temperatures between 350-400°C. Films deposited from MAI sent through a region 350°C or cooler have consistent peak locations and intensities. New peaks and changing peak intensities appear consistently at deposition temperatures above 400°C. The changes in FTIR results are identical at both 400°C and 450°C deposition temperatures. Furthermore, these changes do not vary between measurements across the film. The difference in peaks only appear in the fingerprint region. See SI for full FTIR-ATR spectra.

Shown in Figure 17, there are four modifications to the FTIR spectrum between films deposited through a 350°C and a 400°C Zone 2. There is an increase in peak intensity around 1450cm^{-1} and the appearance of new peaks at 1005, 970, and 805 cm^{-1}. The peak in both films occurring at 991 cm^{-1} corresponds to a C-N stretch[112]. One potential explanation for the appearance of two smaller peaks around the large peak in the higher temperature films is the addition of more C-N bonds. With more bonds there would be a symmetric and asymmetric stretch, which would offset the peak appearance relative to a

molecule with a singular C-N bond. The increase in peak intensity around 1450cm^{-1} could correspond to increased symmetric NH or asymmetric CH_3 bends[112,123]. This potential explanation corresponds well with literature on mass spectrometry results, which indicate the appearance of more complicated carbon and nitrogen compounds at higher temperatures[125].

While FTIR probes the bulk of the film, XPS analyzes the surface of the perovskite film. Once again there is a shift in chemistry between 350-400°C. Figure 18 shows the total carbon, nitrogen, and iodine content within the film. Likely there is more carbon than nitrogen in the film due to adventitious carbon on the surface of the film. The relative ratio between carbon and nitrogen stays the same throughout all the samples. However, above 350°C the percentage of carbon and nitrogen decreases while that of iodine increases. At higher temperatures carbon and nitrogen are expected to form gaseous degradation products[118,125] and therefore may not re-deposit on the surface of the film after passing through Zone 2. This could explain the decrease in the amount of carbon and nitrogen on the film. Another potential explanation is that exposure to the hot zone may increase the mobility of iodine. Therefore at least the surface of the perovskite film is becoming iodine rich at temperatures above 350°C.

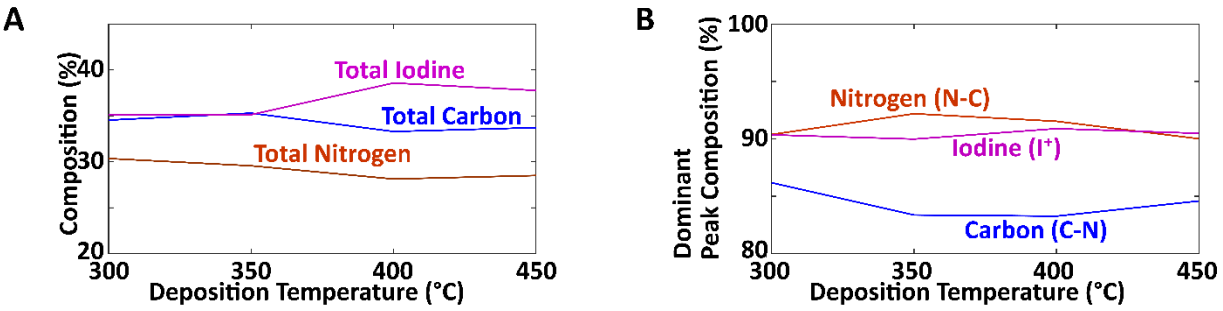

Figure 18. Analyzed XPS spectra of the dominant species comprising MAI. A) Tracks the compositional changes by deposition zone temperature. B) Tracks the dominant peak contribution by deposition temperature.

Looking deeper into the bonding chemistries within these peaks shows if the elements are forming different compounds while remaining in the film. As opposed to the changes in the total perovskite composition, Figure 18 shows that the distribution of dominant bonds associated with each element stays the same (peak assignment in SI). For example, the appearance of more N=C bonds than N-C bonds at higher temperatures would correspond to a drop in the nitrogen curve. Here, the bonding chemistries stay relatively the same regardless of Zone 2 temperature indicating that the loss of overall carbon and nitrogen is not also forming new compounds at the surface of the film.

3.5 Integration into Perovskite Films

Since MAI films alone cannot contribute to the active layer of a solar cell, we next integrate the MAI precursor into a $MAPbI_3$ perovskite film. By examining the influence MAI degradation has on the bonds and crystallinity of co-deposited and sequentially-deposited perovskite films, we can both determine appropriate next steps for optimization and make recommendations for focusing on either co-deposition or sequential deposition.

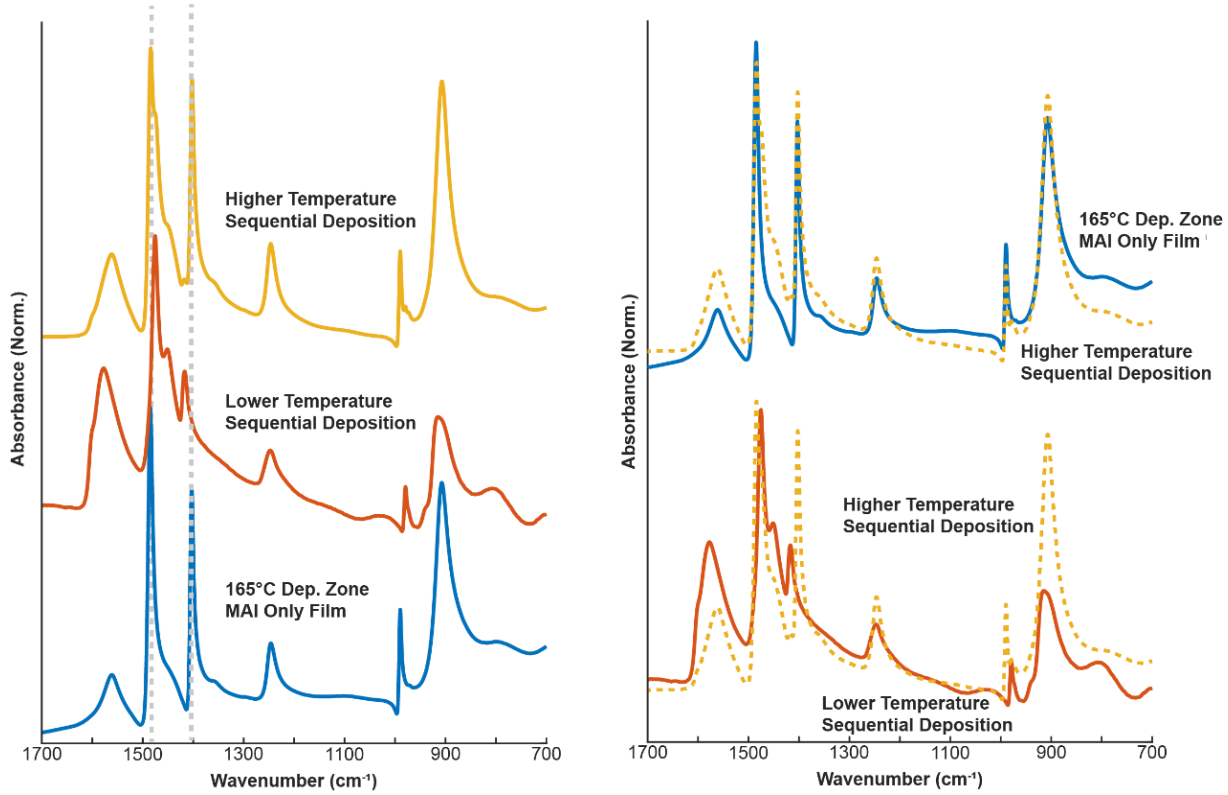

Figure 19. FTIR-ATR spectra of sequentially deposited $MAPbI_3$ films. The higher temperature sequential deposition corresponds to the temperatures that MAI would experience during co-deposition while the lower temperature corresponds to a deposition temperature tailored for preserving MAI.

As an inorganic precursor, we do not expect to see any contribution from PbI_2 alone but will see the organic signature of MAI shift with the new bonds. As shown in Figure 19, there is no longer any contributions from methylamine gas at any temperature, as the peaks at 969cm^{-1}, 1024cm^{-1}, and 1179cm^{-1} do not appear[124]. The higher wavenumber methylamine peaks are harder to distinguish from other perovskite bonds in these samples. However, there are significant differences in the relative peak intensities and FWHMs of different peaks within each sample. In general, the peaks associated with the lower temperature sequential deposition are broader, indicating an increase in the interactions of that bond with other species in the crystal lattice. In contrast, the peaks within the higher temperature sequential deposition spectrum show minimal changes compared to the MAI-only film. This could indicate that with a higher deposition

temperature the MAI precursor experiences difficulties in integrating into the perovskite crystal lattice.

To further decouple the potential factors determining perovskite lattice growth, we next use XRD to determine crystalline properties of co-deposited and sequentially-deposited films. In this $MAPbI_3$ perovskite film series, the top XRD spectrum (Figure 20) is the standard co-deposition process. The next two films are both sequentially deposited, with PbI_2 as the first precursor deposited and then MAI to convert the PbI_2 film into $MAPbI_3$ perovskite. In the middle film the MAI-only layer is deposited at the same deposition temperature as the co-deposited film. The final MAI-only layer is deposited at a significantly lower temperature, corresponding to the ideal deposition temperature for MAI. The films are fit according to previous literature results[112,126].

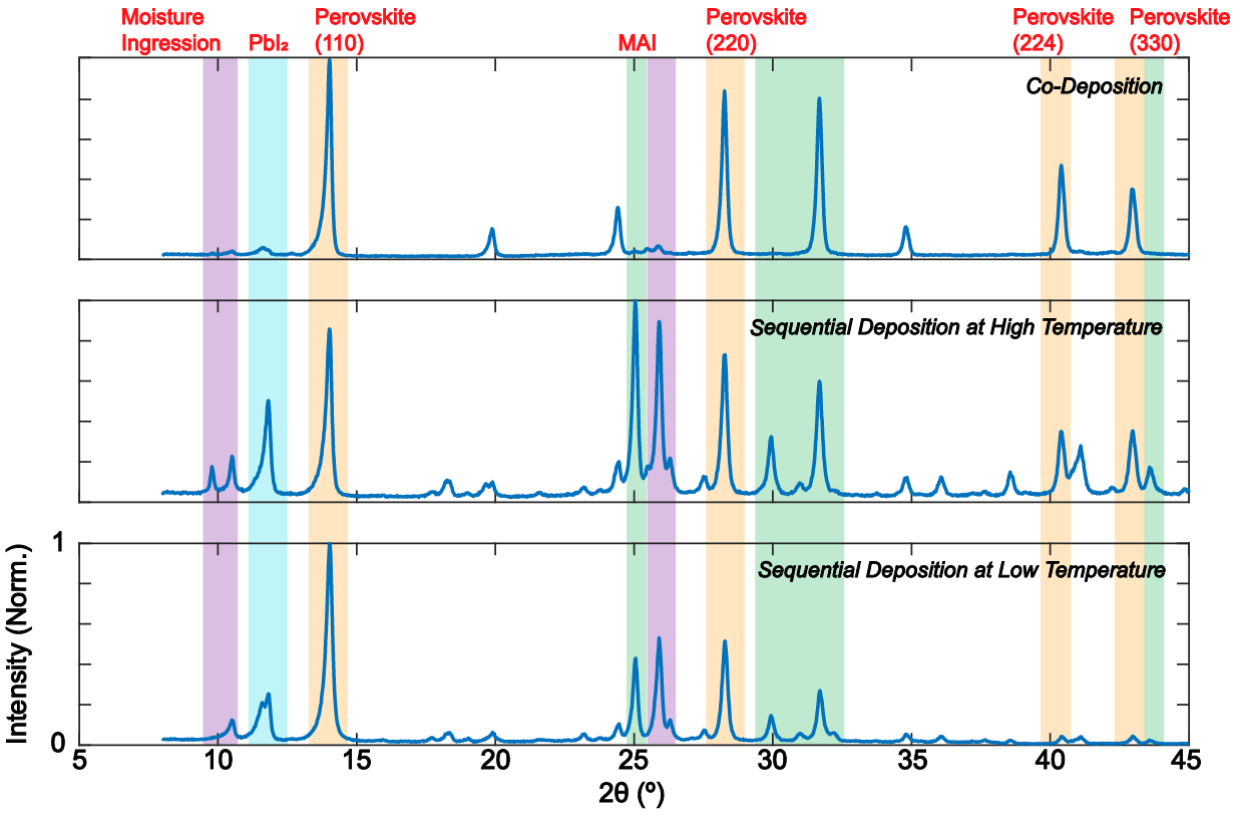

Figure 20. XRD spectra of co-deposited and sequentially deposited $MAPbI_3$ films. High temperature sequential deposition corresponds to identical conditions as the co-deposited films.

A preliminary survey of the data reveals that no two graphs are the same, with even the most dominant peak changing depending on deposition process. For both the co-deposited film and the sequentially deposited film at low temperature, the $MAPbI_3$ 110 phase is dominant. However, for the sequential deposition at high temperature the dominant peak corresponds to MAI.

The same four perovskite phases show up in all three XRD graphs, However, the sequential deposition graphs show more unreacted precursor peaks than the co-deposition graph. Both show signatures of unreacted MAI and PbI_2 while the co-deposition graph only shows an excess MAI peak. Since the interaction volume of the XRD beam encloses the entire film, it is possible that there are two unreacted precursor layers. Sequential films are deposited by first laying down a film of PbI_2 and then converting with MAI so if the

film does not fully convert there would be pure PbI_2 in the back while the front is unreacted MAI. Unreacted MAI on the surface of the sample also explains why the sequentially deposited films exhibit peaks associated with moisture ingression into the film[112]. This suggests that post-deposition treatments to improve conversion and resulting crystallization may be necessary for thick, sequentially deposited films.

3.6 Influence of Post-Deposition Film Treatments

Commonly, highly efficient and stable perovskite solar cells make use of post-deposition treatments to modify the interface, reduce mobile species, and/or de-sensitize the perovskite surface to the surroundings[127,128]. These treatments can vary widely from annealing the film[129,130] to depositing a 2D material on the top interface[131]. In vacuum-deposited perovskites, annealing or isopropanol (IPA) treatments post-deposition are used to facilitate a uniform reaction and/or remove excess degraded precursor material such as MAI. Therefore, understanding how post-deposition treatments that do not intend to leave behind a surface-modifying molecule are an important place to start.

Using the data from the previous section as the baseline, we take the higher temperature sequentially deposited films and do either annealing or IPA post-deposition treatments and track the MAI bonding changes using FTIR (Figure 21).

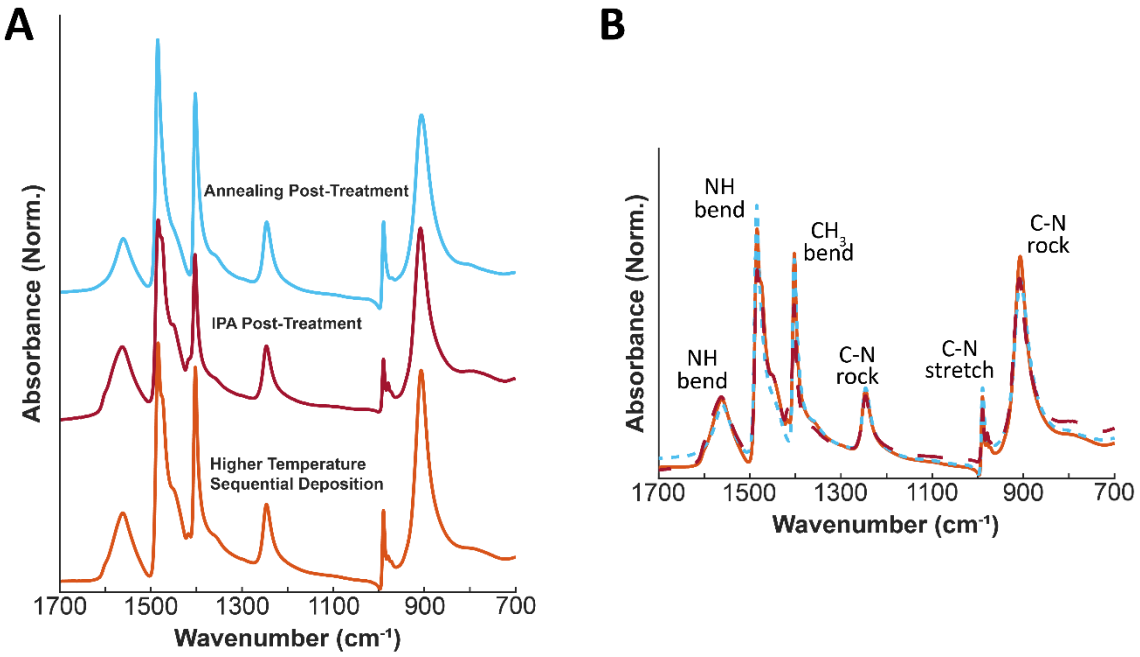

Figure 21. FTIR-ATR spectra of high temperature sequentially deposited films and their different post-treatments. A) Fingerprint region spectra. B) Overlapping spectra showing the differences in peak heights and FWHM. Important peak information is labeled.

Once again there appears to be a peak around 1120cm^{-1}, which could correspond to methylamine gas. This could be consistent with the disappearance of that peak for the annealing post-deposition treatment, as methylamine gas is volatile. Beyond that peak, post-deposition treatment does not show significant changes to the baseline, higher temperature sequential deposition film. Once again however, they do still vary from the lower temperature sequentially deposited film. Therefore, it seems the initial deposition type has more of an influence over the MAI bonding structure and species than the post-deposition treatment. Focusing more specifically on IPA, since it is intended to directly influence the presence of excess MAI and MAI degraded products, we move to looking at the role temperature has in film crystallinity.

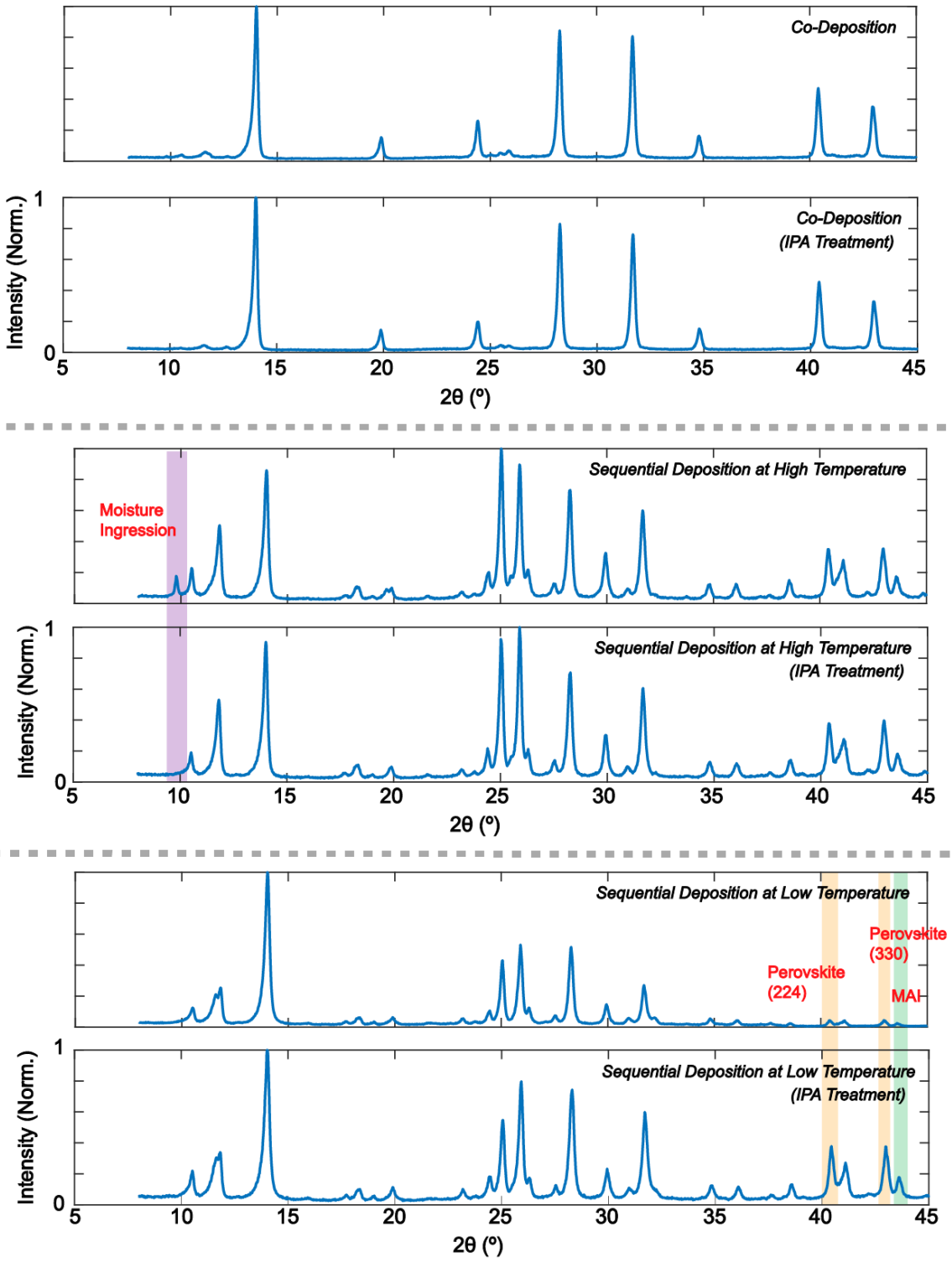

Figure 22. XRD spectra of co-deposited and sequentially deposited films before and after IPA post-deposition treatments. Baseline spectra are also shown in Figure 21.

For the co-deposited films, the IPA treatment does not have much of an influence on the crystalline structure. However, for both the sequentially deposited films there are the disappearance/reappearance of peaks associated with IPA treatments. For the films sequentially deposited at a high temperature the peak most associated with moisture ingression disappears after IPA treatment, since the dihydrate is closely tied to excess MAI and can be rinsed away using IPA[132,133]. For the sequentially deposited film at lower temperatures the IPA rinse cycle increases the contributions of perovskite at the 2θ values. Additionally, for both sequential films the ratios of peak intensities between 25-33° changes as a result of IPA rinsing. Since both precursor and perovskite peak ratios are shifting after IPA treatments, it is unclear whether the IPA rinses help specifically with the crystallization of the perovskite films.

3.7 Conclusion

It is currently unclear how these changes in the film will impact the solar cell performance. However, through cataloging the changes in VTD perovskite films we have a starting place for optimizing solar cells. We show that in our system the sublimation temperature has more of an influence on degradation products than the deposition temperature. We went on to expand our results to a more general tube furnace system where we show that the transition to degradation during deposition occurs between 350-400°C. Finally, we translated this bonding information into crystallinity information through the use of XRD. We show that even for the same temperatures sequential deposition does not form the same perovskite as co-deposition. The co-deposited perovskite shows the highest contributions from perovskite phases while previous findings from FTIR-ATR demonstrates that using a lower sublimation temperature minimizes degradation, altogether showcasing $MAPbI_3$'s ability to be co-deposited via VTD.

3.8 Supplementary Information

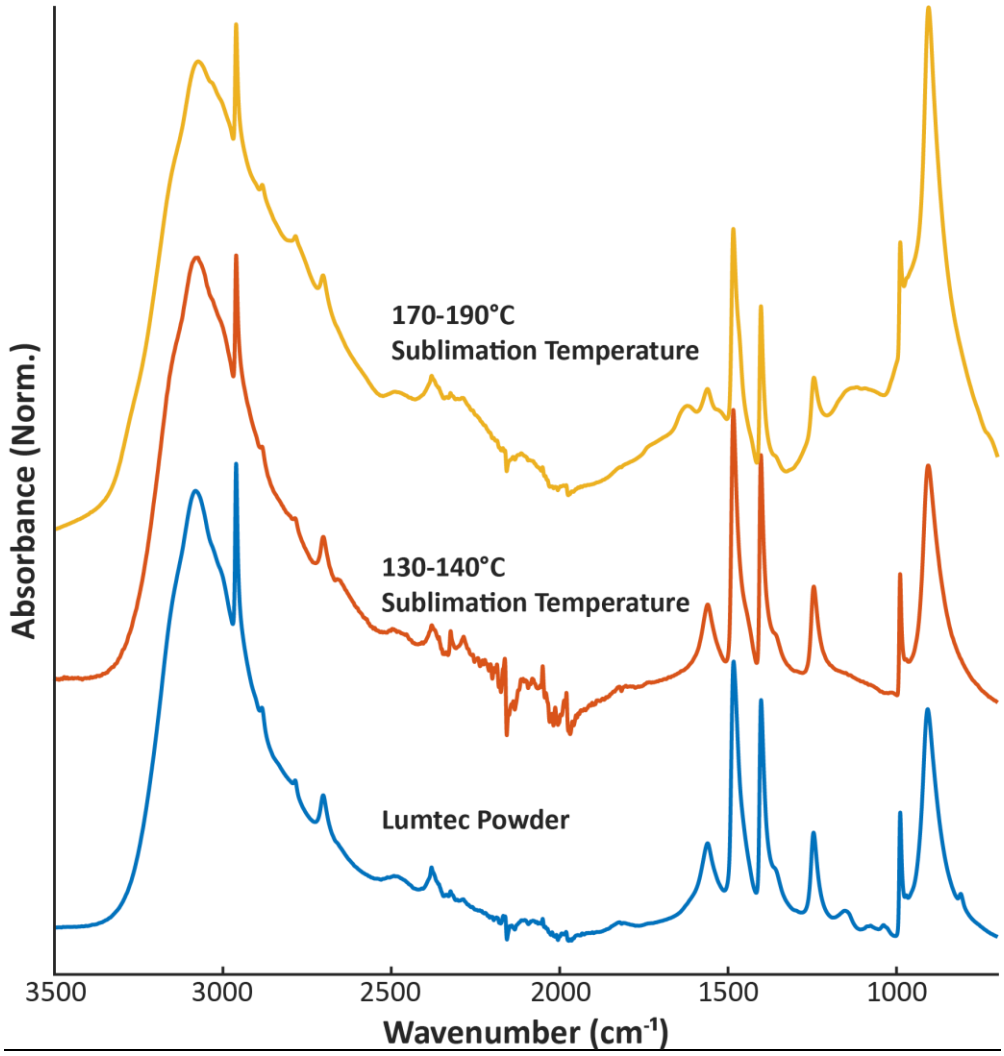

Figure 23. Full FTIR spectra corresponding to the fingerprint regions shown in Figure 14.

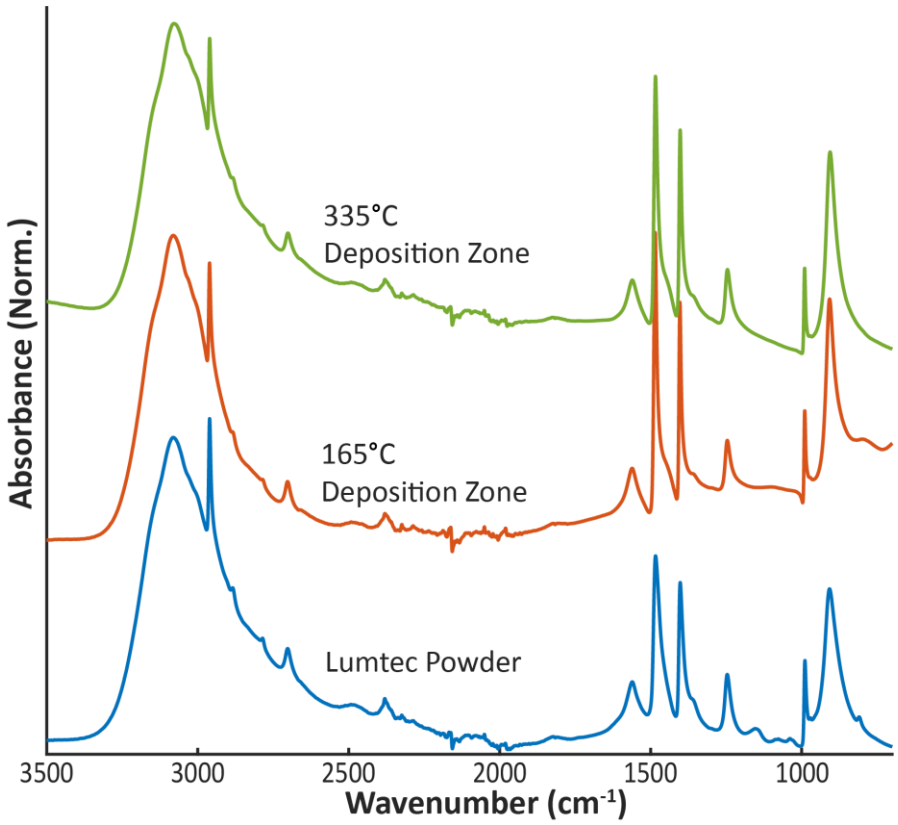

Figure 24. Full FTIR spectra from the fingerprint regions shown in Figure 15.

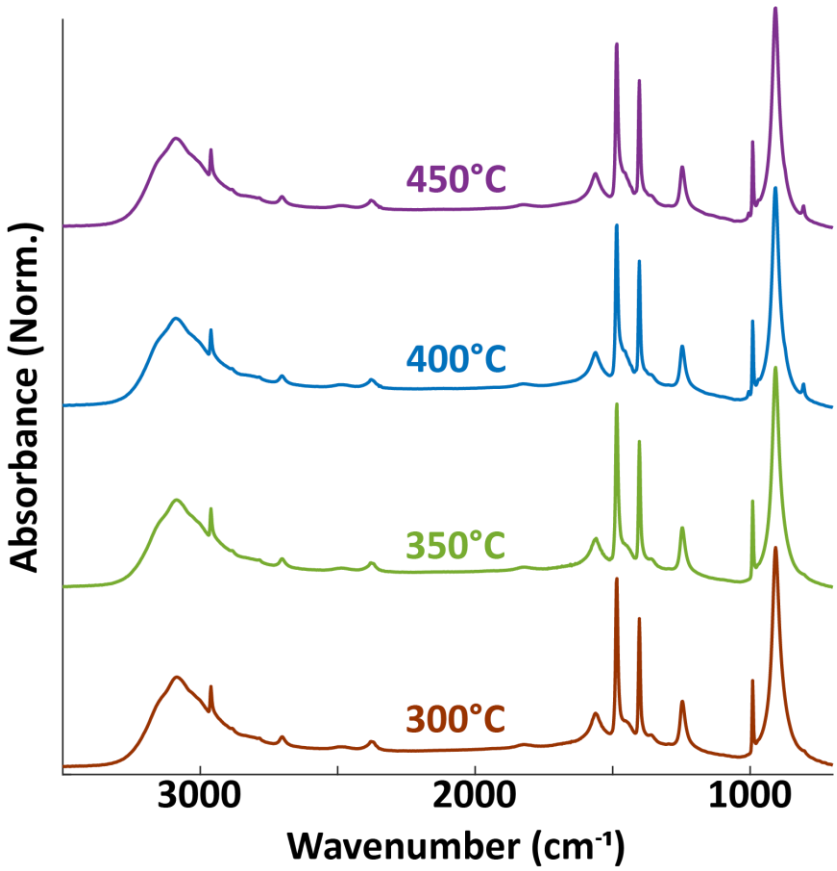

Figure 25. Full FTIR spectra from the fingerprint regions shown in Figure 17.

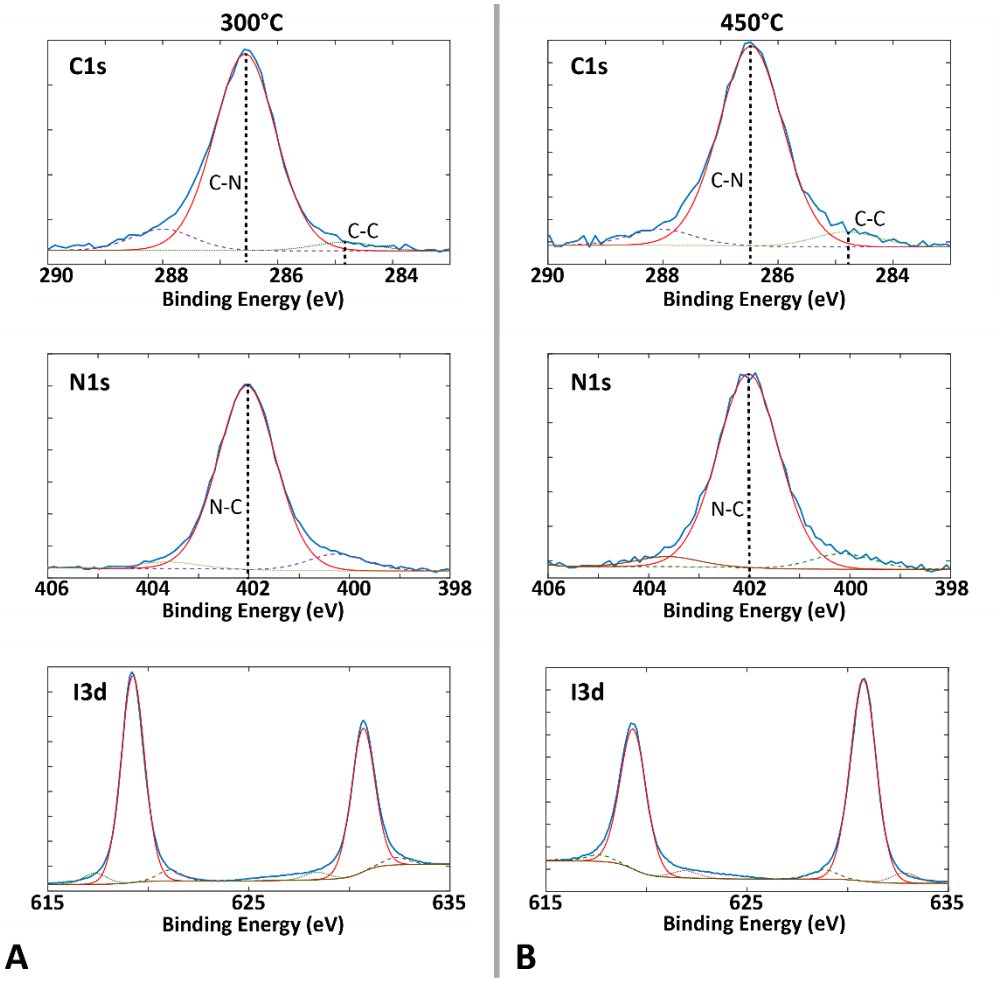

Figure 26. XPS fitting spectra from Figure 18.

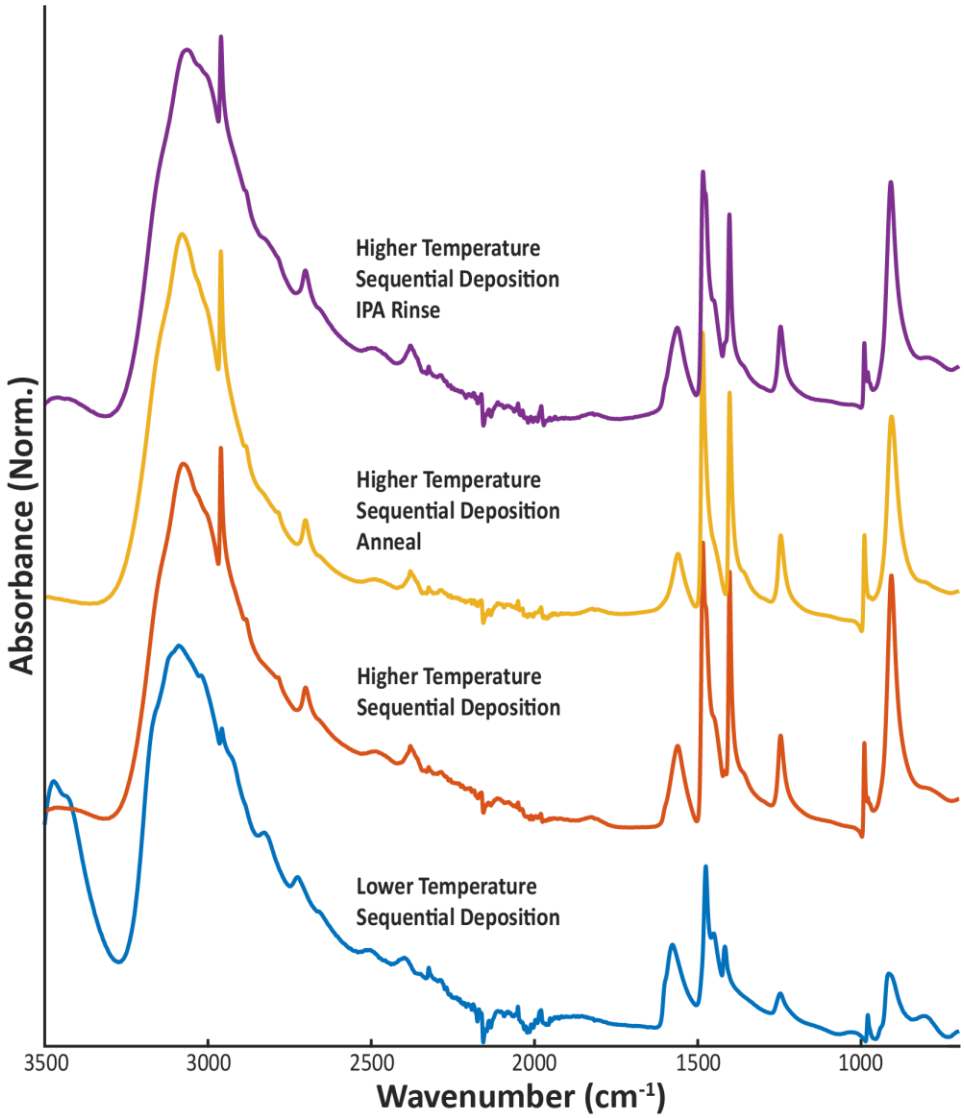

Figure 27. Full FTIR spectra from the fingerprint regions shown in Figures 19 and 21.

4. Design and Construction of a Vapor Transport Deposition System

4.1 Background

Vapor transport deposition (VTD) is a technique similar to organic vapor phase deposition (OVPD) which grows organic films for LEDs[134] and solar cells[135,136], and close space sublimation (CSS) and metal-organic CVD (MOCVD)[137–139] which have been used to produce all-inorganic solar cells. However, VTD combines different techniques to function similarly for both inorganic and organic precursors and can thus be used in hybrid material systems such as organometallic perovskites.

For the first version of a VTD system, we developed a tool for depositing perovskite active areas for solar cells. The system focused on sequential deposition which deposits each precursor materials separately. In contrast, co-deposition deposits all precursor materials simultaneously. The initial VTD system focused on sequential deposition due to the differences in sublimation temperatures for the organic and lead halide precursors. In the sequential reactor design, we placed methylammonium iodide (MAI) and lead iodide (PbI_2) into separate steel capsules and heated the capsules such that the source materials sublimed. Using this technique, we achieved a 10x faster deposition rate than thermal evaporation and produced 6.9% efficient solar cells[140].

Sequential deposition can be desirable when ideal precursor sublimation temperatures, deposition pressures, or deposition gasses are dramatically different. In this case, the reactor can deposit each precursor in its ideal deposition condition without having to make any compromises between unlike precursors. In the case of $MAPbI_3$, the two

precursors have dramatically different sublimation temperatures and the lower temperature material, MAI, is an organic susceptible to degradation. Therefore, most current literature deposits MAI and PbI_2 separately.

However, a switch to co-deposition would increase deposition speed and improve control over the composition of the perovskite film. One of the main challenges of sequential deposition is attaining complete and even conversion of the full film in parallel with building a film thickness with good capability for absorbing light. Similar to a previous VTD system, sequential deposition often has to rely on multiple PbI_2 depositions with MAI conversion steps in order to build up to an active layer thickness capable of absorbing most incoming light. Each of the precursor materials in these paired steps is deposited independently in its own unique set of optimal conditions. Overall, this makes the deposition process longer than with co-deposition.

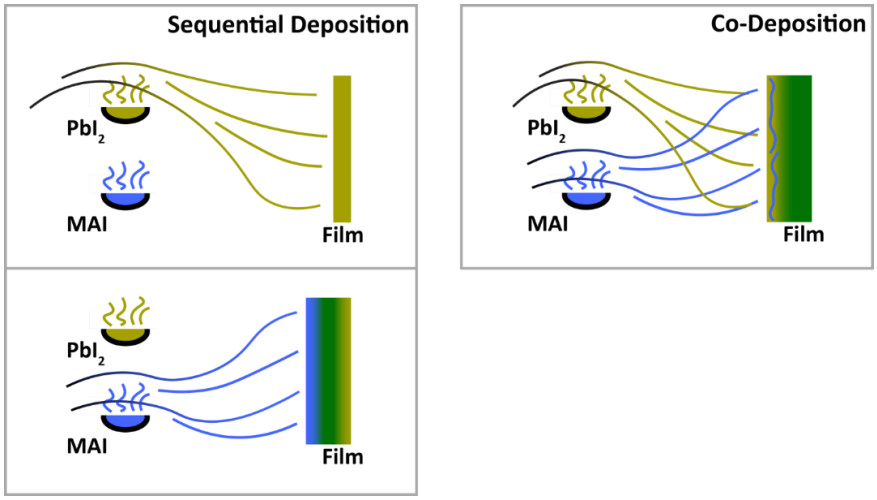

Figure 28. Conversion of a $MAPbI_3$ film with sequential deposition vs co-deposition.

Furthermore, while depositing both materials in parallel the uniformity of conversion throughout the film is higher than a sequential process. With co-deposition, the improved control over the stoichiometry of the perovskite film means that substrate heating during

deposition and post-deposition annealing should not be required[141,142]. This gives an improved control over the final film's composition and makes it easier to produce multi-component films.

Finally, while sequential reactors have been demonstrated using a variety of methods, co-deposition is yet to be fully explored. Here, we design a new, co-deposition-based VTD chamber which increases control over deposition parameters. We develop a novel quartz insert capable of stopping highly diffusive and reactive materials at temperatures above 300°C. To improve control over the deposition process, we will discuss the calculations and simulations behind the fluid flow and heating design. Utilizing improved material control enables the new VTD chamber with a wide range of deposition parameters to improve perovskite film formation for a better film and solar cell performance.

4.2 Prior Sequential VTD Demonstration

Prior to development of a co-deposition chamber, initial VTD trials were performed in a reactor designed for sequential deposition. The initial VTD sequential prototype successfully demonstrated perovskite solar cells with 6.9% efficiency at a 10x increase in deposition rate over thermal evaporation[140]. The system design comprised of three long material arms in which precursor capsules were inserted and through which carrier gas flowed towards a common deposition chamber (Figure 29). Surrounding each material arm, thermal heating tape allowed for a range of deposition temperatures. Care was taken so that the carrier gas reached temperature before interacting with sublimed material. Each precursor was deposited independently of the others, such that there were optimized parameters for each. Thin alternating layers of precursors built up to produce thick, homogenous perovskite films.

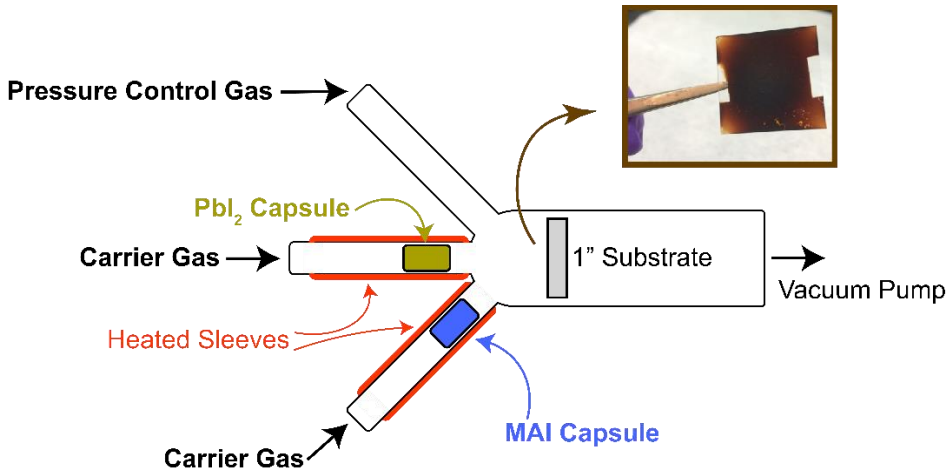

Figure 29. Sequential VTD Reactor Layout. Two separate capsules are aimed at a chilled substrate.

With this sequential design, a linear increase in the amount of PbI_2 deposited would correspond to thicker and thicker $MAPbI_3$ films after MAI deposition and conversion. Under standard deposition conditions for this system, a 1.3nm/s deposition rate was achieved. Negligible time was required for MAI deposition and conversion to perovskite. Using this sequential reactor and technique, perovskite solar cells with the architecture FTO/TiO_2/perovskite/Spiro-OMeTAD/Au achieved 6.9% power conversion efficiency[140] as shown in Figure 30.

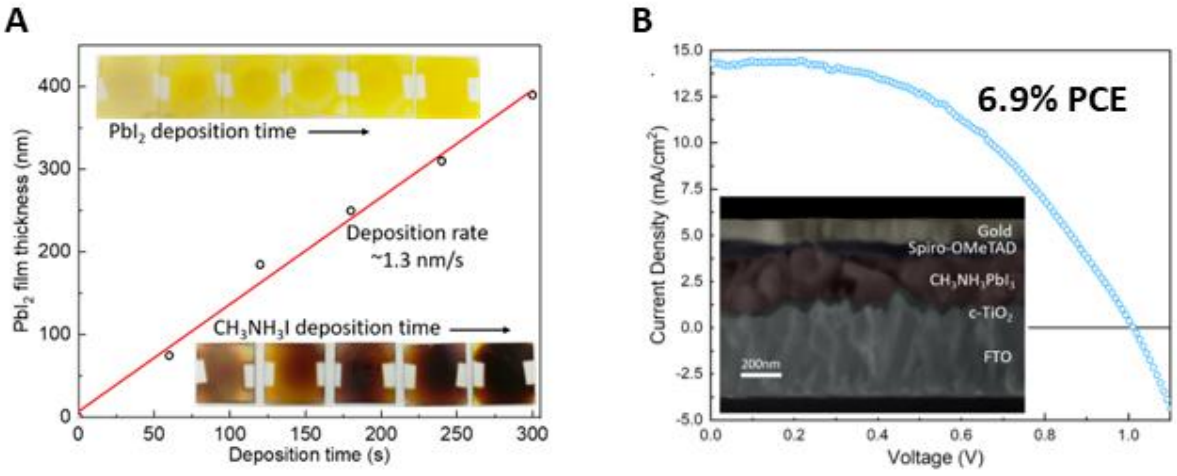

Figure 30. Results from the sequential VTD chamber. A) The deposition rate measured as a function of PbI_2 thickness. B) The resulting record efficiency solar cell using this system[140].

With an experimentally derived deposition rate and initial proof of device performance, a simulation was developed to illustrate the potential deposition speed to show compatibility with a manufacturing process (Figure 31).

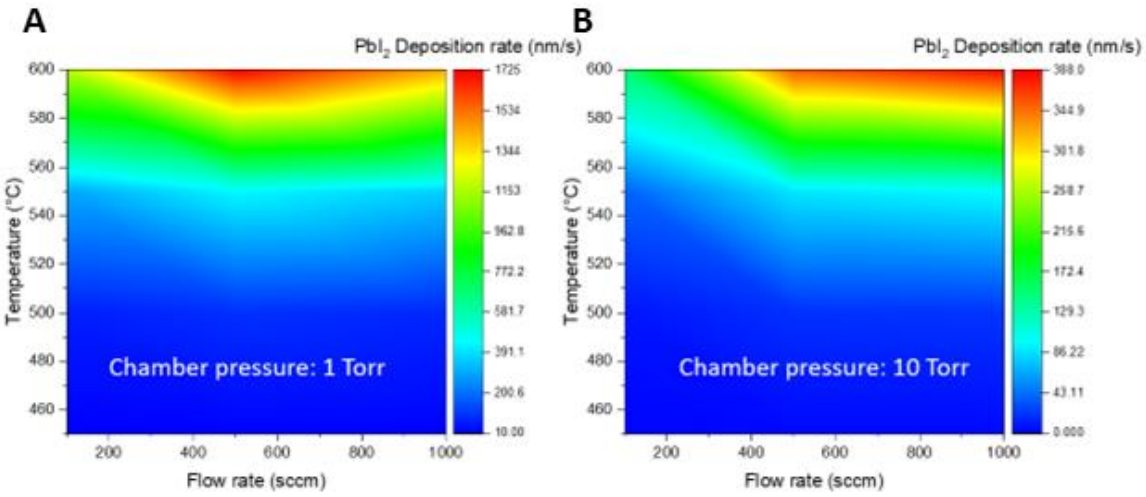

Figure 31. COMSOL Simulations of the sequential deposition system. A) Temperature vs Flow Rate at 1 Torr. B) Temperature vs Flow Rate at 10 Torr[140].

Via decreasing the deposition chamber pressure or via increasing the deposition temperature the deposition rate will continue to increase. By finding a balance between deposition parameters increasing the deposition rate and influencing film properties, simulations and experiments prove promising for sequential VTD as a technique. Although the initial results appeared encouraging, issues surrounding deposition also revealed many design considerations necessary for a next generation prototype.

In the initial reactor, parasitic film growth on the chamber walls determined the deposition process parameters and changing substrates was the dominant contributing factor to deposition time. Due to geometric and loading considerations, the main deposition chamber was not actively heated. Therefore, incomplete heating coverage caused a

significant number of cold spots. As shown in Figure 32, much of the material would condense on the chamber walls before reaching the substrate if the carrier gas flow rate was below a certain amount. As soon as the precursor is lower than its sublimation temperature, it will parasitically deposit.

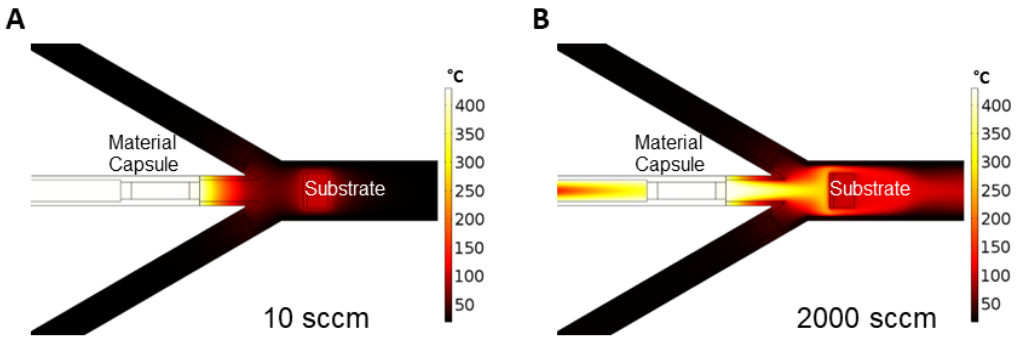

Figure 32. COMSOL Simulations of the temperature within the reactor as a function of flow rate. A) 10sccm flow rate B) 1000sccm flow rate.

In order to get any film growth on the substrate the carrier gas flow rate was increased to over 1,000sccm. As a result, there is less flexibility in deposition parameters than is theoretically possible for VTD.

Lack of flexibility in the deposition parameters also barred co-deposition in this system. When co-deposition was attempted, the MAI component of the film does not deposit over the entirety of the substrate. As Figure 33 demonstrates, due to the use of a hotter carrier gas at a high flow rate for the PbI_2, MAI encountered a heated barrier from most of the substrate. Since MAI requires lower sublimation temperatures and degrades at higher temperatures, the much hotter PbI_2 carrier gas shielded some of the substrate from MAI.

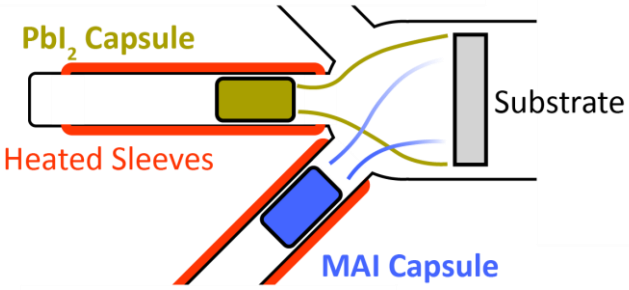

Figure 33. Diagram of heat shield formation during a co-deposition process within the sequential VTD reactor.

So although the sequential reactor was a remarkable first demonstration of the VTD technique, the second iteration needs to address chamber design such that a broader range of deposition parameters is accessible.

4.3 Design Goals and Considerations

Fundamentally, the place to start with any large engineering design is to define the goals and constraints of the system. As outlined in the Sections 4.1 and 4.2, the goals for the new system are as follows:

- Compatibility with Manufacturing
- $MAPbI_3$ Co-Deposition
- Rapid, Safe Sample Changes
- Precise Deposition Control of All Precursors
- Fulfills the assumptions in Chapter 1

In addition to any larger design goals, there are also a number of practical considerations when implementing this design in a real lab setup. For our system the considerations are:

- 1″x1″ Maximum Sample Side

  Although the technique can be applied to much larger substrates, the characterization infrastructure already present in the lab is compatible with a certain electrode layout on a 1″ square substrate. Therefore, to avoid needing to make new characterization setups we will use the standards already present.

- Safety Considerations
  - Fits within a Fumehood

    As a new design, the safety risks of working with sublimed powders, even in a vacuum, is relatively unknown. Therefore to minimize the inhalation risk the system will be placed inside of a designated fumehood.

  - High-Voltage Consideration

    Highly heated components will require high power to operate. Therefore, there is the potential for electrical shorts. The system will need to have electrical safety appliances to eliminate the potential for electrocution.

  - Heated Components

    The highly heated components of the system will be situated in the fumehood to minimize accidental contact with either the operator or other materials.

4.4 System Overview

For a significant product, such as this reactor, the design can be broken down into a series of subsystems. The ensuing development of each subsystem engineers its use but also predicts the integration into a whole. The major components of a VTD system include: vacuum chamber, heating system, and gas/pressure management.

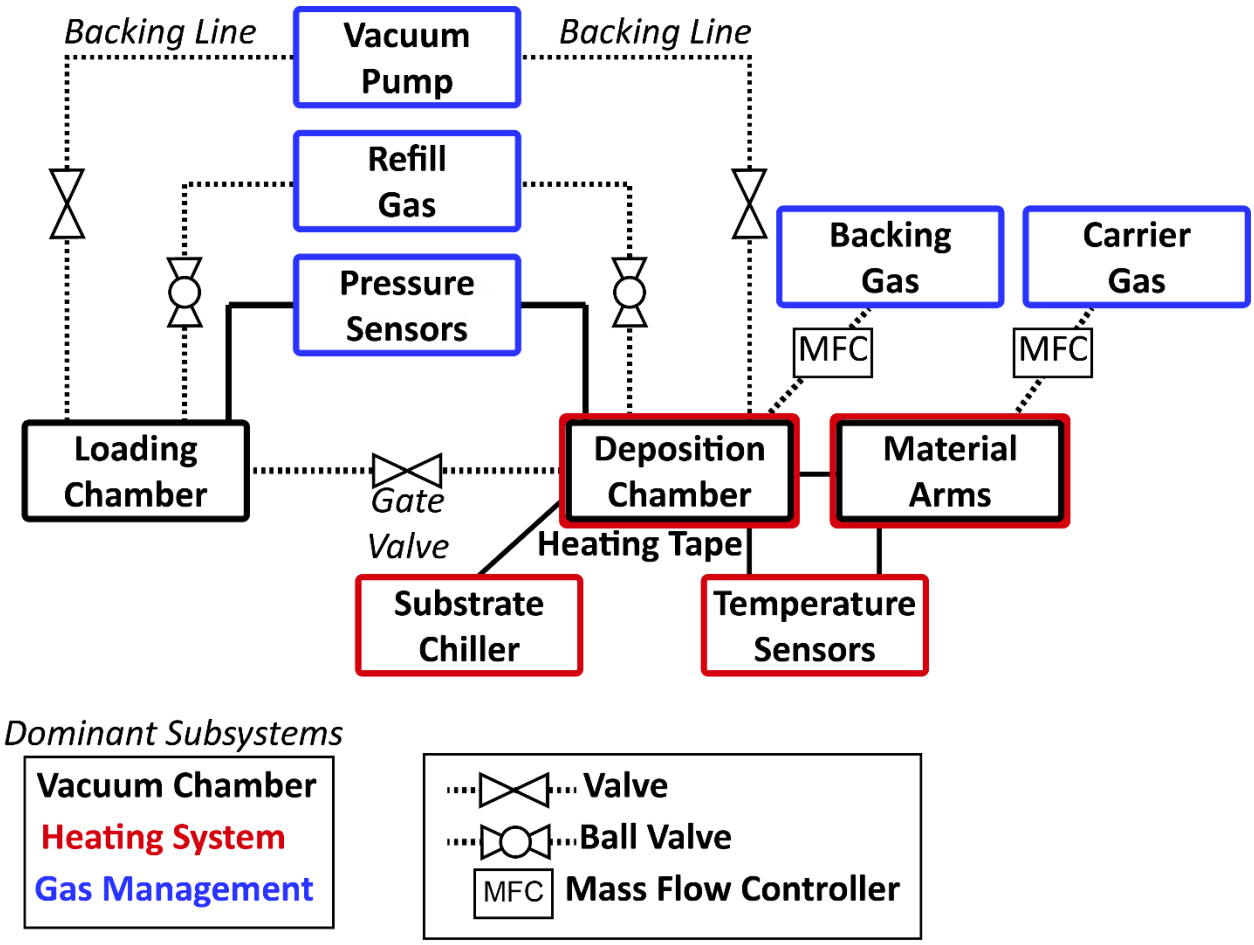

Figure 34. Block diagram of the new co-deposition VTD system.

This manufacturing prototype consists of a series of interconnected subsystems as shown in Figure 34: the vacuum chamber (black), gas management system (multicolor), and thermal control system (red).

- **Vacuum Chamber:**
    - *Goal:* To hold vacuum and allow for rapid sample exchanges
    - *Relation to other Subsystems:* The vacuum chamber is made of two separate chambers including the loading chamber (left) and the deposition chamber (right). Each chamber has an isolated backing line used for pressure management. Independently each chamber can be brought down to pressure or refilled to atmosphere while maintaining a steady state in the

other chamber. A gate valve connects the two chambers and allows for substrates to pass between them. Therefore, it is very closely tied to the Gas/Pressure Management Subsystem.

- **Heating Subsystem:**
    - *Goal:* To maintain precise temperatures within the deposition chamber.
    - *Relation to other Subsystems:* Unlike the other subsystems, the Heating Subsystem is only relevant to the deposition portion of the chamber. It provides the energy necessary for sublimation and joins the Gas/Pressure Management Subsystem in defining deposition parameters.
- **Gas/Pressure Management:**
    - *Goal:* To control the atmosphere and carrier gas within the vacuum chamber.
    - *Relation to other Subsystems:* The gas management subsystem governs the input of carrier gas into the deposition chamber, regulated by mass flow controllers. It is related to the Vacuum Chamber by running the substrate exchange process and gasses within the reactor. Additionally, it combines with the Heating Subsystem to produce the full range of deposition parameters.

Consequently, each subsystem influences the performance of the other. The design and practical construction considerations for each subsystem require a dedicated discussion. The next few sections give the details behind the Heating Subsystem and Gas/Pressure Management design.

4.5 Gas and Pressure Management

Controlling the atmosphere within a reactor has tremendous impact on the growth process and final film quality. The starting base pressure of the system dictates the purity of the deposition gasses, adhesion, and final film properties[143,144]. Then both the carrier gas flow rate and deposition pressure influence the perovskite film[145,146].

There are two main stages for a full deposition, the substrate loading/unloading and the deposition itself. During substrate loading/unloading the reactor is designed to maintain an almost deposition style fluid flow via strategic positioning of the vacuum port (Figure 35).

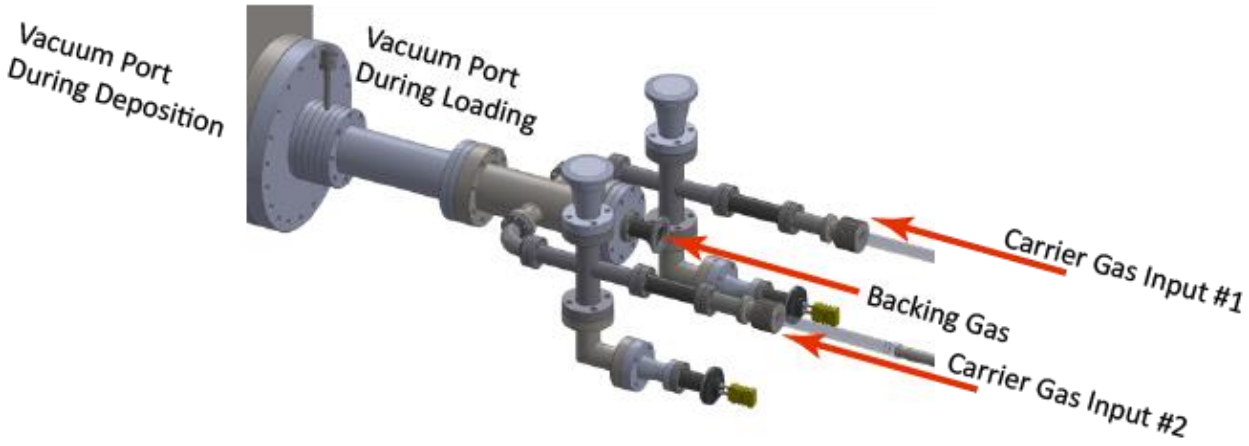

Figure 35. CAD of the material arms and deposition chamber specifically highlighting the gas and pressure management systems.

Then during deposition, the vacuum port is switched to a location inside the loading chamber to allow for a uniform flow around the substrate holder which is located just deeper into the chamber than the other port.

To maintain a carrier gas flow independent of deposition pressure, the system must be able to conserve a much lower pressure than the targeted deposition pressure while heated. To do that, the roughing pump used must be slightly overpowered for the system, Figure 36 shows base pressures under different levels of deposition temperatures.

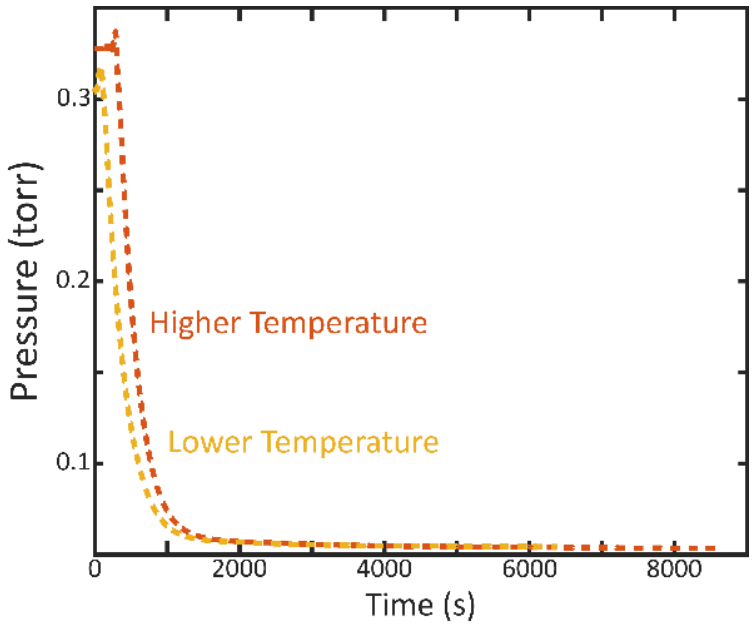

Figure 36. Pumpdown times and base pressure reached as the reactor heats up to deposition temperature and while that temperature is maintained.

Different temperatures can induce different base pressures as materials absorbed on the chamber sidewalls start to evaporate or flange seals start to break down. In our case, the chamber can handle a range of temperatures used in depositions with nominally the same base pressure.

Then, to set the actual deposition pressure a backing gas is used as shown in Figure 35 that increases the pressure to what is desired. The increase in pressure from a combination of the carrier gasses and backing gas set the deposition pressure and are regulated by mass flow controllers for a steady input.

When designing the system for the target pressure and carrier gas flow rates, it is important to consider the resulting hydrodynamic regime the reactor will operate in. As the pressures during deposition are relatively high, we will always be able to operate within the laminar flow regime.

4.6 Thermal Management

Similar to controlling the carrier gasses and pressures present within the system, thermal management plays a critical role in material transport and film growth. In this case, the temperatures used in the system are dictated by the sublimation temperatures of the precursor materials used, examples shown in Table 2.

		Sublimation Temperature (°C)
Organic	MAI	160
	FAI	145
Inorganic	PbI_2	370
	$PbBr_2$	400
	CsCl	430

Table 2. Optimal sublimation temperatures for a variety of organic and inorganic perovskite precursors.

As previously determined, our system will be designed to handle MAI at 160°C and PbI_2 at 370°C. Therefore, each material arm will be designed for the temperatures of its specific precursor but the PbI_2 necessary temperatures will dominate the deposition zone other than the substrate. Heating of the vacuum system and cooling of the substrate require very different techniques so will be discussed in turn.

4.6.a Chamber Heating

As shown in the previous sequential deposition chamber (Section 4.2), thermal management within the reactor is critical to maintaining sublimed material and thus enabling a large range of deposition parameters. Figure 37 shows two critical elements to designing the reactor.

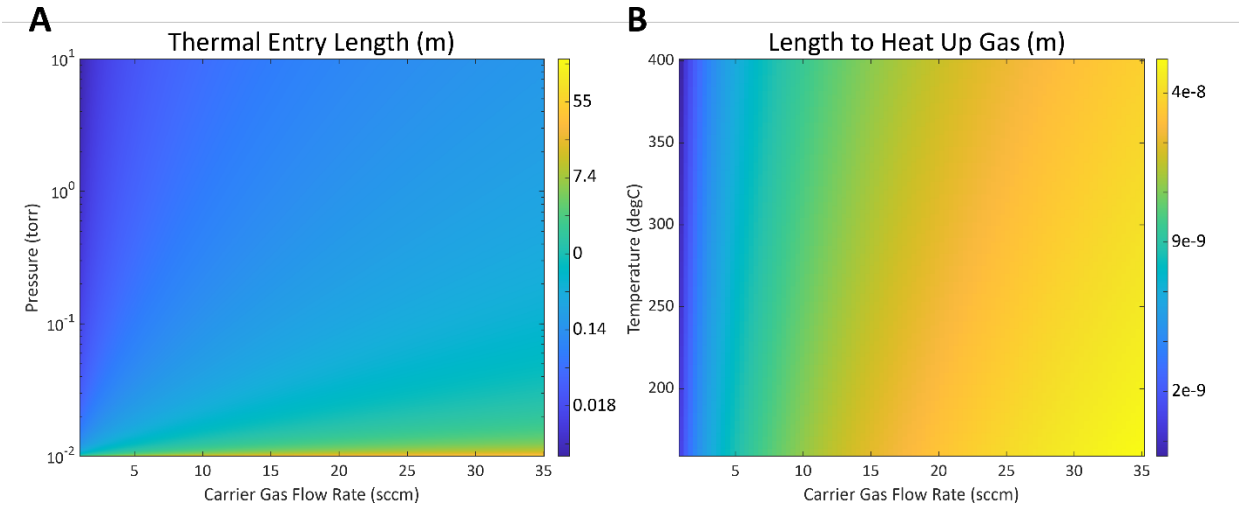

Figure 37. Thermal COMSOL Simulations of the co-deposition VTD reactor. A) The Thermal Entry Length for a variety of carrier gas flow rates and deposition pressure parameters. B) The tube length required to heat up a carrier gas to chamber temperature. In the deposition parameter space presented, the creation of a uniform thermal boundary layer throughout the tube requires much more distance than heating the carrier gas.

The first graph shows the thermal entry length which is analogous to the hydrodynamic entry length. However, the second graphic expands upon that concept using Equation 10 from Section 1.2.b to calculate the length of tube required to heat the carrier gas to the sublimation temperature. Based on the deposition parameter space the reactor is designed to operate in, the length to heat up the gas is minimal compared to the length required. Therefore, the reactor should be designed for the thermal entry length rather than the length required for heating.

However, uniform heating of the chamber is complicated since the deposition chamber is made of mostly off-the-shelf vacuum components for ease of implementation elsewhere. Therefore, there are a plethora of flanges that provide variable thermal masses that all need to be at a consistent temperature (Figure 12). As a result, many thermocouples implanted into the outer, heating sections and the chamber is broken down into many different heating zones which corresponded to either the thermal mass or temperature requirements. Important thermocouple temperatures include:

D2: Location of the substrate during deposition

PJ/MJ: Junction between the material arm and main deposition chamber

P4/M4: Outer thermocouple corresponding to the precursor sublimation temperature

PS/MS: Inner thermocouple corresponding to the precursor sublimation temperature

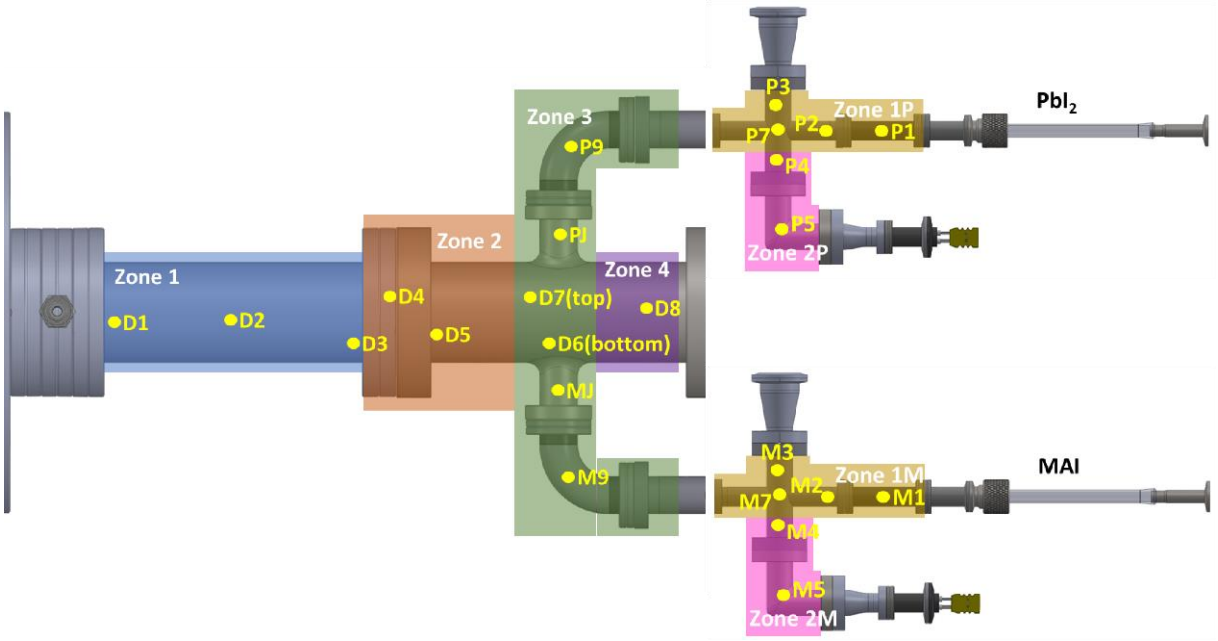

Figure 38. Location of the different heating zones and thermocouples. Each heating zone can be heated independently of all the others.

To assist in tracking important temperatures during deposition, a thermocouple recorder was used for 11 of the different thermocouples including D2, D7, MJ, M9, M7, M4, MS, PJ, P9, P4, PS. These thermocouples are chosen to watch the deposition temperature at the location of the substrate but mostly to ensure constant temperatures throughout the material arms.

With the tracked thermocouples we can do in-depth analysis of how the system heats up and the exact temperatures during deposition (Figure 39).

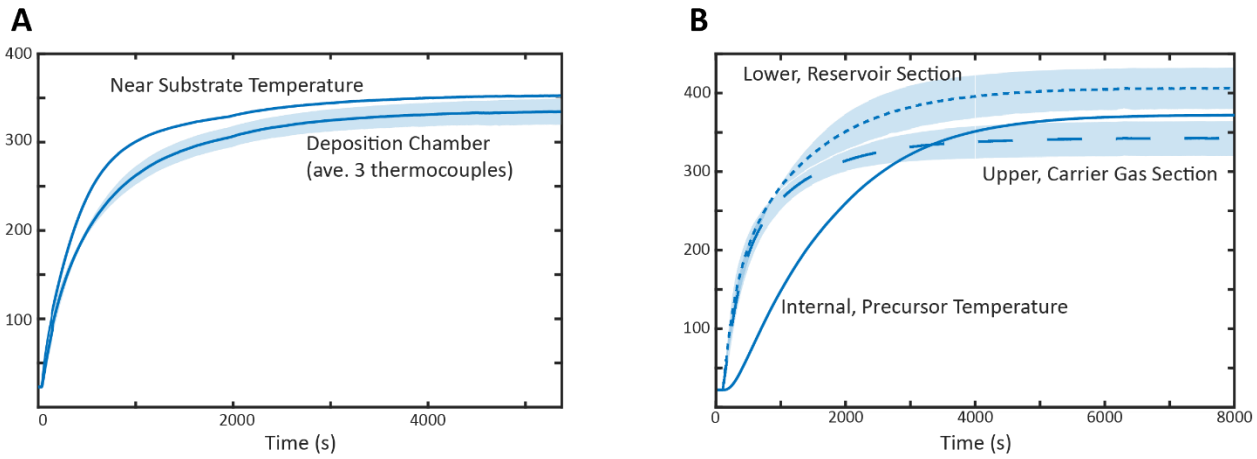

Figure 39. Thermocouple readings from the VTD system during the warmup process. A) Thermocouples outside of the chamber corresponding to the deposition chamber temperatures. B) Thermocouples inside and outside the chamber corresponding to the temperatures within the PbI2 material arm.

Figure 39.A displays the deposition chamber temperature during the heating and deposition processes. Then, Figure 39.B highlights the heating and temperature distribution if we focus the thermocouple recording on only one material arm. These recordings demonstrate stability and a <15°C spread once at deposition temperature.

4.6.b Managing Substrate Temperature

Since the rest of the reactor must remain above sublimation temperature for adequate material transport, choosing an appropriate substrate temperature below that threshold has wide-ranging consequences from influencing conversion and precursor film deposition rates to film formation[50,51,145,147]. Since our precursors have already been determined, we can look to the lower sublimation temperature material (MAI) and manufacturing compatibility with flexible, plastic substrates to define the upper range in our system to be 110°C. Currently, many CVD perovskite deposition processes currently use substrate temperatures ranging from 70-220°C[148,147,149] depending on the types of precursors used. In contrast, most thermal evaporation processes do not directly control their substrate temperature[29,44].

Therefore, since substrate temperature influences the film growth in the vapor phase, we design to allow for a range of substrate temperatures. Figure 40.A shows the substrate mounting scheme to the substrate arm that moves in an out of the chamber. The substrate is mounted via a mounting plate that evenly presses on all four edges of the substrate to hold it tight to the chilling block. Then the whole fixture screws onto the chilling arm. A 50/50 mixture of ethylene glycol and water is chilled and circulated through the substrate arm in order to maintain a certain deposition temperature. Thermal pads between rigid surfaces aid in the convective heat transfer.

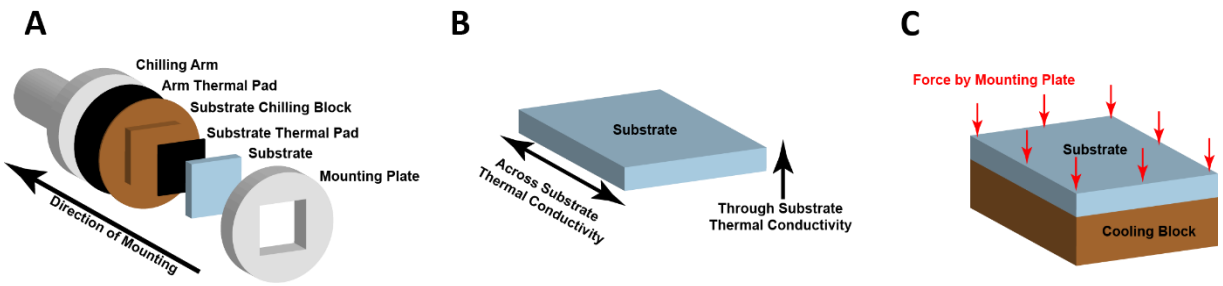

Figure 40. The current substrate mounting scheme and it's specific challenges. A) The current substrate mounting scheme to the cooling block. B) Highlighting the different types of thermal conductivity within a substrate. C) The forces experienced by a substrate during mounting to the cooling block.

However, as Figure 41 illustrates, the types of substrates used in the system greatly influence the chilling uniformity and capabilities. Substrates such as silicon have high thermal conductivity across the substrate. Therefore, even if the substrate is not uniformly seated on all areas the substrate is still a uniform temperature across it. Other substrates such as glass have low conductivity in all directions. Since through substrate is thinner than the width, if a certain point is touching the chilling block and another is not, then one area will be colder than the other. Furthermore, it is important to consider how substrates both transmit heat through the substrate and across different areas of the substrate. Additionally, for silicon vs glass, glass samples have a higher bend radius than silicon. Consequently, when pressing on all edges of the substrate, a glass substrate will more easily bend upwards in the middle as shown in Figure 40.C. These considerations are demonstrated with MAI-only films.

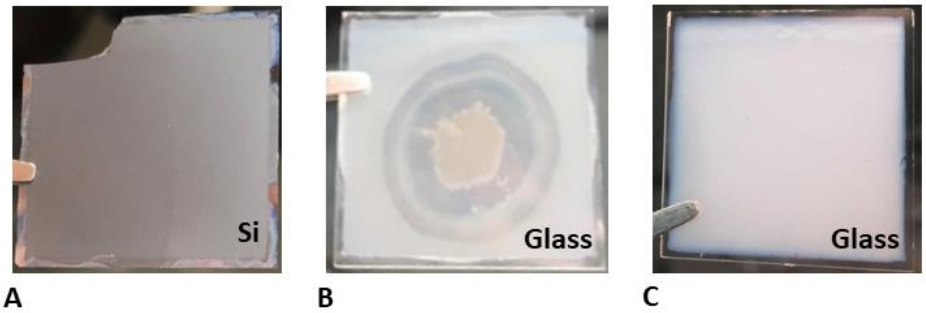

Figure 41. Deposition of MAI on different substrates using slightly different thermal pads. A) Deposition on a silicon substrate. B) Deposition on a glass substrate with rigid thermal pads. C) deposition on a glass substrate with conformal thermal pads.

Figure 41.A and B, the same mounting and deposition scheme is shown on different substrates. As discussed previously, due to the higher thermal conductivity and lower ability to bend as a result of mounting, the silicon substrate show a uniform film while the glass substrate exhibits ringing. For Figure 41.C, a compressible, conformal, high-temperature thermal pad was used to ensure that uniform heat was dissipated from the sample in all areas.

However, compressible thermal pads are most frequently made of polymers embedded with non-conductive materials or silicone. This means that frequently the thermal conductivity of the thermal pad is not nearly as high as some incompressible thermal pads such as graphite. In our substrate mounting scheme the substrate thermal pad is made of a compressible graphite sheet while the arm pad is made from a compressible pad. This was found to be the best combination to get the best thermal transfer between substrate to chiller with the calibrated temperatures found in Figure 42.

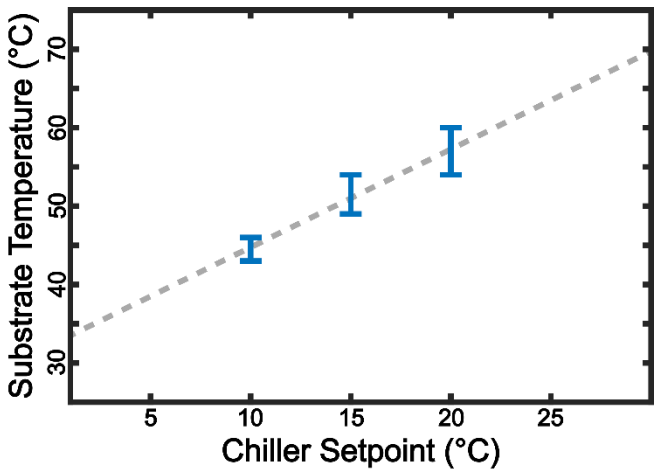

Figure 42. Calibration of the chiller setpoint to the actual substrate temperature. The dotted gray line corresponds to extended chiller setpoints.

With the current configuration, the substrate is able to access between 35-60°C during deposition. A linear interpolation between the points indicates a uniform thermal transfer coefficient within these parameters.

4.7 Precursor Material Handling

Creating high quality films within devices oftentimes depends on the interface between that film and other materials. If there is parasitic deposition before or after the intended deposition process then the interfaces between the film and the surrounding layer changes[110,150], sometimes unpredictably. Additionally, there have been demonstrations that the presence of stainless steel around specifically the MAI precursor can result in the presence of iron from the stainless steel in the final film[151]. In order to get a high quality and reproducible film impurities incorporation needs to be minimized. Therefore, the areas with the highest concentration of precursor materials need to be protected from impurities. Finally, sublimation relies on high temperatures, so the parts associated with sublimation need to be able to withstand that temperature over many depositions. As a result, the four basic criteria for our valve are to prevent parasitic material leakage and deposition, to prevent reaction of the chamber wall and boat with precursor materials, to

repeatedly function at temperatures up to 450°C, and to be compatible with manufacturing.

Current vacuum deposition systems rely on the use of material boats and shutters in order to control when deposition occurs. In thermal evaporation, boats hold material, and are then resistively heated to evaporate material onto a substrate. As a line-of-sight deposition process, thermal evaporation only requires a chamber shutter below the substrate to prevent parasitic deposition on the substrate. Similarly in chemical vapor deposition (CVD) furnaces, shutters prevent the gasses from reaching the substrate and reacting before the intended time. The concern about high temperatures and reaction with metals prompted some groups to work with quartz CVD furnaces. However, quartz furnaces are not able to scale to large-area manufacturing tools. Additionally, there is significant parasitic deposition from the uncovered source before the carrier gas is turned on. However, these available valve and boat techniques on the market today do not always meet the needs of VTD chambers, especially when used with typical perovskite precursors such as metal halides or organic components. Table 2 gives a summary of valves and boats used to control precursor deposition.

		Controls Deposition	Non-reactive with Precursors	High Temperature Compatible (>200°C)
Valves	All-Metal Valve	✕		
	Harsh-Process Valve	✕		
	Glass	✕	✕	
Material Boat	Knudsen Cell			✕
	Baffled Boat			✕
	Ceramic Crucible		✕	✕
	Quartz Boat		✕	✕

Table 3. Overview of different valves and material boats currently on the market. X's mark where different techniques fit our requirements.

Therefore, to develop our VTD tool we have to develop mechanisms that can be used with perovskite precursors on a manufacturing scale while allowing for precise delivery of the material to the substrate. Unfortunately, no product on the market fits our needs. Our new system requires materials that do not react with MAI, vacuum-tight sealing, and over 200°C working temperatures. Off-the shelves vacuum valves, material boats, precision bore tubing, and quartz valves only partially fulfill the functionality necessary for perovskite VTD. Using one singular off-the-shelf technique will not be feasible as we continue to push the limits of thin film manufacturing into a design that not only has applications in VTD but in related fields.

Since much of the technology on the market today fit aspects of our needs, we combined several related tool designs to create a new instrument. The main body of the material holder is made of stainless steel with a snug fitting quartz insert to control the material while minimizing unwanted reactions.

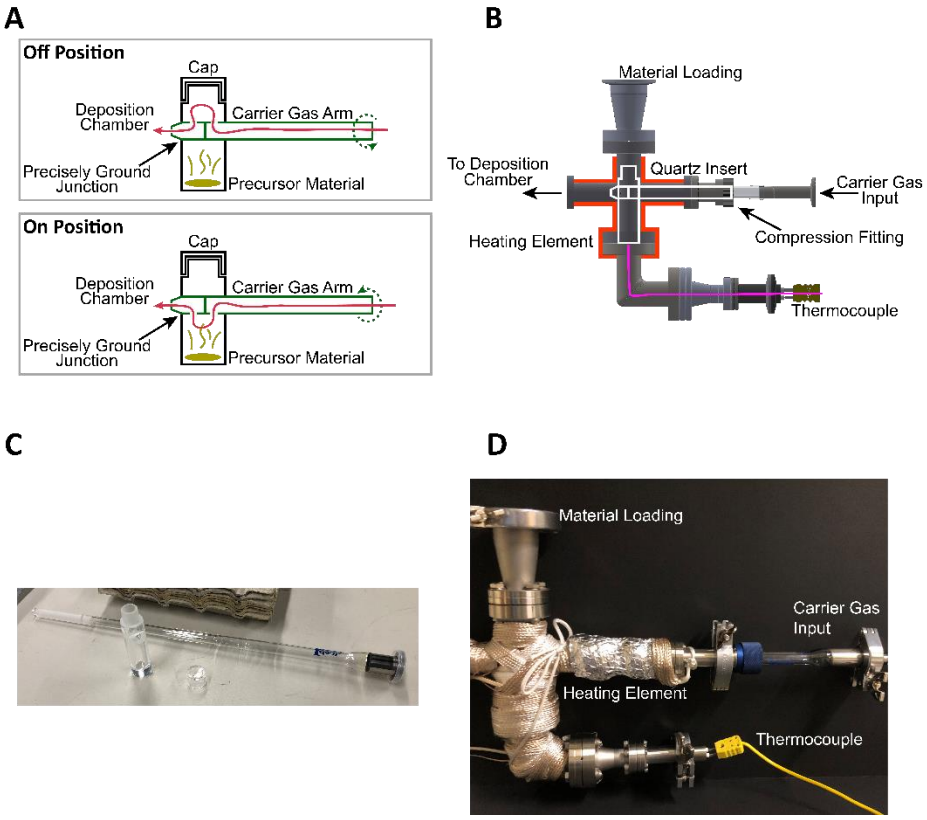

Figure 43. High-temperature quartz material reservoir design. A) Quartz-based insert in the on and off positions with carrier gas. B) Quartz material reservoir inserted into a stainless-steel chamber approximating it's use on a manufacturing line.

Specifically, the insert is made out of two modified quartz precision bore tubing pieces. As shown in Figure 43.A, the green tube is the inner of the precision bore tubing while the black segments are the outer chambers. The green inner tube is used for carrier gas injection. Close to the end of the quartz tube is a wall that directs the carrier gas flow into the selected chamber and back into the green carrier tube before entering the deposition chamber. The black outer sections are separated into two different small chambers. The top chamber is covered with a quartz cap and is used as a material bypass. The lower chamber is a material reservoir that contains the precursor power heated to sublimation temperature. In the Off Position, the valve closes by rotating the openings on the green carrier gas injection tube to pass through the bypass chamber. Then when the valve is turned to the On Position, the holes face the precursor material reservoir and a carrier gas is allowed to flow through the sublimed vapors and out into the deposition chamber.

The material reservoir is designed to not only hold the solid precursor as it sublimes, but also to enable deposition in the equilibrium regime. Directing flow of the carrier gas through the material reservoir chamber sends it through a region saturated with precursor vapors and therefore pushes deposition towards the equilibrium regime. Depositing in the equilibrium regime is favorable especially in co-depositing more than one precursor because it is not tied to sublimation temperature. In the kinetic regime, deposition rates increase with temperature because more material will start subliming. However, increasing temperature of precursor material quickly causes degradation of that material. Through depositing in the equilibrium regime we are able to tailor composition of films by controlling the deposition rate of different precursor materials through their carrier gas.

The quartz insert design is shown in Figure 43.A, but during use it is inserted into a stainless-steel vacuum chamber as shown in Figure 43.B. The quartz valve must fit snugly into the stainless-steel chamber. Since the heating of the systems is done from outside of the chamber any gaps between the quartz and stainless steel will result in significant thermal loss. Positioning the quartz inside of the stainless steel is critical because different thermal expansion coefficients for the quart and stainless steel could damage the equipment. The quartz tube component is terminated with a stainless-steel flange which is vacuum sealed to the outside of the chamber via a compression fitting in what is standard techniques.

This quartz design has been built (Figure 43.C) and is currently in use in our lab as shown in Figure 43.D. We have successfully heated up material and prevented deposition for 45 minutes. After rotation we have deposited films 100s of nanometers thick over a one inch square substrate with the size of the current material reservoir. The quartz insert has been operating successfully at temperatures around 400°C and pressures below $5x10^{-2}$torr.

To further investigate the material holder's capabilities, we designed a simulation using the finite elemental analysis software COMSOL. Since we designed to operate the system to use the carrier gas as the primary determinant of deposition rate, we assume operation in the laminar flow regime and with a dilute amount of precursor material.

In the model, the two influential components to accurately describe are the sublimation of the precursor material and the transport of that material out of the material holder into the main chamber. To find this rate, we can combine the Hertz-Knudsen Equation, Clausius-Clapeyron Relation as previously described in Chapter 1.

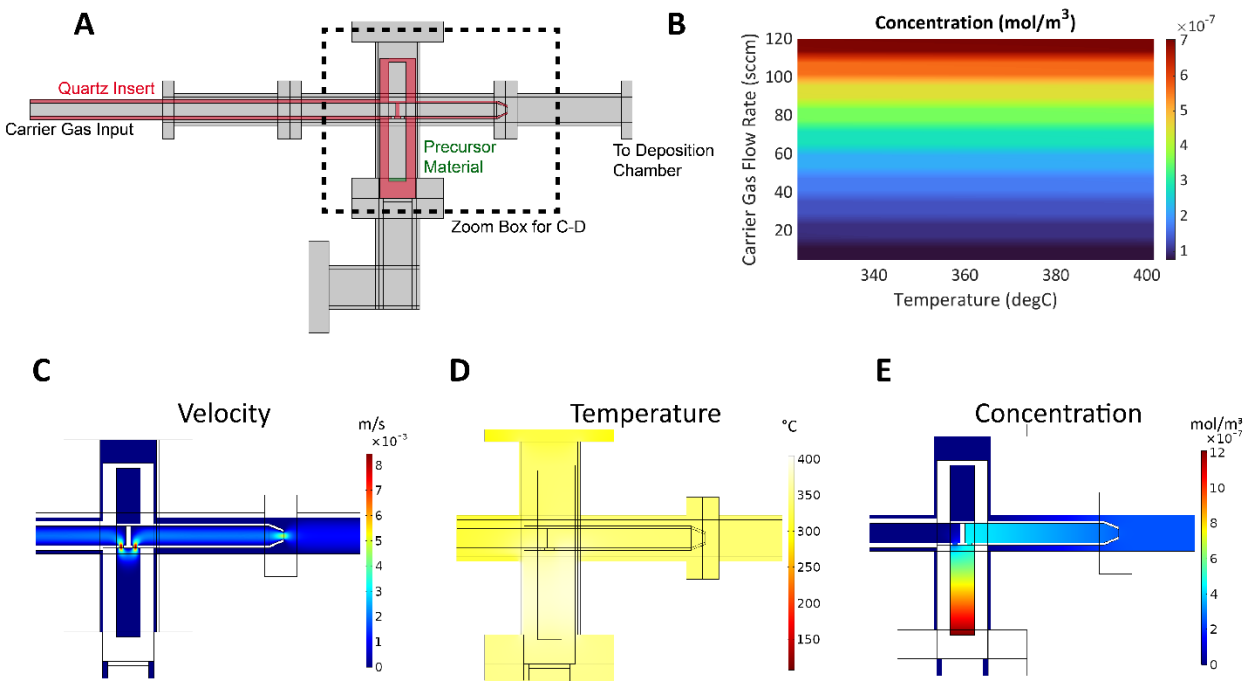

Figure 44. COMSOL Simulations of the PbI2 material arm. A) The geometry used in implementing the simulation. B) The range of deposition parameters and resulting PbI2 concentration. C) An example of the velocity profile through the material arm using the Zoom Box from A. D) An example of the temperature profile through the material arm using the Zoom Box from A. E) An example of the concentration distribution through the material arm using the Zoom Box from A.

Figure 44.A shows the geometry used in the COMSOL model with the quartz insert highlighted in red, and the precursor material location in green. Using the laminar flow, heat transfer, and dilute species concentration modules, we simulate the inner workings of the material arm as it occurs during deposition. Experimental data and constants used in the model is presented in the SI. As seen in Figure 44.C, the velocity profile out of the quartz insert nozzle rapidly reaches a continuous, stable flow. Through careful wrapping of the material arm stainless steel chamber with heating tape and 8 thermocouples we allow for consistent heating throughout (Figure 44.D). High concentration of the precursor material is successfully contained to within the quartz section of the material arm to minimize any potential degradation due to the reactive iodine subcomponent. Therefore,

this new material arm design will allow for a wide range of deposition parameters while meeting our requirements.

4.8 Full Design and Operation

Now that there is a method for precise controlling of the wide range of precursors and designs for the critical elements of material transfer, we are ready to describe the integration into a full VTD system. Figure 45 steps through the design of the full system.

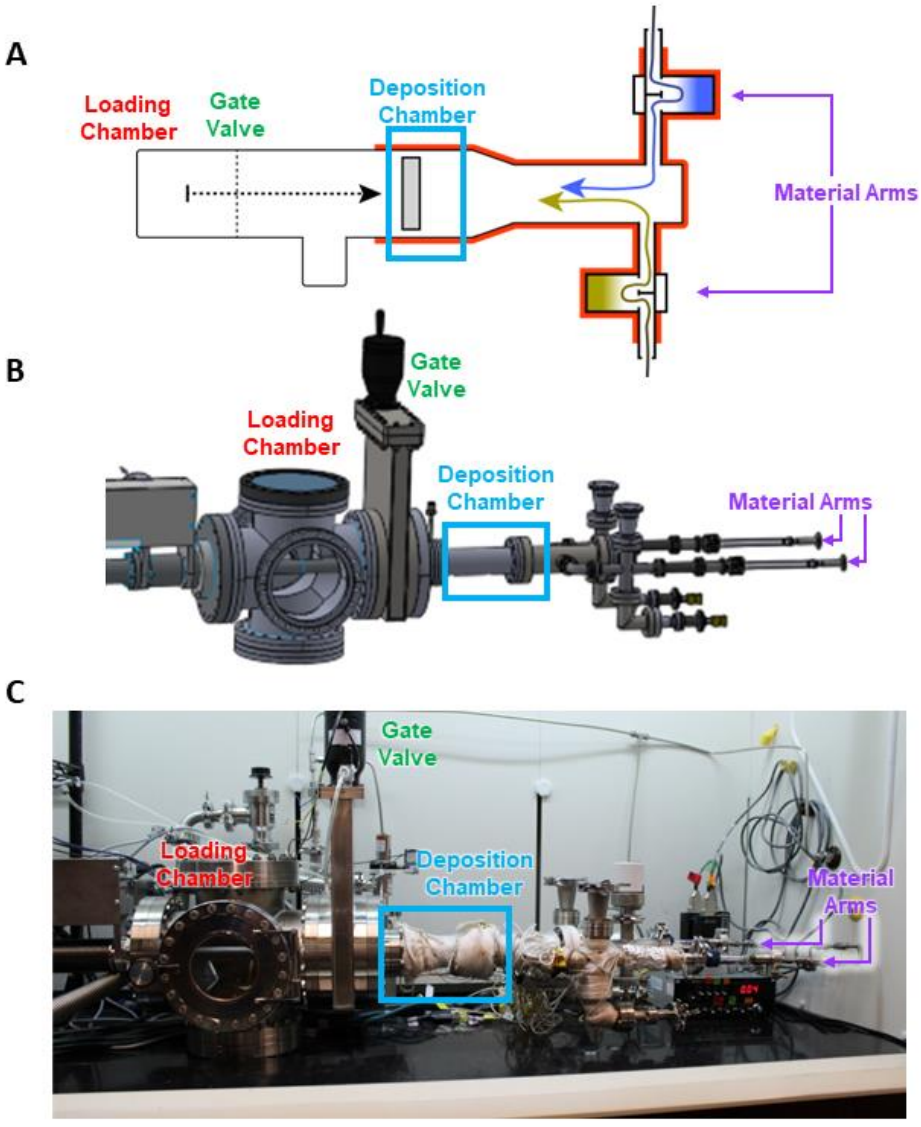

Figure 45. Progression of more and more specific VTD system diagrams. A) A diagram of the general layout of the VTD system. B) A CAD drawing of all parts of the vacuum chamber used. C) An image of the implemented VTD system.

Currently the system is setup with two different precursor material arms in order to deposit $MAPbI_3$. Each precursor has a unique material arm with its own carrier gas source as shown in blue for MAI and gold for PbI_2. By using individual precursor material arms, the system can tailor the deposition parameters to be specific to that material. The substrate is moved via a stage from the loading chamber and into the deposition chamber (indicated by the dotted arrow). A moving stage allows for quick substrate changes without cooling down the chamber. The resulting CAD is shown in Figure 45.B, with external components omitted.

Figure 45.C is an image of the fully constructed system. The material arm and deposition chamber geometry allow for continuous heating from the input of the carrier gas until slightly past the substrate. The wrapping style and amount of heater tape is tailored to both the geometry and thermal mass of each chamber section with ~25 total thermocouples checking for thermal variation. A thorough description of the thermal management system is given in Section 4.6. The systematic and continuous heating allows for a decrease in the carrier gas flow rate for both material arms. This in turn gives a wider deposition range for both the carrier gas flow rate and pressure as discussed in depth in Section 4.5.

Additionally, putting all these subsystems together allows for a full view of the deposition process. In order for rapid switching of substrates with minimal influence to both temperature and fluid flow, there is a before deposition state and during deposition state defined as shown in Figure 46.

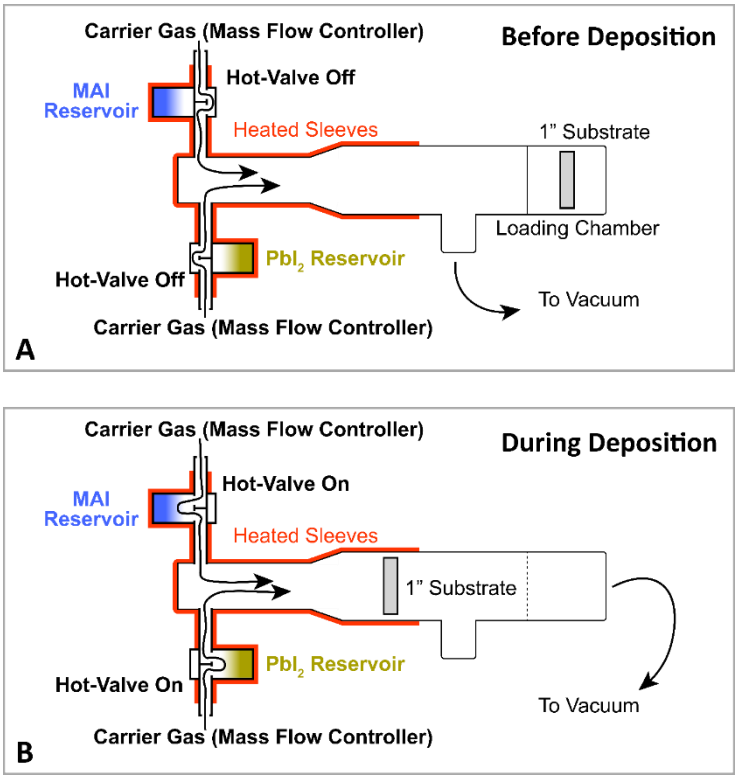

Figure 46. Diagram of the changes to the system before and during deposition. A) The system before and after deposition. B) The system during deposition.

Before deposition the substrate is in the loading chamber with the gate valve closed. Carrier gas can flow through the system in a mimic of during deposition by using a port situated very close to the gate valve. Then when deposition occurs, the gate valve is opened and the substrate is translated into the heated deposition zone and vacuum is pulled from the loading chamber. A full operating procedure is included in Appendix B.

4.9 Full System Simulation

The goal of designing simulations for a vacuum system is a more thorough understanding of the inner workings and influential design parameters before construction or during operation. In our specific situation, we want to understand several significant design choices and the potential limitations to deposition parameters. In our case, we decided to

use the finite elemental analysis tool COMSOL. Within COMSOL we used the laminar flow, heat flow in fluids, and dilute species modules to replicate a simplified version of the co-deposition chamber as shown in Figure 47.

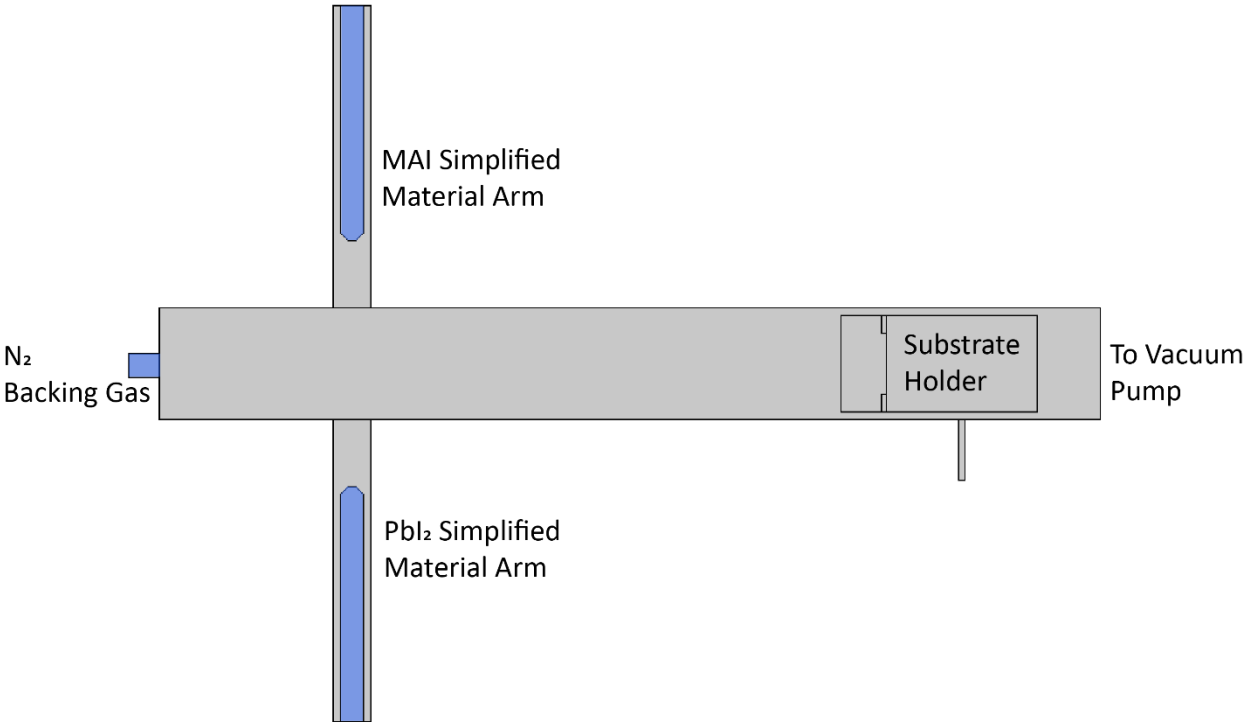

Figure 47. System geometry used in the COMSOL simulation.

While accurate to the dimensions and materials of the real system, the model is simplified in a number of ways. The external stainless-steel chamber in this instance is not simulated, since unlike in Section 4.7, we are focused on the gas flow and resulting precursor flux within the chamber. Additionally, since we simulated in detail the material arms already, we simplify their geometry to focus on the deposition chamber.

To start, since we are assuming that the heat profiles within the system are accurate to their section, we focus on the carrier gas flow and how that translates into precursor flux.

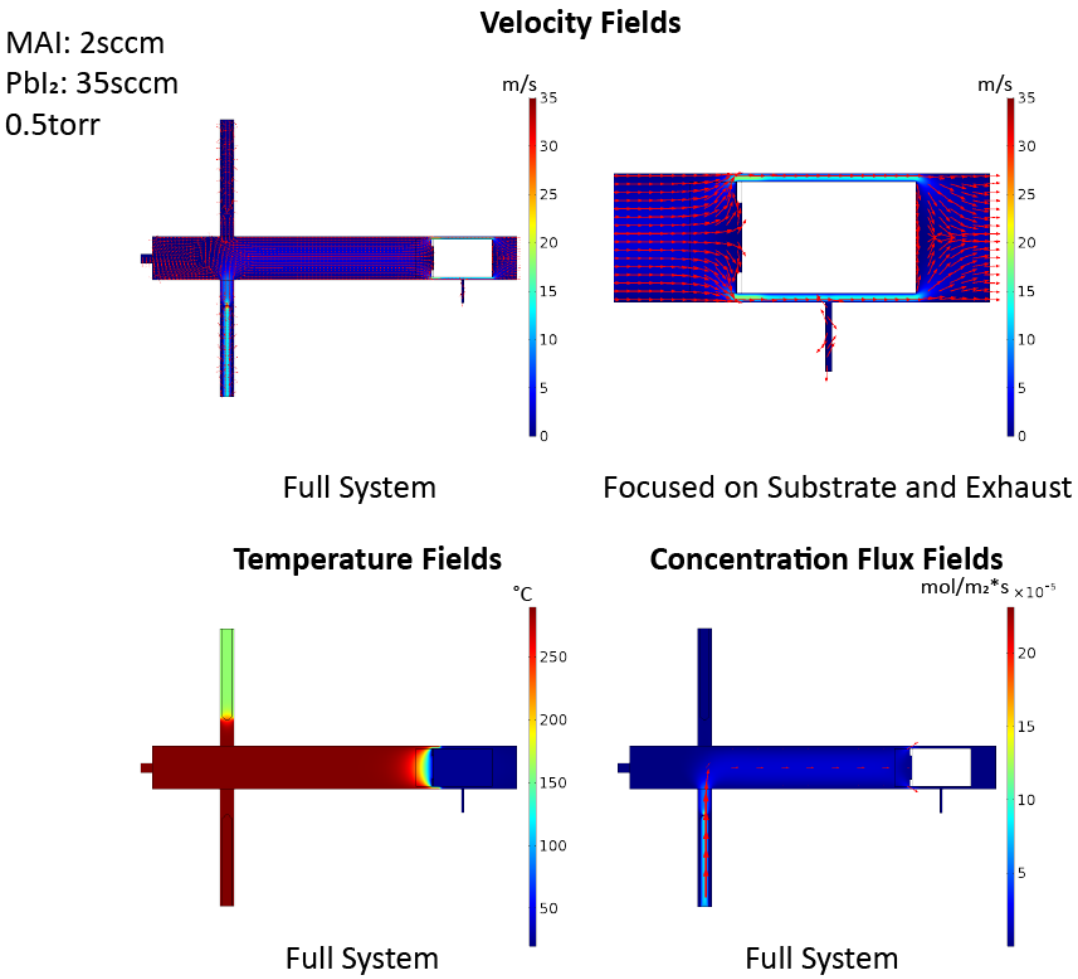

Figure 48. Simulation results for one specific deposition condition. A focus on velocity fields, temperature fields, and concentration flux fields.

In Figure 48, we assume a deposition pressure of 0.5torr with carrier gases for MAI at 2sccm and PbI_2 at 35sccm. As designed, even at the maximum of our laminar flow regime within the chamber, the carrier gases for both precursors are directed towards the substrate. The substrate itself poses a bottleneck for both exhaust ports that will set up a strong boundary layer at the surface of the substrate for deposition. Additionally, the side exhaust port for during loading/unloading of the substrate is successfully placed far enough behind the substrate boundary layer to not affect the deposition on the substrate's surface.

The temperature distribution within the system in this simplified design has a lower temperature at the MAI arm and at the substrate holder. Combining both the carrier gas velocity fields and the temperature distribution, the concentration flux around the deposition chamber is simulated in Figure 48.D. Given the gas profiles and uniform temperatures, the precursor flux is successfully aimed at the substrate. However, in this larger view of the whole deposition chamber at one set of deposition parameters, it is unclear how the precursor flux will initially combine and mix. Figure 49 focuses on the intermixing of the two precursors at a series of deposition parameters.

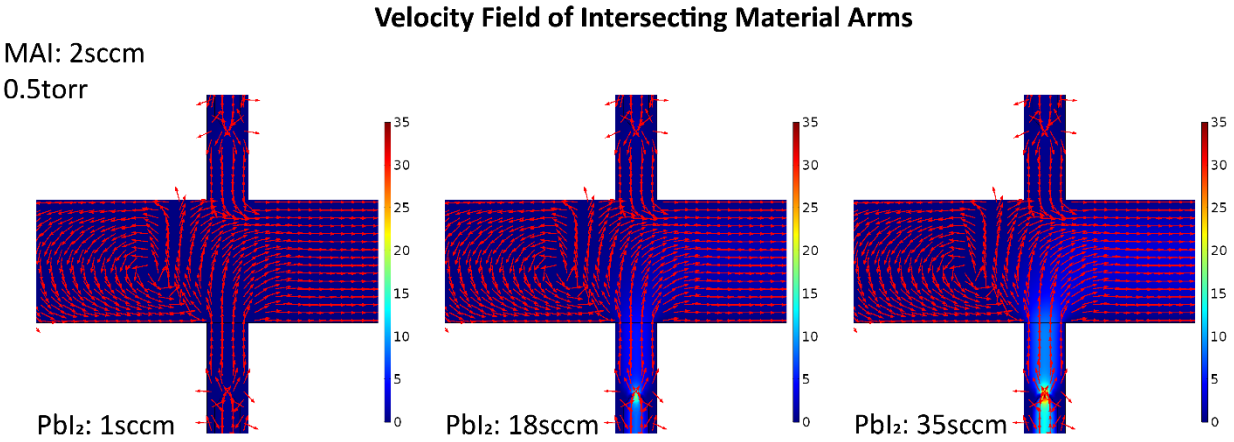

Figure 49. Simulation of the velocity fields with different PbI_2 carrier gas flow rates.

One potential area of high parasitic deposition and important intermixing of precursors is at the intersection of the two material arms. The PbI_2 is deposited at a much higher carrier gas flow rate (due to lower diffusion coefficient) and at a much higher temperature, therefore it may parasitically deposit on the MAI arm due to its lower temperature. In this simulation though, the potential for parasitic deposition appears to be low since from the ending of the quartz component the stainless-steel chamber is heated to the deposition chamber temperature. Therefore, at the intersection there is no cold spot that would attract the PbI_2. Additionally, according to the simulation the intermixing of the two

precursors occurs rather rapidly, with plenty of room left before the substrate boundary layer.

With these understandings of the precursors before interactions with the substrate, the last item to look at is how the film growth is impacted by different deposition parameters (Figure 50).

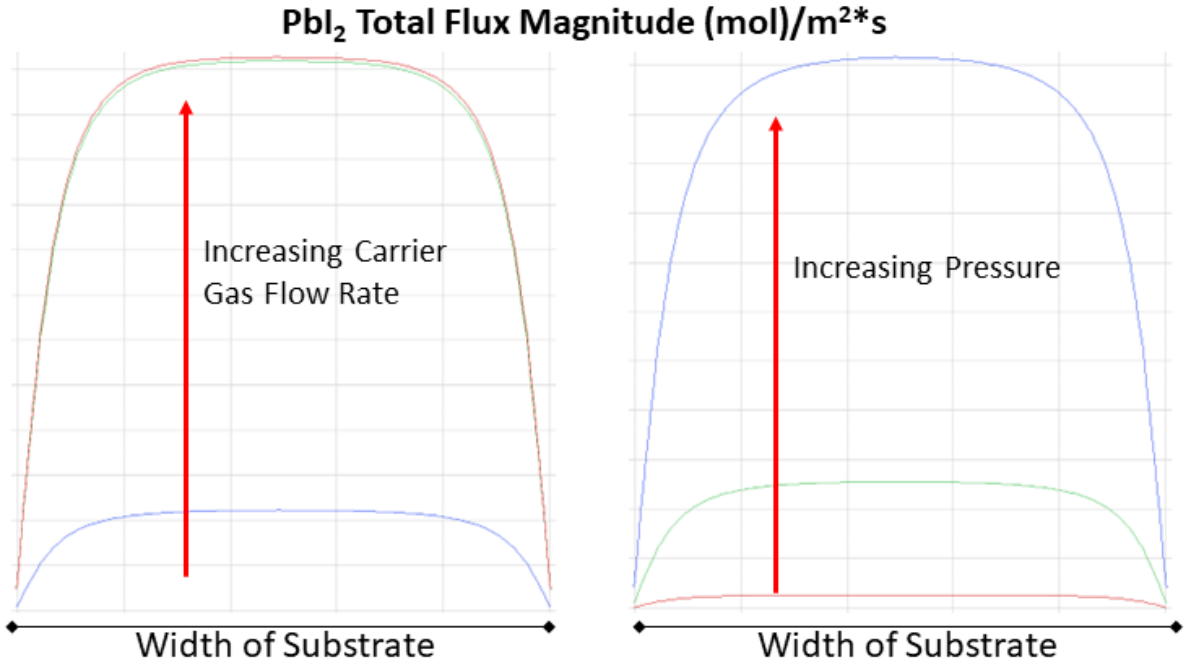

Figure 50. Uniformity and flux magnitude under different deposition conditions, specifically, increasing carrier gas flow rate and increasing pressure.

Across a wide range of deposition parameters available, the precursor flux on the substrate surface is uniform. Only PbI_2 is graphed since it forms the base layer for the perovskite. While it helps to understand how important deposition parameters such as carrier gas flow rate and deposition pressure influence the flux upon the substrate, it is not the only characteristic determining strong film growth. Under these different deposition parameters the films will change from rough to smooth or start to form degradation products. Therefore, both the film growth rate and how these deposition

parameters influence the types of film produced will be recorded. However, these results show that there is a large range of deposition parameters available to optimize film deposition.

4.10 Conclusion

With careful design this system is able to achieve a wide range of independent deposition conditions including:

- Independent material arm temperatures from 295-723K
- Deposition zone temperatures ranging from 295-723K
- Carrier gas flow rates from 0-35sccm
- Substrate temperatures from 35-60°C
- Pressures from 0.05-5torr

Through manipulation of these different deposition conditions, we can probe the influence on perovskite film formation and optimize growth specifically for solar applications.

5. Vapor Co-Deposition of Perovskite Films and Initial Integration into Solar Cells

5.1 Background

Recent literature has seen vapor-deposited perovskites expand in both the number of precursors[28,152] and the techniques available[148,153,154]. While hybrid and sequential deposition processes are an active area of research[148], co-deposition especially within the thermal evaporation field has increased in popularity[155–158]. From there, carrier gas-based deposition techniques have begun to explore co-deposition[51,122,159,160]. With the increase in deposition types available, many researchers have begun to explore vapor-deposition on a larger scale[29,161–163].

Both increases in types of deposition techniques available and in deposition scale is brought about by advances in the fundamental understanding of how to control perovskite precursors under vacuum[164,165]. Deposition parameters such as pressure and substrate temperature are found to control grain size[51], composition[157,158], defect density[166], and crystallinity[167]. With these advances, the vapor-deposition field is starting to define deposition regimes[147] and overall film growth processes[168].

Here, we assess precursor deposition, determine the importance of process parameters, and deposit the very first solar cells with the new VTD system to complete the initial assessment of each step in the fundamental understanding and optimization process. First, we start by assessing deposition of the individual precursors with taking a special eye towards the deposition parameters that influence deposition rate and film morphology. Taking those learnings, we start the co-deposition process and build it

towards incorporation into a device structure. Finally, we deposit initial solar cell devices and discuss how to improve performance.

It is important to realize that the research process is inherently cyclical and folds back on itself at every point in the process to multiple previous steps. The optimization process is never truly done and consequently the research process goes on.

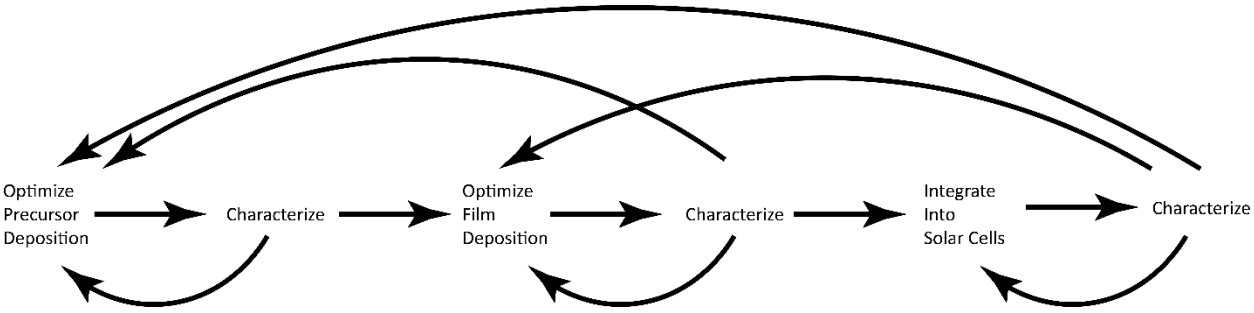

Figure 51. Diagram of the cyclical research process.

The goal of this chapter is to lay the foundation for this cyclical process by defining the base at each step. Then from here, future researchers can go on to continue to optimize and demonstrate remarkable solar cell performance.

5.2 Individual Precursor Deposition

$MAPbI_3$ perovskite is a relatively simple system compared to triple cation or 2D/3D architectures found in literature. However, it also captures the breadth of precursors available to use, and therefore challenges not only equipment design but also material handling. Each precursor has its own unique set of challenges and its own unique role in the deposition process. Furthermore, these roles are more similar to other precursors not found in the current formulation, such as MAI has many similarities to formamidinium iodide (FAI) but less in common with PbI_2. Therefore, understanding the unique challenges

and roles associated with each precursor is a necessary prerequisite to co-deposition of both.

5.2.a Methylammonium Iodide

MAI is notoriously difficult to control under vacuum. Historically, precursors under vacuum are controlled via a quartz crystal monitor (QCM). However, MAI has largely been resistant towards developing a simple QCM rate. Therefore, in literature there are two prevalent techniques for depositing the MAI precursor. One advocates for the use of the MAI partial pressure during deposition since it is the most reproducible[44,169,170]. The other argues that with proper calibration and understanding that quartz crystal monitors (QCMs) provide the more accurate assessment[49]. One potential explanation is the prevalence of organic contaminants in the raw precursor powders. In Chapter 3, we demonstrated that Lumtec precursor powders likely contain organic impurities and are favored by the QCM side of the debate while Sigma-Alrich/GreatCell powders likely do not. Rob *et. al.* discussed how organic contaminants improve the sticking coefficient and likelihood that MAI stays together during vacuum deposition[171]. Additionally, Kim *et. al.* developed an understanding of the MAI sticking coefficients as a function of the species present during a co-deposition process with PbI_2[45]. In general, these discussions surrounding basic MAI control under vacuum highlight the transport and film growth processes that still need to be understood.

As a result of these depositional difficulties, many different techniques have been developed to deposit MAI for perovskite films under vacuum. While researchers using thermal evaporation debate using a QCM vs chamber pressure, others focus on developing other methods. Some separate the precursors into a sequential deposition process, usually referred to as a hybrid technique. Either half of the hybrid technique can be vapor- and/or solution-processed. Similar to previous organic solar cells, Sahli *et. al.*

developed the showerhead deposition method to convert a PbI_2 film to $MAPbI_3$[149]. Meanwhile, Moser *et. al.* used a bidirectional carrier gas flow to grow perovskite films and found that controlling temperature conditions within the reactor was key to proper perovskite conversion[172]. In our new co-deposition system, one of the goals is to study the MAI precursor and understand how to control it in our specific deposition process.

To begin, we first investigate the thickness and morphology dependence of MAI films using a variety of sublimation temperatures and carrier gas flow rates. As fully explained in Chapter 3, using a sublimation temperature as high as 170°C would cause partial MAI degradation including decomposition products in the final film. Therefore, the sublimation temperature is varied from 135°C to 155°C to minimize degradation. The results are shown in Figure 52.

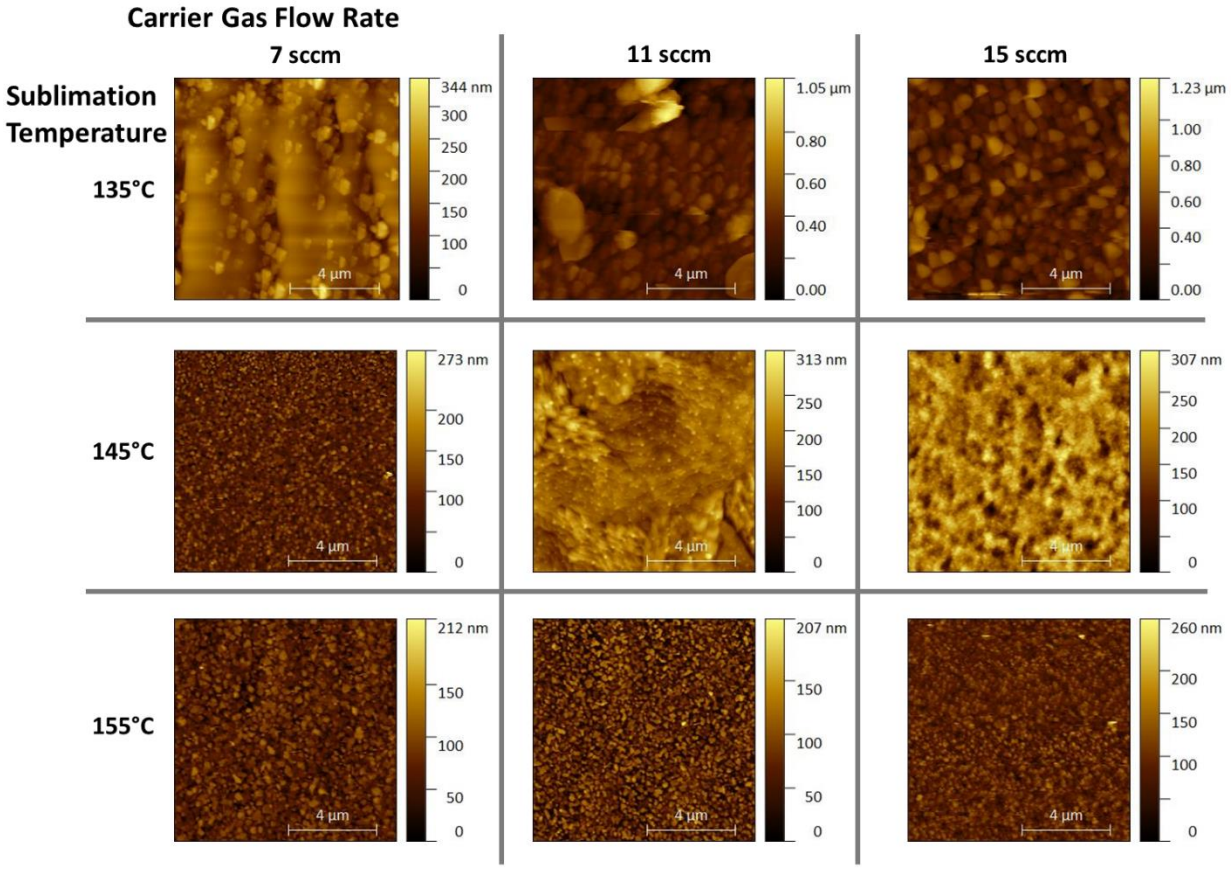

Figure 52. Atomic force microscopy of MAI films deposited under different sublimation temperatures and carrier gas flow rates. While all films exhibit roughness, some conditions maximize islanding film growth.

Measured via AFM, there is a wide range of morphologies present within these deposition parameters. The grain structure changes dramatically with both sublimation temperature and carrier gas flow rate even with the same deposition pressure. The grain size does not appear to trend with neither sublimation temperature nor carrier gas flow rate, however the same cannot be said for the film roughness. This wide range of morphologies additionally necessitates using different ranges for each image's Z axis, across all images the maximum z value ranges from 207nm to 1.23um. Even with a 0 – 207nm Z axis range (found in 155°C, 7sccm) the variation in thickness across the film is likely showing islanding-style growth. To further investigate, cross-sectional images were taken across the 135°C condition using different carrier gas flow rates.

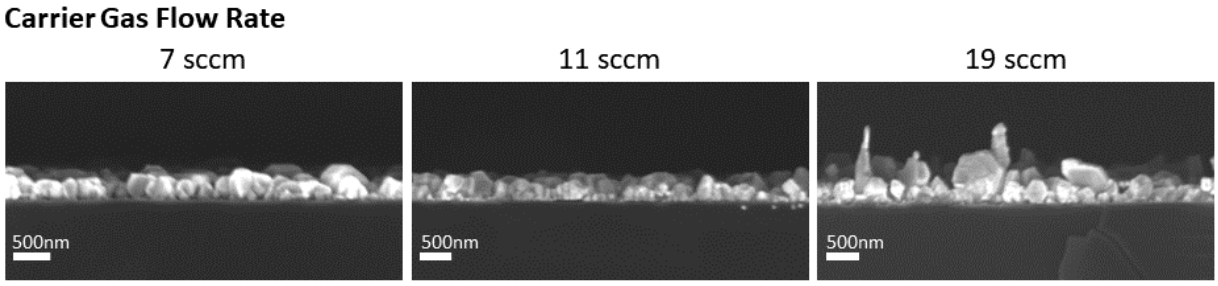

Figure 53. SEM cross-sectional images with 135°C sublimation temperature across three different carrier gas flow rates. The islanding style film growth is present within each film, however, an increase in film roughness is exhibited with higher carrier gas flow rates.

The cross-sectional SEM confirms an islanding film growth structure with "grain boundaries" going all the way to the substrate. In addition, there seems to be an increase in the height of these structures with an increase in carrier gas flow rate even with keeping all other deposition parameters (including pressure) the same. It is important to note, this islanded-style film structure may not be important to the final perovskite film morphology. It is more likely a result of the poor sticking coefficient of MAI to silicon and it's preferential growth on PbI_2 or $MAPbI_3$[168] . However, this film characterization is still of critical importance because it gives a starting point for co-deposition of the perovskite film. Therefore, the full range of MAI films was deposited and characterized for thickness via cross-sectional SEM and roughness via AFM.

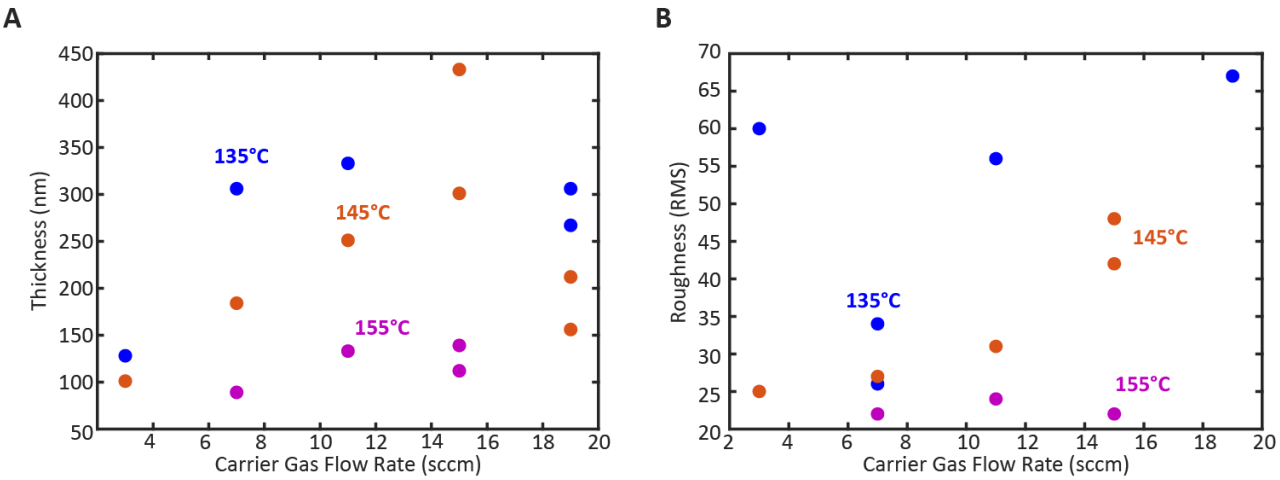

Figure 54. Film thickness and roughness as a result of varying the sublimation temperature and carrier gas flow rate. A. MAI film mildly increasing with an increase in the carrier gas flow rate while decreasing with an increase in the sublimation temperature. B. MAI film roughness increasing as a result of carrier gas flow rate. An increase in the sublimation temperature causes an overall decrease in the film roughness, potentially due to the thinness of the higher sublimation temperature film.

Interestingly, in Figure 54 there is a trend downwards in thickness with all carrier gas rates depending on the MAI sublimation temperature. With an increase in sublimation temperature there is a downward trend in film thicknesses, even with substrate temperature kept constant. This could be indicative of an increase in degradation even with a 20°C change in sublimation temperature. As the MAI precursor material degrades, as shown in Chapter 3, it preferentially forms gaseous byproducts such as methylamine gas. Therefore, this would not deposit on the substrate and cause a thinner film. However, within each of these sublimation temperatures there is a mild trend similar to the equilibrium/kinetic regime theory used in organic vapor phase deposition[173]. There, an increase in the carrier gas flow rate causes an increase in deposition rate only to a certain extent. After a certain carrier gas flow rate, the deposition rate is determined by the sublimation rate which for MAI can be difficult to determine, as mentioned earlier. Based on this graph, the lowest sublimation temperature should be used with a carrier gas flow rate below about 11sccm in order to get both the highest deposition rate possible and control via the carrier gas.

Then, in Figure 54.B, we track the MAI film roughness depending on sublimation temperature and carrier gas flow rate. Once again, we see a general trend downwards with sublimation temperature and upwards with carrier gas flow rate for the 135°C and 145°C curves. Based on both the graphs presented in Figure 54, the 155°C sublimation temperature seems to indicate an upper, deposition parameter limit.

In conclusion, for use in our co-deposition process, it will be important to remember that the MAI deposition rate will be inversely proportional to sublimation temperature and limited in the carrier gas influence.

5.2.b Lead Iodide

Current understanding is that PbI_2 forms the first layer on most substrates during a co-deposition process with MAI[45] and is the controlling factor throughout the deposition. Therefore, the goal of studying the PbI_2 precursor alone is to identify a good material base.

Decoupling the deposition process and looking first to sequential deposition methods, various crystallinities and deposition parameters have been cited to be important to the perovskite conversion process. Specifically, to control the film growth, deposition parameters such as deposition rate[174], pressure, and substrate temperature[175] can dictate crystallinity[176] and density of film grains[146,177]. These features then dictate conversion to perovskite once the organic precursor is introduced[178]. Finally, the defects that originate from the PbI_2 can propagate and damage the $MAPbI_3$[179].

Exactly how baseline morphology and crystallinity of the PbI_2 film will influence perovskite performance in our process is debatable, therefore we will focus on depositing a

reproducible base layer with a wide range of deposition parameters such that we can study the influence during co-deposition.

To start, we work on depositing a complete and uniform film of PbI_2 and positively identifying it as such.

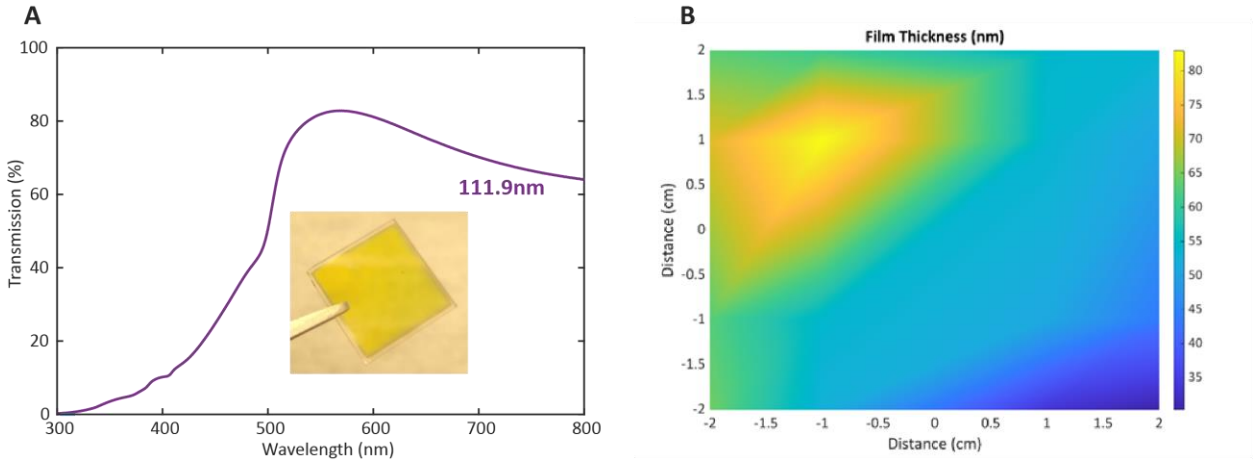

Figure 55. Thickness uniformity and transmission for PbI_2 films in the VTD system. A. UV-Vis transmission spectrum of an example PbI_2 film with a film image inset. B. Ellipsometry of an example PbI_2 film with thickness variations.

PbI_2 should show its absorption onset around 510nm, as confirmed in Figure 55.A. Even though most films by eye show a uniform deposition, some of the films can exhibit large thickness non-uniformities as shown in Figure 55.B. While most of these non-uniformities were addressed with substrate thermal pad engineering shown in Section 4.6.b, non-uniformities can still be present on some of the PbI_2 films.

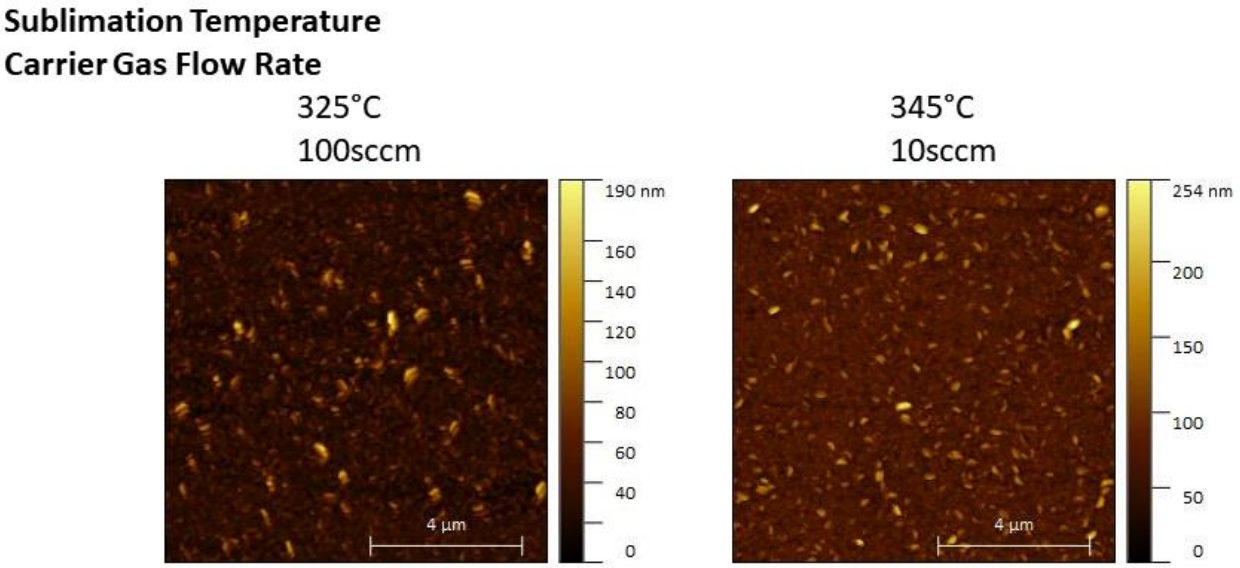

Figure 56. Atomic force microscopy images of PbI_2 at different sublimation temperatures and carrier gas flow rates.

AFM confirms the presence of a complete film absent of obvious pinholes at a variety of deposition parameters. This is enough for now because the conversion process during co-deposition may add an additional smoothing or roughness factor to the film. Therefore, just knowing we can lay down a base layer of PbI_2 that is relatively complete and smooth is enough. Additionally, we know that roughly we can have a sublimation temperature range at least 325°C-345°C with a carrier gas flow rate ranging from 10sccm to 100sccm. Next, we look to the crystallinity of these deposited PbI_2 films.

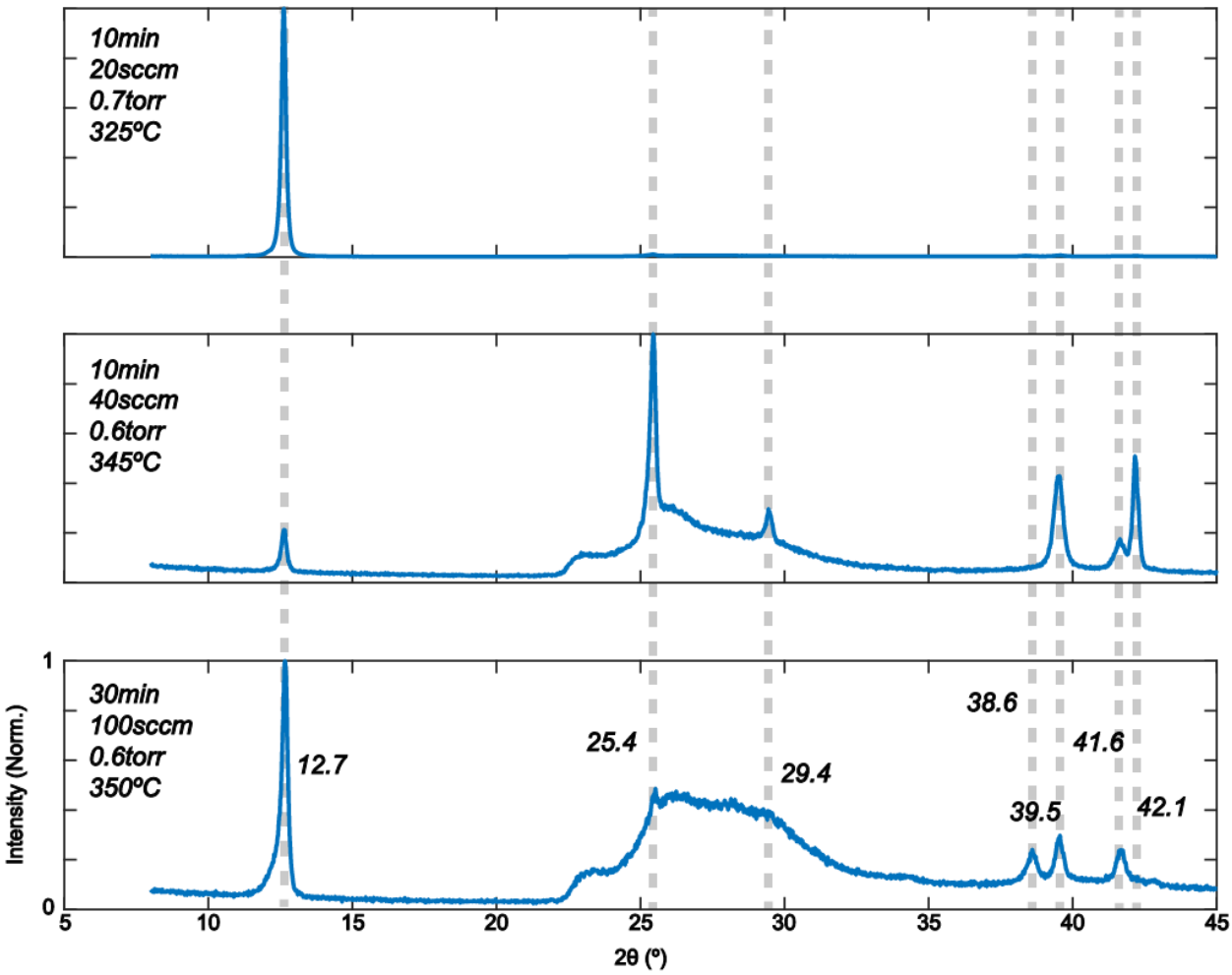

Figure 57. X-ray diffraction patterns of PbI_2 films grown under a variety of different deposition conditions.

Each of the PbI_2 films in Figure 57 is grown with different deposition parameters. Interestingly, not all deposition parameters give the same phases. Each film shows the characteristic peak at 12.7° but to different extents. In Film B the peak at 25.4° dominates compared to the peak at 12.7°. Additionally, at the higher sublimation temperatures and carrier gas flow rates there is an increase in the background noise from around 22° – 33°. It is only Film A that shows only a clear peak at 12.7° and no other features. This might be significant as we move forward. We will have to keep track of the presence of these other, normally less dominant peaks to see how they influence the perovskite film growth under co-deposition. If they are significant and bad, then depositing the PbI_2 layer at slower

carrier gas flow rates and lower sublimation temperatures may give us an overall more fully converted perovskite film.

5.3 Co-Deposited $MAPbI_3$ Films

With control over the individual precursors, we can start to co-deposit full $MAPbI_3$ films. For the VTD system to be useful and in order to optimize film performance, identical deposition parameters need to produce similar films. There are a number of ways to assess reproducibility, either to deposit a whole series of identical films or to repeat conditions after a whole series of experimental films.

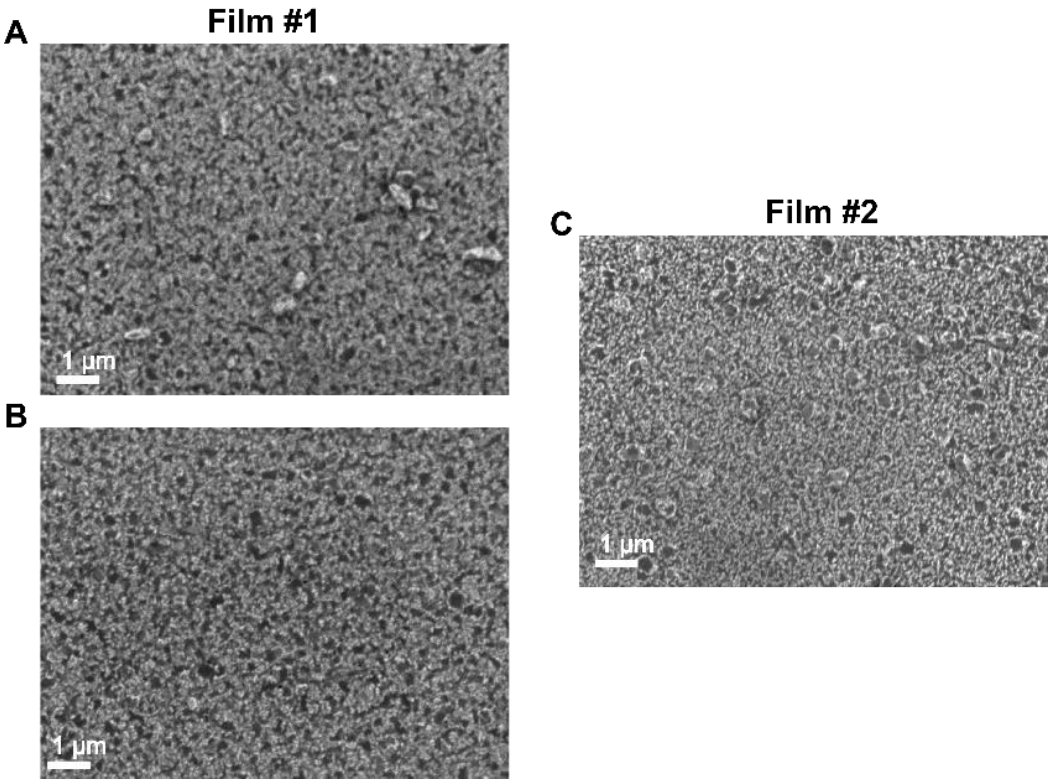

Figure 58. Scanning electron microscopy images of two different films grown under identical deposition conditions. A and B are images over two different areas of the same film while C is a secondary film.

In the first perovskite film, we measure SEM over 2 large areas to compare grain structure. We find a compact and complete grain structure with individual grains much smaller than

the 1µm scale bar. Each portion of the film shown in Figure 58.A and B exhibit similar morphologies which in turn are comparable to another film deposited on a second substrate shown in C. Both the film uniformity across one substrate and across two independently deposited substrates is a positive indication for the reproducibility of future experiments. However, in order to fully understand the structure of the perovskite films we also need to look at the phases present.

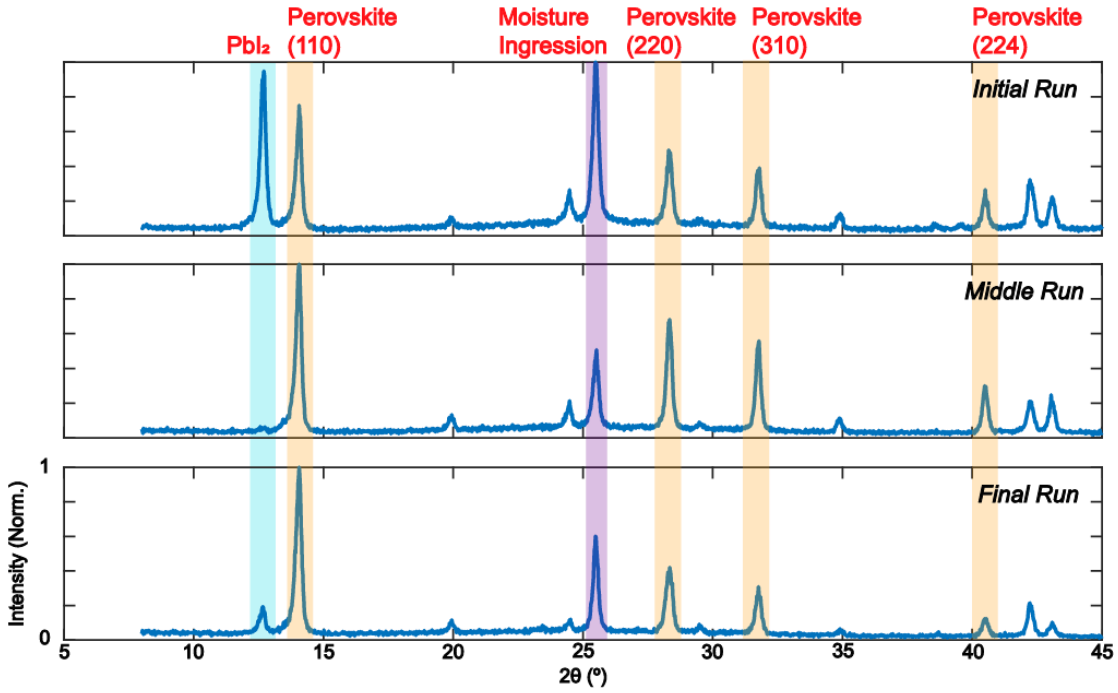

Figure 59. Three films deposited with identical conditions, one right after the other. X-ray diffractions shows the presence of a variety of phases within each film.

Noticeably, there is a changing significance of the PbI_2 peak at 12.7° across the three films. Additionally, each film has the same peaks of perovskite but with varying amounts. For all films the 110 phase is dominant, with the other phases decreasing in intensity from 220, 310, to 224 across all three films. The excess MAI peak is present but only slightly in all three films while the moisture ingression peak is significant.

Consequently, we can routinely deposit perovskite on our substrates, however the precise chemical and crystalline composition may vary slightly with identical conditions. This is something we will need to continue to work on. But for now, we have enough confidence in our system, since the proportions of different perovskite peaks are relatively consistent, to move forward.

5.4 Substrate Influence

Although film growth is dictated by the presence of colder surfaces, quality film growth even under vacuum is determined by deposition conditions and the substrate. As a result, much thought has been placed on determining optimal transport layer substrates for perovskite film growth[180]. The two broad categories of transport layer substrates used in solar cells are organics (such as C60 or PTAA) and inorganics (such as metal oxides SnO_2, TiO_2, and NiOx). Olthof *et al.* investigated perovskite growth on a variety of substrates, finding both the interface formation and work functions depended on the underlying substrate[181]. Building on this chemical-based knowledge, Abzieher *et. al.* developed a framework for crystal growth on different types of substrates, including metal oxides and organics, and finding specifically that different substrates determine vertical grain growth[44].

Organic transport layers have been used to deposited conventional and inverted devices with ease and similar efficiencies[182]. However, even within organic materials, recent research has revealed that differences between even organics cause differences in device performance by modifying the interface and inducing a different morphology[183].

To investigate the influence of film growth in the new VTD deposition system, we use three different substrates, glass, inorganic, and organic films. For an inorganic film, SnO_2 is chosen to be the representative transport layer substrate. SnO_2 has been demonstrated

to be a useful vapor-processed electron transport layer (ETL) for efficient and stable perovskites[184,185].

For an organic option, C60 has been demonstrated to improve metal oxide ETLs via either vapor-processing[186] or solution-processing[187]. Therefore, for the organic film, a thin layer of C60 was used to modify a SnO_2 film. This was done partially because of the success of C60 modifying SnO_2 surfaces for perovskite film growth[187–189], but also so that the substrates were quite similar for the comparison, only differing by a thin organic layer.

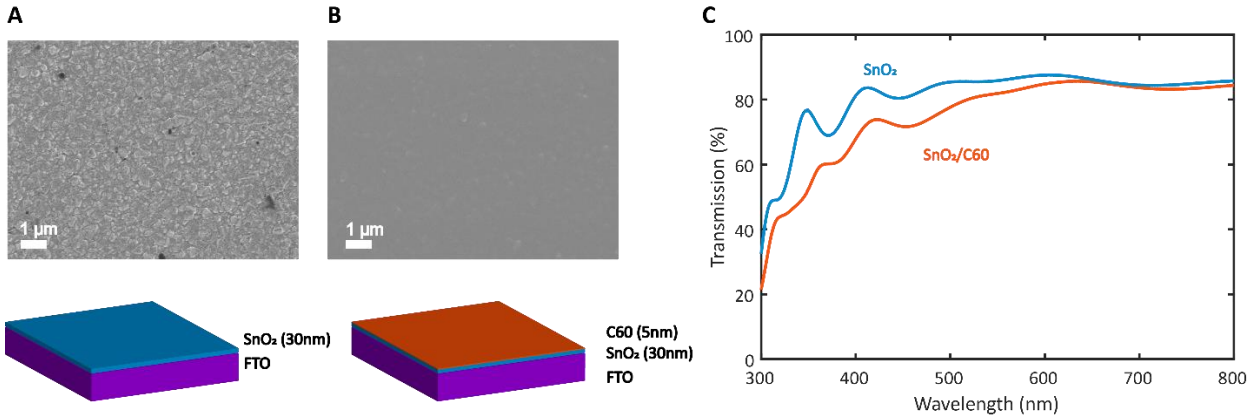

Figure 60. SnO_2 and SnO_2/C60 films to be used for perovskite deposition. A. The configuration and resulting surface scanning electron microscopy image of the SnO_2 substrate. B. The configuration and resulting surface scanning electron microscopy image of a SnO_2/C60 substrate. C. UV-Vis spectra of both SnO_2 and SnO_2/C60 substrates.

Both films show a uniform and compact underlying film structure under SEM. The additional organic layer appears to have a smoothing effect. Furthermore, for wavelengths between 500-800nm the films are around 80% transmissive. Therefore, since both films are relatively smooth with minimal absorption, both could be used as a trial ETL in our devices.

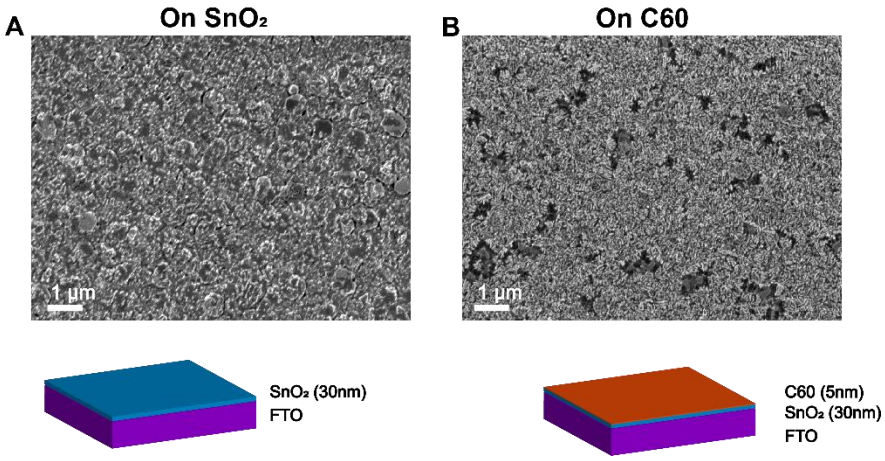

Figure 61. Perovskite film growth on both SnO_2 and SnO_2/C60 substrates. A. $MAPbI_3$ films grown on a SnO_2 substrate. Compact and complete but small grains are shown over the entire substrate. B. $MAPbI_3$ films grown on a SnO_2/C60 substrate. In contrast to the SnO_2 substrate, these films are flaky and exhibit large voids that may or may not go down to the substrate.

Its only when we deposit perovskite films on the different substrates do the differences start to appear. The C60 substrate shows a feathery, platelet style growth which is incompatible with traditional planar perovskite structures. In contrast, the perovskite film on SnO_2 shows a surface morphology similar to films deposited on glass but with larger, more well-defined grains. Similarly, when we look to absorption profiles we see that the films grown on SnO_2 perform the best.

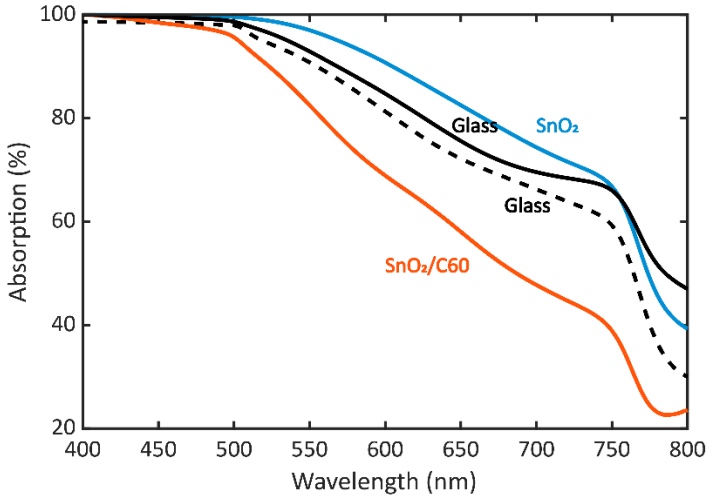

Figure 62. UV-Vis spectra of MAPbI3 perovskites growth on glass, SnO_2, and SnO_2/C60 substrates. All exhibit $MAPbI_3$ absorption onset a little below 800nm and no PbI_2 absorption peak around 510nm.

All 3 substrate types show the onset of perovskite absorption and no clear indication of overly PbI_2 rich films. The two glass spectra are from two different substrates but deposited with the same deposition parameters as the other substrates. It is promising that they show very similar absorption profiles and give us confidence in our different substrate results. The SnO_2/C60 substrate shows the lowest absorption which is surprising, since an integrating sphere was not used in the measurement. Without an integrating sphere, the scattered light appears as absorbed light in the measurement overall the absorbed light is overestimated. However, due to either unfavorable film formation conditions on this substrate or another mechanism, the SnO_2/C60 substrate shows the least absorption.

Due to the poor grain structure and low absorption with similar deposition parameters, the SnO_2/C60 transport layer was not pursued further and instead we focused solely on the SnO_2 transport layer.

5.5 Post-Deposition Film Treatments

One of the key "tricks" to getting the highest efficiency and stability for perovskite devices is through a plethora of post-deposition treatments. While annealing is nearly universal for most solution-processed perovskites, vapor-processed perovskites mainly focus on other post-deposition treatments. For example, post-deposition solvent treatments can either use solvents to deliver a surface-modifying molecule or modify the surface themselves[190,191]. In contrast vapor post-deposition treatments frequently are using the gas to treat the surface and the bulk of the perovskite. Methylamine gas, for example, has been found to partially redissolve the perovskite crystal and heal defects within both the bulk and at the surface[192,193].

A post-deposition treatment that is rather unique to vapor-processed perovskites is an IPA wash after deposition. Other than improving conversion to perovskite, post-deposition treatments in the vapor field are concerned with improving stability through removing MAI and MAI degradation products. One reason why this is a common problem is because MAI has an extremely high diffusion coefficient and will stick around a chamber between depositions. Additionally, MAI will preferentially stick to perovskite over PbI_2 and therefore there is commonly a thin layer of MAI on top of perovskite films acting as a starting point for moisture ingression[133].

To study the potential stability improvements, we deposited two identical films and cleaved them into quarters, knowing that likely the precursor ratios in the films varied only slightly, and exposed both to 50%RH after post-deposition treatments, specifically to target the potential moisture ingression.

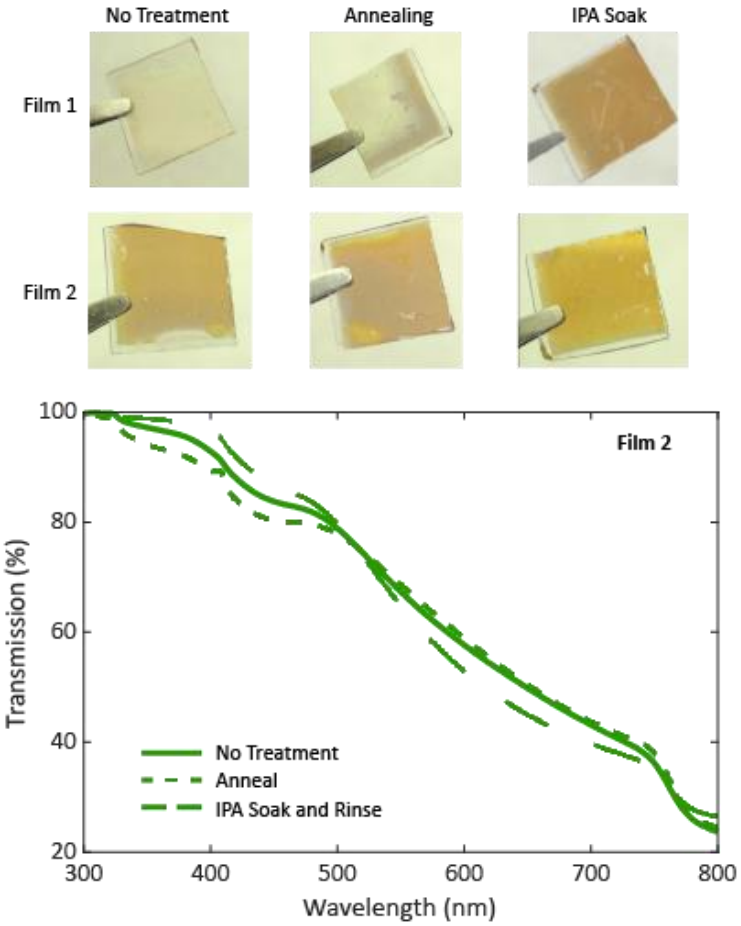

Figure 63. IPA treatments to improve the short-term film stability of $MAPbI_3$ perovskite films deposited on glass under identical deposition conditions.

As shown in Figure 63, even with identical deposition parameters one of the films turned white upon exposure to 50%RH. Only the IPA rinse post-deposition treatment prevented the film from turning white, annealing did not prevent moisture ingression.

The ineffectiveness of annealing in this instance calls into question why researchers use annealing in the first place. In the solution-processing field the solvents drive the perovskite formation process[194]. Therefore, annealing the films can influence crystallization and remaining solvents left in the film. In vapor-processing the annealing influence is trickier, given there is no solvent during the deposition process. It is known that the substrate temperature will influence perovskite formation during deposition.

Temperatures lower than room temperature will inhibit perovskite formation[112] while temperature above 110°C will cause MAI to leave the substrate surface. If precursors are balanced it has been hypothesized that post-deposition annealing is not required for co-deposited perovskites[195], however it has proven useful in determining final perovskite phase[196]. Therefore, while in this case it was not useful for preventing moisture ingression, it could still be a tool for fine tuning film crystallinity.

Meanwhile, the other film stayed brown no matter whether it had a post-deposition treatment or not. Since both films were deposited using the same conditions this points to inconsistencies in the film growth process that can be significant to short-term film stability.

To further investigate the post-deposition treatment on the absorption profile of each film, we took the films to UV-Vis. Each post-deposition treatment does not vary the absorption profile significantly from the baseline, untreated film. Either these treatments do not influence the film in a way discernable via UV-Vis or these films were already optimized in such a way that the post-deposition treatments no longer had any influence.

Further investigations into the influence of IPA post-deposition treatments reveals a dramatic influence for certain perovskite films.

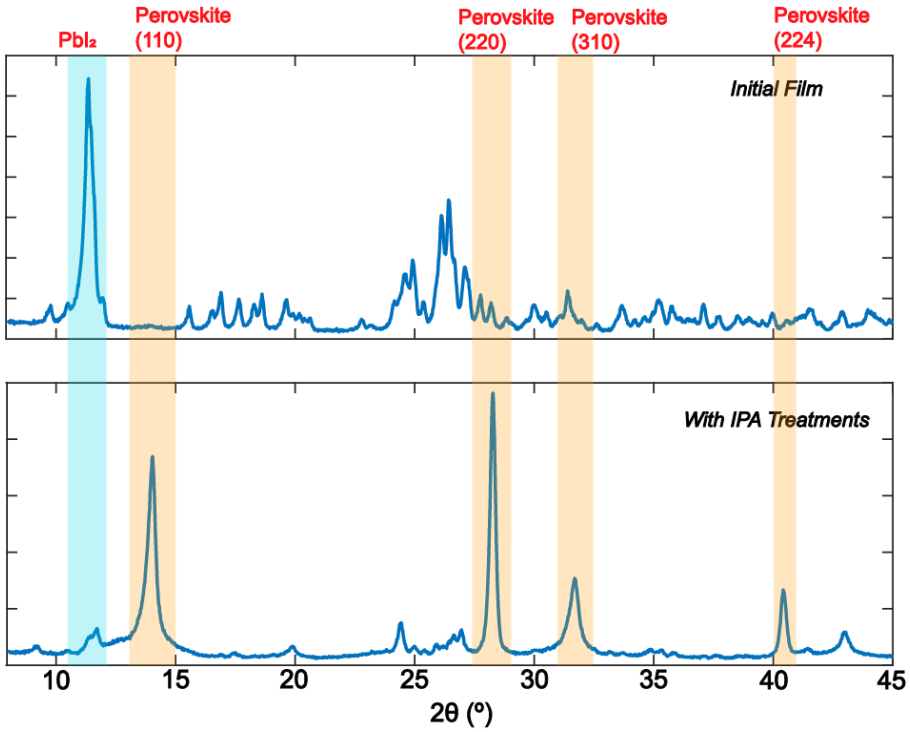

Figure 64. X-ray diffraction patterns before and after IPA treatments.

In Figure 64, the initial, pre-IPA rinse film shows no perovskite peaks. Rather, it shows an intense PbI_2 peak and fuzziness oftentimes related to MAI excess. Then after an IPA treatment, the film no longer exhibits the intense PbI_2 peak and rather shows the perovskite phases 110, 220, 310, and 224. Therefore, the IPA treatment turned the unreacted precursors in the film to perovskite!

XRD measures the entire film so although we know that there is both MAI and PbI_2 in the film, we do not know the relative locations of each material even though it has been co-deposited. Potentially, even with the low formation energy to perovskite under vacuum, IPA mediates MAI diffusion to PbI_2 locations or conversion to perovskite.

5.6 Initial Solar Cells

Although these perovskite films need further investigation into deposition parameters and undergo a resulting optimization, we integrate the films into solar cells as they are as an initial assessment. The device architecture used is FTO/SnO_2/perovskite/Spiro-OMeTAD/Au as it is a common and reproducible option.

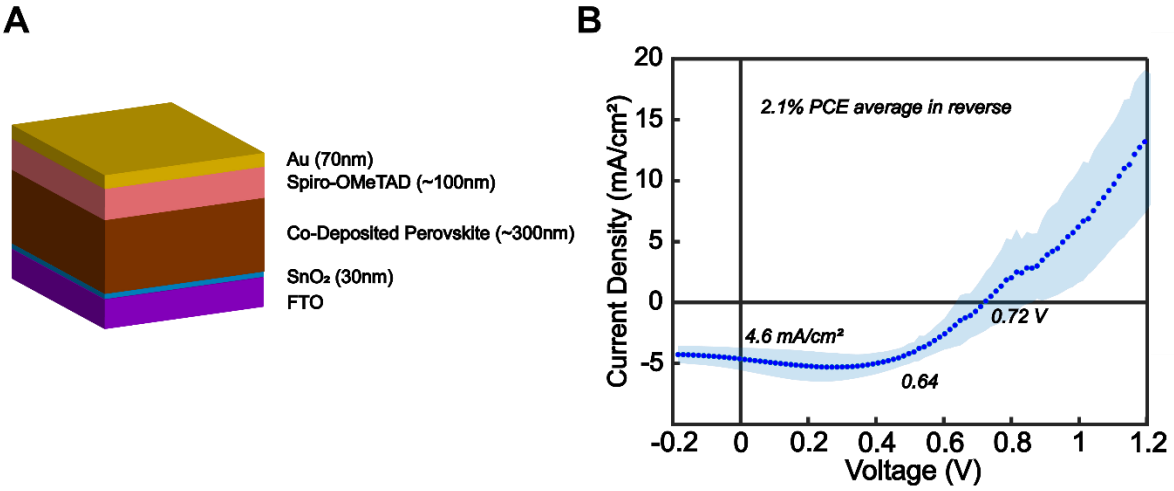

Figure 65. Initial integration of co-deposited VTD perovskite films into solar cells. A. Device architecture used in this work. B. JV curves averaged over ~10 solar cells.

Integrated into solar cells, the initial co-deposited perovskite films give an average of 2.1% power conversion efficiency. In some of these solar cells, there is the presence of an energy barrier at voltages above V_{OC} and an increase in current around 0.3V with the current dropping again around J_{SC}. There could be multiple processes going on that inhibit the free motion of carriers through the device stack. Interfaces are frequently points of energy barrier formation. If we split one JV curve into forward and reverse scans we may see more about the movement of charges or energy barriers within the device.

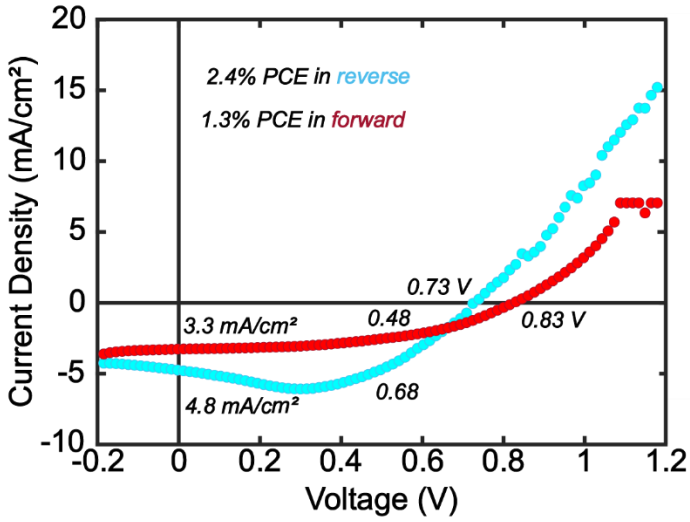

Figure 66. Decoupling averaged JV curves by analyzing the forward/reverse scans and highlighting all the different parameters.

When we do forward and reverse scans on a singular device, we see significant hysteresis. Hysteresis is due to the movement of ions within the device that are influenced by interface morphology[197] and device architecture. It is likely that ionic motion within the device is also the cause of current decreases around J_{SC}. A small voltage across the device could be breaking down an energy barrier that is preventing effective charge flow. It is also notable that the V_{OC} shifts if in forward or reverse scanning. That means that the built-in electric field of the device or the bandgap of the material is shifting with JV scans. We know from previous XRD measurements that there is a large portion of unreacted precursors (both PbI_2 and MAI) present in some films. These unreacted precursors could be influencing interfaces and bulk perovskite structure as they potentially migrate due to the voltages during JV testing causing carrier recombination. It seems that the best path forward for better device performance is improving films via controlling the conversion to perovskite. Specifically in this case, to convert all the precursors within the film.

5.7 Conclusion

Now that we have seen VTD perovskite films under a variety of situations, we can start to summarize common features across conditions. The morphology of the films on glass and SnO_2 is quite similar and devoid of the large grains frequently targeted in high performing solar cells. Rather, the structure is granular and hard to distinguish stereotypical perovskite grains. This could indicate a need to study perovskite film growth under these conditions and on more optimal substrates such that large grain boundaries form.

This unusual film morphology translates into interesting features within the crystalline structure. While we frequently see perovskite peaks in the 110, 220, 310, and 224 phases, we also see a large quantity of unreacted precursor peaks. The unreacted precursors in the film could be at separate film locations or require a perovskite formation energy greater than what is provided during VTD. However, the presence of these unreacted precursors could be one of the root causes of hysteresis and low solar cell performance.

Moving forward, now that we have tracked film progression at all stages of the optimization process, there are clear paths forward for improvements.

Conclusion

Summary of Key Findings

This thesis focuses on work done to develop a vapor transport deposition system and to start understanding the co-deposition process within it. Initial work focused on developing a VTD system with the widest range of decoupled deposition parameters available, such that the full promise of VTD could be studied. With a focus on co-deposition, it was also necessary to also explore MAI's compatibility to be co-deposited with higher temperature metal halide precursors. We found that MAI sublimation temperatures were most influential to instigating film degradation for deposition chamber temperatures below 350°C. Above 350°C, the MAI would also start to degrade as a result of transport through the deposition chamber.

Concentrating on co-depositing MAI and PbI_2 to form $MAPbI_3$ perovskite, we laid the groundwork for future perovskite film optimization by assessing film absorption, structure, and morphology. We evaluated the reproducibility of film deposition and found that the presence of unreacted precursors is greatly dependent on deposition parameters. Additional work started to consider film growth on different substrates and paved the way for initial integration into solar cells.

Future Directions

From here, there are two potential paths forward. One focuses on the fundamental understanding of the co-deposition process. The other focuses on this technique as a potential manufacturing method. The manufacturing path would fixate on deposition speed and would potentially lead towards relying heavily on post-deposition treatments to ensure high quality perovskite. In contrast, concentrating on the fundamental understanding of the co-deposition process would disregard the deposition speed in favor of explaining material transport processes within the chamber, film nucleation and growth, and/or control over organic precursor degradation. There is value and use in both research focus strategies. The need for higher efficiency and easily deposited solar cells dictates an urgency to renewable energy research that produces consumer products. However, taking the time to understand the basics of VTD and publishing for the world to see would assist in many different deposition techniques beyond VTD. Therefore, that is what this thesis focuses on while attempting to remain relevant to commercialization. By continuing to merge both the fundamental and the practical, renewable energy research as a whole can continue to re-imagine the energy consumption of the world.

Materials and Methods

Perovskite Film and Solar Cell Fabrication

Substrate Cleaning

Substrates were cleaned either by:

1. Sonication in acetone (Sigma-Aldrich) followed by sonication in IPA (Sigma-Aldrich), each for 10min. After each sonication the substrates are blown dry using nitrogen.
2. Scrubbing each substrate with detergent followed by sonication in acetone (Sigma-Aldrich) for 5min. Then the substrates are boiled in an IPA (Sigma-Aldrich) beaker twice for 5min each. Finally, the substrates are blown dry using nitrogen.

Substrates with ITO or FTO were both purchased pre-pattern from TFD.

SnO_2 Deposition

For the SnO_2 electron transport layer, start by dissolving KCl (Sigma-Aldrich) in DI water to make a 3mg/mL solution. Dilute the SnO_2 nanoparticle stock solution (Alfa Aesar, 15% wt% in water) in the KCl/DI to make a 3% (wt/wt) solution. UV/Ozone treat the substrate for 20 minutes before spin coating in air at 3000rpm for 30 seconds. Clean off the electrodes and anneal the films in air at 150°C for at least 30 minutes.

Perovskite Precursors

MAI powders unless noted otherwise were purchased from Luminescence Technology Corporation. The other manufacturers used were Sigma-Aldrich and GreatCell. PbI_2 powders were from either TCI Chemicals or Alfa Aesar. All precursor powders were stored under nitrogen until loaded into the chamber.

C60 Deposition

C60 was purchased from Luminescence Technology Corporation and deposited using a thermal evaporator designed by Victory Engineering.

Spiro-OMeTAD Deposition

Dilute to 520mg/mL lithium bis(triflouromethane) sulfonamide (Li-TFSI) (Sigma-Aldrich) in acetonitrile (Sigma-Aldrich). Take care to protect the solution from light exposure and moisture. Mix a solution of 72 mg Spiro-OMeTAD (Luminescence Technology Corporation), 1000 uL chlorobenzene (Sigma-Aldrich), 17.5 uL Li-TFSI solution, with 28.8 uL tetraphenyl butadiene (tpb) (Sigma-Aldrich). Make sure you add the Li-TFSI to the solution before tpb. Filter the resulting solution through a 0.45 um PTFE solution and spin at 4000rpm in dry air for 30 seconds. Store in dry air overnight before depositing next layer.

Post-Deposition Treatments

IPA Post-Treatments

For the static spinning version of IPA post-deposition treatment: In IPA is dripped all over the substrate and left to sit for 10 seconds. Then the substrate spins at 2000 rpm for another 30 seconds.

For the dynamic spinning version of IPA post-deposition treatment: In dry air IPA is dripped all over the substrate as it spins at 4000 rpm for 30 seconds. The solution is administered after the substrate is spinning at speed and takes less than 5 seconds.

Annealing

The films were annealed in dry air at 100°C for 30min.

Electrode Deposition

The electrodes were deposited in a custom thermal evaporator, starting the deposition at 0.5A/s for the first 20-30nm and then at 1A/s for the rest of the deposition. The final electrode thicknesses range from 70-100nm and are noted in the text.

PbS QD Deposition and Solar Cell Fabrication

Materials were purchased from Sigma Aldrich for all the solvents and ligands, Kurt J. Lesker for all the evaporation materials, and Plasmaterials for all sputtering targets. QDs were fabricated through Hines and Sholes PbS QD hot-injection synthesis method[198].

Pre-patterned 150nm thick ITO was purchased from TFD. ZnO was then deposited through sputtering at 0.5A/s and 20mTorr in a pure argon environment. The PbS QD active layer was built up via layer by layer spin coating in air. First, a 50mg/mL PbS QD (first exitonic peak around 920nm) in octane was deposited at 2500rpm for 15s making around a 20nm thick film. Next, for ligand exchange, the ligand solution covered the QD layer and allowed to sit for 30s before spinning off at 7500rpm for 15s. Finally, the newly ligand exchanged films were washed in the ligand's solvent three times. For TBAI the solution used was 10mg/mL TBAI powder in methanol. For EDT the solution used was 0.02% EDT in acetonitrile. After depositing 10 TBAI layers (~200nm total) and 2 EDT layers (~40nm total) the PbS QD absorbing layer and PbS QD HTL were complete.

NiOx was then deposited through sputtering at 0.1A/s and 6mTorr in a pure argon environment. AlOx was deposited through sputtering at 0.2A/s and 3mTorr in a pure argon environment. The ITO buffer layer was deposited via sputtering at 0.6A/s and

6mTorr in a pure argon environment. Finally, the chromium buffer layer and all metal electrodes were deposited via thermal evaporation at 0.5-1A/s.

Tube Furnace Experiments

A standard quartz tube was used for the tube furnace depositions. The tube furnace was pumped down to 10-2torr and a copper stage for the substrate was set to 15°C. Nitrogen at a 1sccm flow rate (as determined by a mass flow controller) was used for the carrier gas. Around 0.3g of MAI (GreatCell Solar) was loaded in humidity ranging from 5-35% into a quartz boat for deposition. Zone 1 and 2 were allowed to stabilize at temperature before a quartz rod moved the quartz boat into Zone 1. Depositions lasted for around 20 minutes.

Film and Solar Cell Characterization

X-Ray Diffraction (XRD)

X-Ray Diffraction was performed on a Rigaku Smartlab Multipurpose Diffractometer in the MIT Materials Research Laboratory. The settings were PB-PSA GIXD with 0.02 step size and a rate of 0.6s/step.

Fourier Transform – IR (FTIR)

The FTIR-ATR used primarily was a Thermo Fisher Nicolet iS50 Fourier Transform Infrared Spectrometer with diamond-based Attenuated Total Reflection crystal and infrequently with a Bruker FT-IR system at the Harvard Center for Nanoscale Sciences. ATR measurements were used due to the ability to measure multiple characteristics off of the same set of samples with minimal preparation and ATR's usefulness in measuring coatings.

However, current literature is a collection of transmission and absorption curves and ATR measurements are directly output as absorbance. Absorbance is a unit of attenuation (commonly in log scale) which is the direct consequence of interaction with the ATR crystal. If we were to switch to either absorption or transmission then we would need to assume film qualities such as scattering or reflection. Then the conversion between absorbance and transmission, for example, come from the dependence on wavelength and refraction index and are reflected in the peak intensities. For this work, we will stick with using the direct absorbance measurement so we do not need to assume anything about the amount of scattering/reflection in our different samples. This means that our relative peak intensities and exact positions will vary from some literature results.

X-Ray Photoelectron Spectroscopy (XPS)

X-Ray Photoelectron Spectroscopy was performed on a Thermo Scientific K-Alpha+ system at the Harvard Center for Nanoscale Sciences. Fits were found on the Avantage software and graphs were charge corrected via the adventitious carbon line at 248.8eV. Overall composition was found by integrating the area of each element and significant peak values were assigned corresponding to their literature values[199–201]. Each sample had two spots measured.

Scanning Electron Microscope (SEM)

For SEM, the films were measured either with a Zeiss Gemini 450 SEM in MIT.nano or a Zeiss Merlin High-Resolution SEM in MIT Materials Research Laboratory.

Atomic Force Microscope (AFM)

The Atomic Force Microscope used was an Asylum Research Cypher VRS AFM in tapping mode at MIT.nano.

Current Density – Voltage Measurements (JV)

Current-voltage measurements were conducted using a Newport solar simulator and either a custom solar cell holder or one from Mutovis.

Appendix A: Evaporation Theory

Assumptions:

- Can use ideal gas approximation – since most gases trend towards being ideal at low pressures and the sublimed precursor amount is minimal this should be a valid assumption.

Theories Used:

Ideal Gas Law

$$PV = nRT$$

P : pressure (Pa)

V : volume (m^3)

n : amount of gas molecules (mol)

R : gas constant

T : temperature (K)

Hertz-Knudsen

$$\frac{r_{evap}}{A_{eff}} = \alpha \frac{P_{mat}^{sat} - P_{cell}}{\sqrt{2\pi MRT_{mat}}}$$

r_{evap} : evaporation rate (mol/s)

A_{eff} : effective precursor surface area (m^2)

α : sticking coefficient for re-adsorption (unitless)

P_{mat}^{sat} : saturation material pressure (Pa)

P_{cell} : pressure of source cell (Pa)

M : molar mass of precursor (kg/mol)

T_{mat} : material temperature (K)

Langmuir Evaporation vs Effusion

Clausius-Clapeyron

$$P_{eq} = P_o \exp\left(\frac{\Delta H_{vap}}{RT}\left(\frac{1}{T_0} - \frac{1}{T_{mat}}\right)\right)$$

P_{eq} : Partial Pressure (Pa)

P_o : Base pressure (Pa)

ΔH_{vap} : Enthalpy of vaporization

With R and T defined same as above.

Derivation for Evaporation Rate from Precursor Material Inside Source Cell:

The evaporation rate is given by the Hertz-Knudsen Equation:

$$\frac{r_{evap}}{A_{eff}} = \alpha \frac{P_{mat}^{sat} - P_{cell}}{\sqrt{2\pi MRT_{mat}}}$$

Where P_{mat}^{sat} is given by the Clausius-Clapeyron relation:

$$r_{evap} = \alpha A_{eff} \frac{P_o \exp\left(\frac{\Delta H_{vap}}{RT}\left(\frac{1}{T_0} - \frac{1}{T_{mat}}\right)\right) - P_{cell}}{\sqrt{2\pi MRT_{mat}}}$$

Derivation for Output Rate from Source Cell:

We are looking for output rate (given in mol/s)

We know from the Ideal Gas Law:

$$n = \frac{VP}{RT}$$

Since n is mol of material, dividing both sides by time gives a rate:

$$\frac{n}{s} = \frac{VP}{sRT}$$

Additionally, $\frac{V}{s}$ is the volumetric flow rate, for this case, the carrier gas flow rate (different from the flow rate read by MFCs). This leaves only the precursor pressure within the chamber as an unknown. From Hertz-Knudsen and Clausius-Clapeyron we previously solved for the evaporation rate:

$$r_{evap} = \alpha A_{eff} \frac{P_o \exp\left(\frac{\Delta H_{vap}}{RT}\left(\frac{1}{T_0} - \frac{1}{T_{mat}}\right)\right) - P_{cell}}{\sqrt{2\pi M R T_{mat}}}$$

Which should be equivalent to the total output of the source cell and gives us a second equation for the second unknown:

$$r_{out} = \frac{n}{s} = \frac{\bar{V}P}{RT} = r_{evap} = \alpha A_{eff} \frac{P_o \exp\left(\frac{\Delta H_{vap}}{RT}\left(\frac{1}{T_0} - \frac{1}{T_{mat}}\right)\right) - P_{cell}}{\sqrt{2\pi M R T_{mat}}}$$

Where $P_{cell} = P$, from the ideal gas law. Solving for P :

$$P\left(\frac{\bar{V}}{RT} + \frac{\alpha A_{eff}}{\sqrt{2\pi M R T_{mat}}}\right) = \frac{\alpha A_{eff} P_o \exp\left(\frac{\Delta H_{vap}}{RT}\left(\frac{1}{T_0} - \frac{1}{T_{mat}}\right)\right)}{\sqrt{2\pi M R T_{mat}}}$$

And thus:

$$r_{out} = \frac{\bar{V}P}{RT} = \frac{P_o \exp\left(\frac{\Delta H_{vap}}{RT}\left(\frac{1}{T_0} - \frac{1}{T_{mat}}\right)\right)}{\frac{RT}{\bar{V}} + \frac{1}{\alpha A_{eff}}\sqrt{2\pi M R T_{mat}}}$$

Appendix B: VTD Operation and Loading Procedures

Chamber Operation

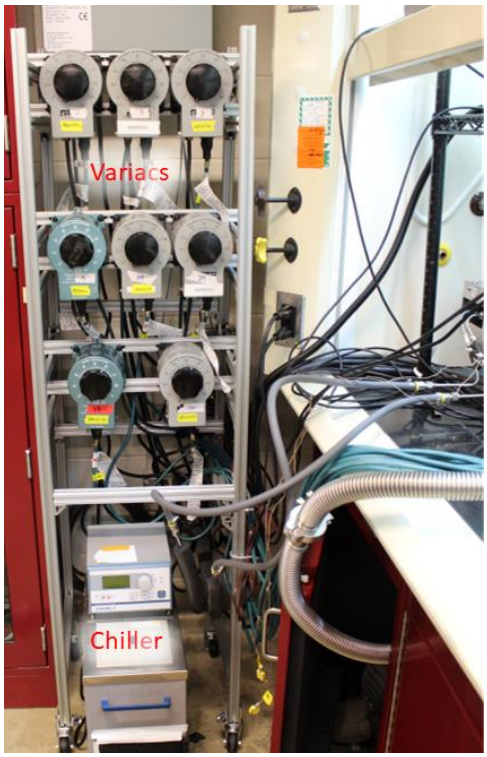

1. Close the gate valve and open the backing line to the deposition chamber
2. Turn on the chiller and the heating element for the substrate translation/rotation stage
3. Wait for the chiller to reach the baseline temperature
4. Start the power controllers, previous ramp powers and deposition powers are recorded in the logbook
5. Wait for the quartz insert internal thermocouples to reach the target value and stabilize for 5min
6. Load the substrate
7. Open the gate valve and close the backing line to the deposition chamber
8. Translate the substrate stage to the deposition zone
9. Turn on the carrier gas

10. Wait for the pressure to stabilize

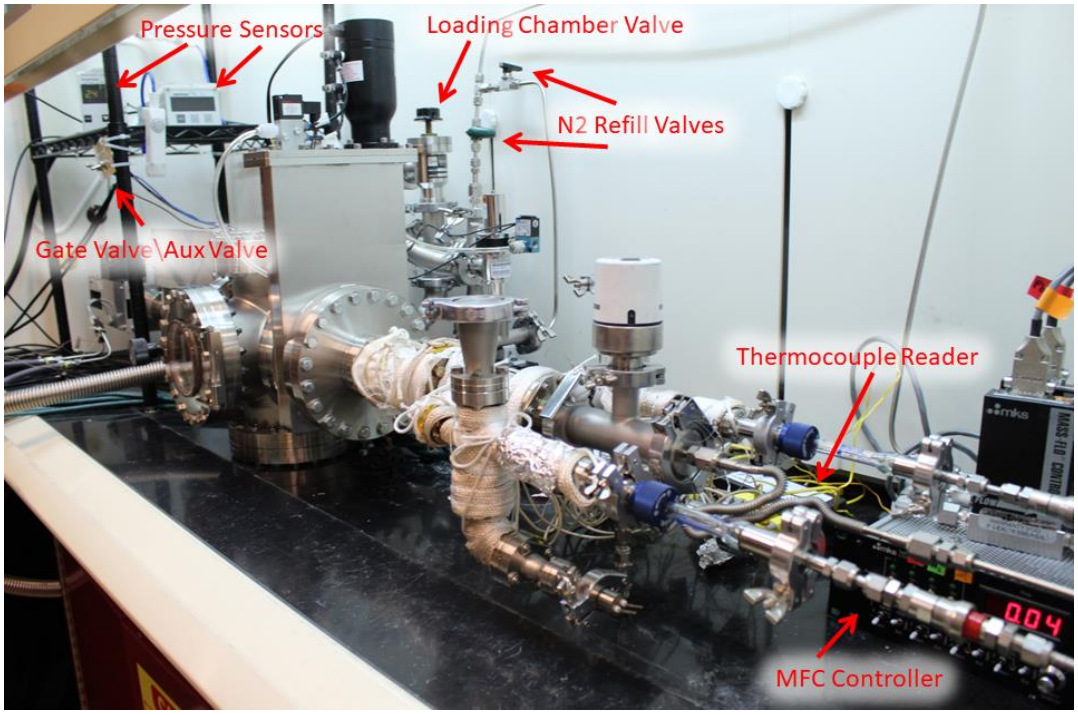

11. Rotate the quartz insert arms to the "on" position. Do the MAI arm first and then the PbI_2 arm. Make sure you do a pure rotation and don't put any other torque on it
12. Deposition
13. Rotate the quartz insert arms (PbI_2 first then MAI) to the "off" position
14. Remove the substrate stage while the carrier gas is still flowing through the "off" position
15. Close the gate valve, open the backing line to the deposition chamber, and quickly turn off the carrier gas
16. Replace the substrate

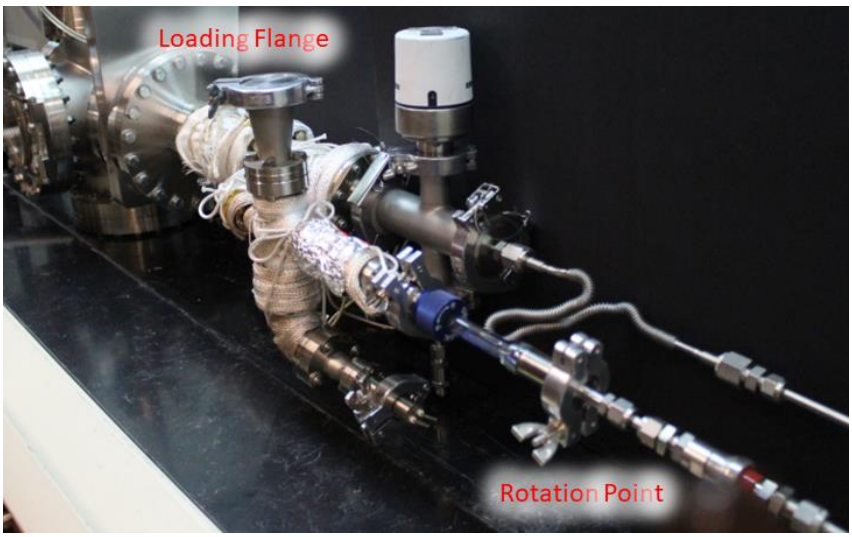

Loading the Chamber

1. Open the gate valve
2. Close the backing line to the loading and to the deposition chamber
3. Open the loading door
4. Vent the full system
5. Loading door will swing open when the chamber is fully vented
6. Lay down aluminum foil around the chamber
7. Unlatch the KF flange from the quartz arm to the MFCs
8. Open the KF blank to the loading zone of the quartz reservoir
9. Loosen the blue, compression flange
10. Pull out the quartz insert nitrogen arm and place on spare aluminum foil
11. Use a long hook to pull out the quartz insert reservoir and load with new material
12. Do 7-11 in reverse order to put the quartz insert back together
13. Close the chamber door
14. Slowly open the backing line to the deposition chamber and keep opening until the valve is fully open
15. Open the backing line to the loading chamber

16. Close the gate valve
17. Clean up after yourself

References

1. Fawzy, S., Osman, A. I., Doran, J. & Rooney, D. W. Strategies for mitigation of climate change: a review. *Environmental Chemistry Letters 2020 18:6* **18**, 2069–2094 (2020).
2. Mi, Z. & Sun, X. Provinces with transitions in industrial structure and energy mix performed best in climate change mitigation in China. doi:10.1038/s43247-021-00258-9.
3. Filho, W. L. *et al.* Realising the Potential of Renewable Energy as a Tool for Energy Security in Small Island Developing States. *Sustainability 2022, Vol. 14, Page 4965* **14**, 4965 (2022).
4. Viviescas, C. *et al.* Contribution of Variable Renewable Energy to increase energy security in Latin America: Complementarity and climate change impacts on wind and solar resources. *Renewable and Sustainable Energy Reviews* **113**, 109232 (2019).
5. Roose, B. *et al.* Local manufacturing of perovskite solar cells, a game-changer for low- and lower-middle income countries? *Energy Environ Sci* (2022).
6. Owusu, P. A. & Asumadu-Sarkodie, S. A review of renewable energy sources, sustainability issues and climate change mitigation. *http://www.editorialmanager.com/cogenteng* **3**, (2016).
7. Jean, J., Brown, P. R., Jaffe, R. L., Buonassisi, T. & Bulović, V. Pathways for solar photovoltaics. *Energy Environ Sci* **8**, 1200–1219 (2015).
8. Bosio, A., Pasini, S. & Romeo, N. The History of Photovoltaics with Emphasis on CdTe Solar Cells and Modules. *Coatings 2020, Vol. 10, Page 344* **10**, 344 (2020).
9. Mishra, S., Ghosh, S. & Singh, T. Progress in Materials Development for Flexible Perovskite Solar Cells and Future Prospects. *ChemSusChem* **14**, 512–538 (2021).

10. Verduci, R. *et al.* Solar Energy in Space Applications: Review and Technology Perspectives. (2022) doi:10.1002/aenm.202200125.
11. Best Research-Cell Efficiency Chart | Photovoltaic Research | NREL. https://www.nrel.gov/pv/cell-efficiency.html.
12. Yang, T. Y., Kim, Y. Y. & Seo, J. Roll-to-roll manufacturing toward lab-to-fab-translation of perovskite solar cells. *APL Mater* **9**, 110901 (2021).
13. Li, H. *et al.* Recent progress towards roll-to-roll manufacturing of perovskite solar cells using slot-die processing. *Flexible and Printed Electronics* **5**, 014006 (2020).
14. Galagan, Y. Perovskite Solar Cells: Toward Industrial-Scale Methods. *Journal of Physical Chemistry Letters* **9**, 4326–4335 (2018).
15. Powell, R. C. Research Leading to High-Throughput Manufacturing of Thin-Film CdTe PV Modules: Annual Subcontract Report, September 2004--September 2005. (2004).
16. Schwambera, M. *et al.* 27.4: Modeling and Fabrication of Organic Vapor Phase Deposition (OVPD) Equipment for OLED Display Manufacturing. *SID Symposium Digest of Technical Papers* **33**, 894–897 (2002).
17. Sahli, F. *et al.* Vapor Transport Deposition of Methylammonium Iodide for Perovskite Solar Cells. *Cite This: ACS Appl. Energy Mater* **2021**, 4333–4343 (2021).
18. Wang, Y. *et al.* Recent progress in developing efficient monolithic all-perovskite tandem solar cells. *Journal of Semiconductors* **41**, 051201 (2020).
19. Fang, Z. *et al.* Perovskite-based tandem solar cells. *Sci Bull (Beijing)* **66**, 621–636 (2021).
20. Swartwout, R., Hoerantner, M. T. & Bulovi, V. Scalable Deposition Methods for Large-Area Production of Perovskite Thin Films. (2019) doi:10.1002/eem2.12043.
21. Lee, D. K. & Park, N. G. Materials and Methods for High-Efficiency Perovskite Solar Modules. *Solar RRL* **6**, (2022).

22. Wang, S. *et al.* Over 24% efficient MA-free CsxFA1−xPbX3 perovskite solar cells. *Joule* **6**, 1344–1356 (2022).
23. Li, H. *et al.* Sequential vacuum-evaporated perovskite solar cells with more than 24% efficiency. *Sci Adv* **8**, 7422 (2022).
24. Li, X. *et al.* A vacuum flash-assisted solution process for high-efficiency large-area perovskite solar cells. *Science (1979)* **353**, 58–62 (2016).
25. Higgins, M. *et al.* Solvent-free and large area compatible deposition of methylammonium lead bromide perovskite by close space sublimation and its application in PIN diodes. *Thin Solid Films* **692**, 137585 (2019).
26. Qiu, L., He, S., Jiang, Y. & Qi, Y. Metal halide perovskite solar cells by modified chemical vapor deposition. *J Mater Chem A Mater* **9**, 22759–22780 (2021).
27. Siegrist, S. *et al.* Triple-cation perovskite solar cells fabricated by a hybrid PVD/blade coating process using green solvents. *J Mater Chem A Mater* **9**, 26680–26687 (2021).
28. Gil-Escrig, L. *et al.* Vacuum Deposited Triple-Cation Mixed-Halide Perovskite Solar Cells. *Adv Energy Mater* **8**, (2018).
29. Li, J. *et al.* Highly Efficient Thermally Co-evaporated Perovskite Solar Cells and Mini-modules. *Joule* **4**, 1035–1053 (2020).
30. Momblona, C. *et al.* Efficient vacuum deposited p-i-n and n-i-p perovskite solar cells employing doped charge transport layers. *Energy Environ Sci* **9**, 3456–3463 (2016).
31. Shtein, M. Organic Vapor Phase Deposition and Vapor Jet Printing for Electronic and Optoelectronic Device Applications. (2004).
32. Qiu, L. *et al.* Scalable Fabrication of Stable High Efficiency Perovskite Solar Cells and Modules Utilizing Room Temperature Sputtered SnO2 Electron Transport Layer. *Adv Funct Mater* **29**, 1806779 (2019).

33. Persad, A. H. & Ward, C. A. Expressions for the Evaporation and Condensation Coefficients in the Hertz-Knudsen Relation. (2016).
34. Shtein, M., Gossenberger, H. F., Benziger, J. B. & Forrest, S. R. Material transport regimes and mechanisms for growth of molecular organic thin films using low-pressure organic vapor phase deposition. *J Appl Phys* **89**, 1470–1476 (2001).
35. Bergman, T., Lavine, A., Incropera, F. & Dewitt, D. *Fundamentals of Heat and Mass Transfer*. (John Wiley and Sons Inc, 2011).
36. Bird, R. B., Stewart, W. & Lightfoot, E. *Transport Phenomena*. (John Wiley and Sons Inc, 2007).
37. WHITEPAPER 2 Understanding Taylor Dispersion Analysis.
38. Taylor, G. Slowly through a Tube Dispersion of Soluble Matter in Solvent Flowing. (2010).
39. Aris, R. (University of M. On the dispersion of a solute in a fluid flowing through a tube. *Proceedings of the Royal Society A* **235**, (1956).
40. Salles, J., Thovert, J.-F. & Delannay, R. Taylor dispersion in porous media. Determination of the dispersion tensor. *Citation: Physics of Fluids A: Fluid Dynamics* **5**, 2348 (1993).
41. Cottet, H., Biron, J.-P. & Martin, M. Taylor Dispersion Analysis of Mixtures. (2007) doi:10.1021/ac071018w.
42. Balog, S. *et al.* Taylor dispersion of nanoparticles. *Journal of Nanoparticle Research* **19**, 1–11 (2017).
43. Borchert, J. *et al.* Impurity Tracking Enables Enhanced Control and Reproducibility of Hybrid Perovskite Vapor Deposition. *ACS Appl Mater Interfaces* **11**, 28851–28857 (2019).
44. Abzieher, T. *et al.* From Groundwork to Efficient Solar Cells: On the Importance of the Substrate Material in Co-Evaporated Perovskite Solar Cells. *Adv Funct Mater* **31**, (2021).

45. Kim, B. *et al.* Deposition Kinetics and Compositional Control of Vacuum Processed CH 3 NH 3 PbI 3 Perovskite.
46. *Handbook of Crystal Growth*. (Elsevier B.V., 2015).
47. Ratsch, C. & Venables, J. A. Microstructural evolution during film growth. *Journal of Vacuum Science & Technology B: Microelectronics Processing and Phenomena* **21**, 117 (2003).
48. Sleutel, M., Lutsko, J., Van Driessche, A. E. S., Durán-Olivencia, M. A. & Maes, D. Observing classical nucleation theory at work by monitoring phase transitions with molecular precision. *Nature Communications 2014 5:1* **5**, 1–8 (2014).
49. Kim, B.-S., Sessolo, M. & Bolink, H. J. Deposition Kinetics and Compositional Control of Vacuum-Processed CH 3 NH 3 PbI 3 Perovskite. (2020).
50. Burns, R. *et al.* Probing structure-property relationship in chemical vapor deposited hybrid perovskites by pressure and temperature. (1805) doi:10.1557/s43578-021-00229-y.
51. Lohmann, K. B. *et al.* Control over Crystal Size in Vapor Deposited Metal-Halide Perovskite Films. *ACS Energy Lett* **5**, 710–717 (2020).
52. CdTe solar cells: technology, operation and reliability. (2021).
53. Duan, L. & Uddin, A. Progress in Stability of Organic Solar Cells. *Advanced Science* **7**, 1903259 (2020).
54. Xue, R., Zhang, J., Li, Y. & Li, Y. Organic Solar Cell Materials toward Commercialization. *Small* **14**, 1801793 (2018).
55. Mora-Seró, I. Current Challenges in the Development of Quantum Dot Sensitized Solar Cells. *Adv Energy Mater* **10**, 2001774 (2020).
56. Zhao, Q. *et al.* Colloidal Quantum Dot Solar Cells: Progressive Deposition Techniques and Future Prospects on Large-Area Fabrication. *Advanced Materials* **34**, 2107888 (2022).

57. Webb, T. *et al.* Device Architecture Engineering: Progress toward Next Generation Perovskite Solar Cells. *Adv Funct Mater* **31**, 2103121 (2021).
58. Li, J. *et al.* Co-Evaporated MAPbI3 with Graded Fermi Levels Enables Highly Performing, Scalable, and Flexible p-i-n Perovskite Solar Cells. *Adv Funct Mater* **31**, 2103252 (2021).
59. Wang, R. *et al.* Prospects for metal halide perovskite-based tandem solar cells. *Nature Photonics 2021 15:6* **15**, 411–425 (2021).
60. Bartel, C. J. *et al.* New tolerance factor to predict the stability of perovskite oxides and halides. (2019).
61. Peña, M. A. & Fierro, J. L. G. Chemical Structures and Performance of Perovskite Oxides. (2001) doi:10.1021/cr980129f.
62. Li, X. *et al.* A-site perovskite oxides: an emerging functional material for electrocatalysis and photocatalysis †. (2021) doi:10.1039/d0ta09756j.
63. Fergus, J. W. Perovskite oxides for semiconductor-based gas sensors. *Sensors and Actuators B* **123**, 1169–1179 (2007).
64. Sun, C., Alonso, J. A. & Bian, J. Recent Advances in Perovskite-Type Oxides for Energy Conversion and Storage Applications. *Adv Energy Mater* **11**, (2021).
65. Kumar, N., Rani, J. & Kurchania, R. Advancement in CsPbBr3 inorganic perovskite solar cells: Fabrication, efficiency and stability. *Solar Energy* **221**, 197–205 (2021).
66. Xiang, W., Liu, S. & Tress, W. A review on the stability of inorganic metal halide perovskites: challenges and opportunities for stable solar cells. *Energy Environ Sci* **14**, 2090–2113 (2021).
67. Qiu, F.-Z., Li, M.-H., Qi, J.-J., Jiang, Y. & Hu, J.-S. Engineering inorganic lead halide perovskite deposition toward solar cells with efficiency approaching 20%. *Aggregate* **2**, 66–83 (2021).
68. Zhu, H. *et al.* Low-dimensional Sn-based perovskites: Evolution and future prospects of solar cells. *Chem* (2022).

69. Li, M. *et al.* Advances in Tin(II)-Based Perovskite Solar Cells: From Material Physics to Device Performance. *Small Struct* **3**, 2100102 (2022).
70. Xiang, H. *et al.* Towards highly stable and efficient planar perovskite solar cells: Materials development, defect control and interfacial engineering. *Chemical Engineering Journal* **420**, 127599 (2021).
71. Mohd Yusoff, A. R. bin *et al.* Passivation and process engineering approaches of halide perovskite films for high efficiency and stability perovskite solar cells. *Energy Environ Sci* **14**, 2906–2953 (2021).
72. Wu, T., Li, X., Qi, Y., Zhang, Y. & Han, L. Defect Passivation for Perovskite Solar Cells: from Molecule Design to Device Performance. *ChemSusChem* **14**, 4354–4376 (2021).
73. Pan, H., Shao, H. & Zhang, X. L. Interface engineering for high-efficiency perovskite solar cells COLLECTIONS ARTICLES YOU MAY BE INTERESTED IN. *J. Appl. Phys* **129**, 130904 (2021).
74. Byranvand, M. M. & Saliba, M. Charge carrier management for developing high-efficiency perovskite solar cells. *Matter* **4**, 1758–1759 (2021).
75. Li, Y., Xie, H., Lim, E. L., Hagfeldt, A. & Bi, D. Recent Progress of Critical Interface Engineering for Highly Efficient and Stable Perovskite Solar Cells. *Adv Energy Mater* **12**, (2022).
76. Mohd Yusoff, A. R. Bin *et al.* Passivation and process engineering approaches of halide perovskite films for high efficiency and stability perovskite solar cells. *Energy Environ Sci* **14**, 2906–2953 (2021).
77. Wu, G. *et al.* Surface Passivation Using 2D Perovskites toward Efficient and Stable Perovskite Solar Cells. *Advanced Materials* **34**, (2022).
78. Sai Ma *et al.* Development of encapsulation strategies towards the commercialization of perovskite solar cells. *Energy Environ Sci* **15**, 13–55 (2022).

79. Moody, N. *et al.* Assessing the Regulatory Requirements of Lead-Based Perovskite Photovoltaics. *Joule* **4**, 970–974 (2020).
80. Chen, S. *et al.* Preventing lead leakage with built-in resin layers for sustainable perovskite solar cells. *Nat Sustain* doi:10.1038/s41893-021-00701-x.
81. Niu, B. *et al.* 2021, 6, 3443−3449 ACS Energy Lett. 2021, 6, 3443−3449 Downloaded via MASSACHUSETTS INST OF TECHNOLOGY on. **21**, 35 (2022).
82. Li, X. *et al.* On-device lead-absorbing tapes for sustainable perovskite solar cells. *Nature Sustainability 2021 4:12* **4**, 1038–1041 (2021).
83. Vidal, R. *et al.* Assessing health and environmental impacts of solvents for producing perovskite solar cells. *Nat Sustain* doi:10.1038/s41893-020-00645-8.
84. Kim, H.-S. *et al.* Sustainable Green Process for Environmentally Viable Perovskite Solar Cells. *Cite This: ACS Energy Lett* **2022**, 1154–1177 (2022).
85. Li, D. *et al.* A Review on Scaling Up Perovskite Solar Cells. *Adv Funct Mater* **31**, (2021).
86. Yan, J., Savenije, T. J., Mazzarella, L. & Isabella, O. Progress and challenges on scaling up of perovskite solar cell technology. *Sustain Energy Fuels* **6**, 243–266 (2022).
87. Jean, J. *et al.* Radiative Efficiency Limit with Band Tailing Exceeds 30% for Quantum Dot Solar Cells. *ACS Energy Lett* **2**, 2616–2624 (2017).
88. Lee, J. W., Lee, D. K., Jeong, D. N. & Park, N. G. Control of Crystal Growth toward Scalable Fabrication of Perovskite Solar Cells. *Adv Funct Mater* **29**, (2019).
89. Choi, M. J. *et al.* Cascade surface modification of colloidal quantum dot inks enables efficient bulk homojunction photovoltaics. *Nat Commun* **11**, (2020).
90. Sun, B. *et al.* Ligand-assisted reconstruction of colloidal quantum dots decreases trap state density. *Nano Lett* **20**, 3694–3702 (2020).

91. Hu, L. *et al.* Optimizing Surface Chemistry of PbS Colloidal Quantum Dot for Highly Efficient and Stable Solar Cells via Chemical Binding. *Advanced Science* **8**, (2021).
92. Biondi, M. *et al.* A Chemically Orthogonal Hole Transport Layer for Efficient Colloidal Quantum Dot Solar Cells. *Advanced Materials* **32**, (2020).
93. Sukharevska, N. *et al.* Scalable PbS Quantum Dot Solar Cell Production by Blade Coating from Stable Inks. *Cite This: ACS Appl. Mater. Interfaces* **13**, 5207 (2021).
94. Fan, J. Z. *et al.* Micron Thick Colloidal Quantum Dot Solids. *Nano Lett* **20**, 5284–5291 (2020).
95. Cao, F. *et al.* High-Efficiency and Stable Quantum Dot Light-Emitting Diodes Enabled by a Solution-Processed Metal-Doped Nickel Oxide Hole Injection Interfacial Layer. *Adv Funct Mater* **27**, 1704278 (2017).
96. Widjonarko, N. E. *et al.* Sputtered nickel oxide thin film for efficient hole transport layer in polymer–fullerene bulk-heterojunction organic solar cell. *Thin Solid Films* **520**, 3813–3818 (2012).
97. Sajid, S. *et al.* Breakthroughs in NiOx-HTMs towards stable, low-cost and efficient perovskite solar cells. *Nano Energy* **51**, 408–424 (2018).
98. Hyun, B.-R., Choi, J. J., Seyler, K. L., Hanrath, T. & Wise, F. W. Heterojunction PbS Nanocrystal Solar Cells with Oxide Charge-Transport Layers. **18**, 36 (2022).
99. Liu, S. *et al.* Enhancing the Efficiency and Stability of PbS Quantum Dot Solar Cells through Engineering an Ultrathin NiO Nanocrystalline Interlayer. *ACS Appl Mater Interfaces* **12**, 46239–46246 (2020).
100. Wassweiler, E. Louise. Engineering scalable device architectures for lead sulfide quantum dot solar cells. (2019).
101. Li, J. *et al.* Passivation via atomic layer deposition Al2O3 for the performance enhancement of quantum dot photovoltaics. *Solar Energy Materials and Solar Cells* **209**, 1–6 (2020).

102. Chiang, K. K., Chen, J. S. & Wu, J. J. Aluminum electrode modulated bipolar resistive switching of Al/fuel-assisted NiO x/ITO memory devices modeled with a dual-oxygen-reservoir structure. *ACS Appl Mater Interfaces* **4**, 4237–4245 (2012).
103. Lee, C. B. *et al.* Effects of metal electrodes on the resistive memory switching property of NiO thin films. *Appl Phys Lett* **93**, 042115 (2008).
104. Yamanari, T., Taima, T., Sakai, J., Tsukamoto, J. & Yoshida, Y. Effect of buffer layers on stability of polymer-based organic solar cells. *Jpn J Appl Phys* **49**, 01AC02 (2010).
105. Wang, M. *et al.* Degradation mechanism of organic solar cells with aluminum cathode. *Solar Energy Materials and Solar Cells* **95**, 3303–3310 (2011).
106. Bush, K. A. *et al.* Thermal and Environmental Stability of Semi-Transparent Perovskite Solar Cells for Tandems Enabled by a Solution-Processed Nanoparticle Buffer Layer and Sputtered ITO Electrode. *Advanced Materials* **28**, 3937–3943 (2016).
107. Rong, Y. *et al.* Challenges for commercializing perovskite solar cells. *Science (1979)* **361**, (2018).
108. Turren-Cruz, S. H., Hagfeldt, A. & Saliba, M. Methylammonium-free, high-performance, and stable perovskite solar cells on a planar architecture. *Science (1979)* **362**, 449–453 (2018).
109. Lai, W. C. *et al.* Conversion efficiency enhancement of methylammonium lead triiodide perovskite solar cells converted from thermally deposited lead iodide via thin methylammonium iodide interlayer. *Org Electron* **82**, (2020).
110. Hawash, Z. *et al.* Interfacial Modification of Perovskite Solar Cells Using an Ultrathin MAI Layer Leads to Enhanced Energy Level Alignment, Efficiencies, and Reproducibility. *J. Phys. Chem. Lett* **8**, 45 (2017).

111. Wang, R. *et al.* Surface CH 3 NH 3+ to CH 3+ Ratio Impacts the Work Function of Solution-Processed and Vacuum-Sublimed CH 3 NH 3 PbI 3 Thin Films. *Adv Mater Interfaces* **6**, (2019).
112. Patel, J. B., Milot, R. L., Wright, A. D., Herz, L. M. & Johnston, M. B. Formation Dynamics of CH3NH3PbI3 Perovskite Following Two-Step Layer Deposition. *Journal of Physical Chemistry Letters* **7**, 96–102 (2016).
113. Toloueinia, P. *et al.* Moisture-Induced Structural Degradation in Methylammonium Lead Iodide Perovskite Thin Films. (2020) doi:10.1021/acsaem.0c00638.
114. A Leguy, A. M. *et al.* Reversible Hydration of CH 3 NH 3 PbI 3 in Films, Single Crystals, and Solar Cells. (2015).
115. Dunfield, S. P. *et al.* From Defects to Degradation: A Mechanistic Understanding of Degradation in Perovskite Solar Cell Devices and Modules. (2020) doi:10.1002/aenm.201904054.
116. Guesnay, Q., Sahli, F., Ballif, C. & Jeangros, Q. Vapor deposition of metal halide perovskite thin films: Process control strategies to shape layer properties. *APL Mater* **9**, (2021).
117. Phys, A. & He, S. Perovskite solar cells by vapor deposition based and assisted methods Perovskite solar cells by vapor deposition based and assisted methods. **021305**, (2022).
118. Juarez-Perez, E. J., Hawash, Z., Raga, S. R., Ono, L. K. & Qi, Y. Thermal degradation of CH 3 NH 3 PbI 3 perovskite into NH 3 and CH 3 I gases observed by coupled thermogravimetry–mass spectrometry analysis. *Energy Environ Sci* **9**, 3406–3410 (2016).
119. Dualeh, A., Gao, P., Seok, S. Il, Khaja Nazeeruddin, M. & Grä¨, M. Thermal Behavior of Methylammonium Lead-Trihalide Perovskite Photovoltaic Light Harvesters. (2014).

120. Latini, A., Gigli, G. & Ciccioli, A. A study on the nature of the thermal decomposition of methylammonium lead iodide perovskite, CH 3 NH 3 PbI 3 : an attempt to rationalise contradictory experimental results. *Sustain Energy Fuels* **1**, 1351–1357 (2017).
121. Levchuk, I. *et al.* Deciphering the Role of Impurities in Methylammonium Iodide and Their Impact on the Performance of Perovskite Solar Cells. *Adv Mater Interfaces* **3**, (2016).
122. Igual-Muñoz, A. M. *et al.* Room-Temperature Vacuum Deposition of CsPbI2Br Perovskite Films from Multiple Sources and Mixed Halide Precursors. *Chemistry of Materials* **32**, 8641–8652 (2020).
123. Acik, M. *et al.* Substitutional Growth of Methylammonium Lead Iodide Perovskites in Alcohols. *Adv Energy Mater* **8**, 1–14 (2018).
124. Chen, H. *et al.* A solvent- and vacuum-free route to large-area perovskite films for efficient solar modules. (2017) doi:10.1038/nature23877.
125. Bækbo, M. J., Hansen, O., Chorkendorff, I. & Vesborg, P. C. K. Deposition of methylammonium iodide: Via evaporation-combined kinetic and mass spectrometric study. *RSC Adv* **8**, 29899–29908 (2018).
126. Palazon, F. *et al.* Room-Temperature Cubic Phase Crystallization and High Stability of Vacuum-Deposited Methylammonium Lead Triiodide Thin Films for High-Efficiency Solar Cells. *Advanced Materials* **31**, 1–6 (2019).
127. Raiford, J. A., Oyakhire, S. T. & Bent, S. F. Applications of atomic layer deposition and chemical vapor deposition for perovskite solar cells. *Energy Environ Sci* **13**, 1997–2023 (2020).
128. Zhang, H., Nazeeruddin, M. K. & Choy, W. C. H. Perovskite Photovoltaics: The Significant Role of Ligands in Film Formation, Passivation, and Stability. *Advanced Materials* **31**, 1805702 (2019).

129. Chiang, Y. H., Anaya, M. & Stranks, S. D. Multisource Vacuum Deposition of Methylammonium-Free Perovskite Solar Cells. *ACS Energy Lett* **5**, 2498–2504 (2020).
130. Feng, J. *et al.* High-throughput large-area vacuum deposition for high-performance formamidine-based perovskite solar cells. *Energy Environ Sci* **14**, 3035–3043 (2021).
131. La-Placa, M.-G. *et al.* Vacuum-Deposited 2D/3D Perovskite Heterojunctions. **22**, 18 (2022).
132. Su, T. sen *et al.* Characterization on Highly Efficient Perovskite Solar Cells Made from One-Step and Two-Step Solution Processes. *Solar RRL* **5**, (2021).
133. Toloueinia, P. *et al.* Moisture-Induced Structural Degradation in Methylammonium Lead Iodide Perovskite Thin Films. *ACS Appl Energy Mater* **3**, 8240–8248 (2020).
134. Qu, B. *et al.* Fast organic vapor phase deposition of thin films in light-emitting diodes. *ACS Nano* **14**, 14157–14163 (2020).
135. Yang, F., Shtein, M. & Forrest, S. R. Morphology control and material mixing by high-temperature organic vapor-phase deposition and its application to thin-film solar cells. *J Appl Phys* **98**, (2005).
136. Qu, B. & Forrest, S. R. Continuous roll-to-roll fabrication of organic photovoltaic cells via interconnected high-vacuum and low-pressure organic vapor phase deposition systems. *Appl Phys Lett* **113**, 053302 (2018).
137. Oklobia, O. *et al.* Development of arsenic doped Cd(Se,Te) absorbers by MOCVD for thin film solar cells. *Solar Energy Materials and Solar Cells* **231**, 111325 (2021).
138. Teloeken, A. C., Lamb, D. A., Dunlop, T. O. & Irvine, S. J. C. Effect of bending test on the performance of CdTe solar cells on flexible ultra-thin glass produced by MOCVD. *Solar Energy Materials and Solar Cells* **211**, 110552 (2020).
139. Chmielewski, D. J. *et al.* High Performance Metamorphic Tunnel Junctions for GaAsP/Si Tandem Solar Cells Grown via MOCVD. *2018 IEEE 7th World Conference*

on Photovoltaic Energy Conversion, WCPEC 2018 - A Joint Conference of 45th IEEE PVSC, 28th PVSEC and 34th EU PVSEC 2631–2634 (2018).

140. Hoerantner, M. T. *et al.* High-Speed Vapor Transport Deposition of Perovskite Thin Films. *ACS Appl Mater Interfaces* **11**, 32928–32936 (2019).
141. Ávila, J., Momblona, C., Boix, P. P., Sessolo, M. & Bolink, H. J. Vapor-Deposited Perovskites: The Route to High-Performance Solar Cell Production? *Joule* **1**, 431–442 (2017).
142. Kim, B.-S., Choi, M.-H., Choi, M.-S. & Kim, J.-J. Composition-controlled organometal halide perovskite via CH 3 NH 3 I pressure in a vacuum co-deposition process †. (2016) doi:10.1039/c6ta00168h.
143. Frankel, G. S., Chen, X.-B., Gupta, R. K., Kandasamy, S. & Birbilis, N. Effect of Vacuum System Base Pressure on Corrosion Resistance of Sputtered Al Thin Films. *J Electrochem Soc* **161**, C195–C200 (2014).
144. Smyth, C. M., Addou, R., McDonnell, S., Hinkle, C. L. & Wallace, R. M. WSe2-contact metal interface chemistry and band alignment under high vacuum and ultra high vacuum deposition conditions. *2d Mater* **4**, 025084 (2017).
145. Zhou, Y. *et al.* Millimeter-Size All-inorganic Perovskite Crystalline Thin Film Grown by Chemical Vapor Deposition. *Adv Funct Mater* **31**, 2101058 (2021).
146. Harding, A. J. *et al.* Towards Perovskite Vapor Transport Deposition: PbI2Deposition and Modeling in a Close Space Vapor Transport Configuration. *Conference Record of the IEEE Photovoltaic Specialists Conference* 982–985 (2021) doi:10.1109/PVSC43889.2021.9519001.
147. Moser, T. *et al.* Revealing the perovskite formation kinetics during chemical vapour deposition. *J Mater Chem A Mater* **8**, 21973–21982 (2020).
148. Ngqoloda, S. *et al.* Air-Stable Hybrid Perovskite Solar Cell by Sequential Vapor Deposition in a Single Reactor. *ACS Appl Energy Mater* **3**, 2350–2359 (2020).

149. Sahli, F. *et al.* Vapor Transport Deposition of Methylammonium Iodide for Perovskite Solar Cells. *ACS Appl Energy Mater* **4**, 4333–4343 (2021).
150. Patel, J. B. *et al.* Influence of Interface Morphology on Hysteresis in Vapor-Deposited Perovskite Solar Cells. *Adv Electron Mater* **3**, 1600470 (2017).
151. Poindexter, J. R. *et al.* Distribution and Charge State of Iron Impurities in Intentionally Contaminated Lead Halide Perovskites; Distribution and Charge State of Iron Impurities in Intentionally Contaminated Lead Halide Perovskites. *IEEE J Photovolt* **8**, (2018).
152. Kam, M. *et al.* Efficient Mixed-Cation Mixed-Halide Perovskite Solar Cells by All-Vacuum Sequential Deposition Using Metal Oxide Electron Transport Layer. *Solar RRL* **3**, (2019).
153. Harding, A. J. *et al.* The growth of methylammonium lead iodide perovskites by close space vapor transport. (2020) doi:10.1039/d0ra01640c.
154. Kim, G. *et al.* Perovskite Pattern Formation by Chemical Vapor Deposition Using Photolithographically Defined Templates. *Chemistry of Materials* **31**, 8212–8221 (2019).
155. Gil-Escrig, L. *et al.* Fully Vacuum-Processed Perovskite Solar Cells on Pyramidal Microtextures. *Solar RRL* **5**, (2021).
156. Li, J. *et al.* Co-Evaporated MAPbI3 with Graded Fermi Levels Enables Highly Performing, Scalable, and Flexible p-i-n Perovskite Solar Cells. *Adv Funct Mater* **31**, (2021).
157. Roß, M. *et al.* Co-Evaporated p-i-n Perovskite Solar Cells beyond 20% Efficiency: Impact of Substrate Temperature and Hole-Transport Layer. *ACS Appl Mater Interfaces* **12**, 39261–39272 (2020).
158. Gallet, T. *et al.* Co-evaporation of CH3NH3PbI3: How growth conditions impact phase purity, photostriction, and intrinsic stability. *ACS Appl Mater Interfaces* **13**, 2642–2653 (2021).

159. Dreessen, C. *et al.* Efficient Vacuum-Deposited Perovskite Solar Cells with Stable Cubic FA 1−x MA x PbI 3. **14**, 51 (2022).
160. Gil-Escrig, L. *et al.* Efficient vacuum-deposited perovskite solar cells with stable cubic FA1- xMAxPbI3. *ACS Energy Lett* **5**, 3053–3061 (2020).
161. Ratnasingham, S. R. *et al.* Novel scalable aerosol-assisted CVD route for perovskite solar cells † ‡. doi:10.1039/d0ma00906g.
162. Wang, M. & Carmalt, C. J. Film Fabrication of Perovskites and their Derivatives for Photovoltaic Applications via Chemical Vapor Deposition. *ACS Appl Energy Mater* (2021).
163. Abzieher, T. *et al.* Efficient All-Evaporated <italic>pin</italic>-Perovskite Solar Cells: A Promising Approach Toward Industrial Large-Scale Fabrication; Efficient All-Evaporated <italic>pin</italic>-Perovskite Solar Cells: A Promising Approach Toward Industrial Large-Scale Fabrication. *IEEE J Photovolt* **9**, 1249 (2019).
164. Clark, C. P., Voigt, B., Aydil, E. S. & Holmes, R. J. Carrier-gas assisted vapor deposition for highly tunable morphology of halide perovskite thin films. *Sustain Energy Fuels* **3**, 2447–2455 (2019).
165. Guesnay, Q. & Sahli, F. Vapor deposition of metal halide perovskite thin films : Process control strategies to shape layer properties Vapor deposition of metal halide perovskite thin films : Process control strategies to shape layer properties. **100703**, (2021).
166. Ng, A. *et al.* Crystal Engineering for Low Defect Density and High Efficiency Hybrid Chemical Vapor Deposition Grown Perovskite Solar Cells. *ACS Appl Mater Interfaces* **8**, 32805–32814 (2016).
167. Wittich, C. *et al.* Structural and compositional characteristics of vacuum deposited methylammonium lead halide perovskite layers in dependence on background pressure and substrate temperature. *Thin Solid Films* **650**, 51–57 (2018).

168. Kim, B. S., Gil-Escrig, L., Sessolo, M. & Bolink, H. J. Deposition Kinetics and Compositional Control of Vacuum-Processed CH3NH3PbI3Perovskite. *Journal of Physical Chemistry Letters* **11**, 6852–6859 (2020).
169. Heinze, K. L. *et al.* Importance of methylammonium iodide partial pressure and evaporation onset for the growth of co-evaporated methylammonium lead iodide absorbers. *Scientific Reports* | **11**, 15299 (123AD).
170. Arivazhagan, V. *et al.* Vacuum co-deposited CH3NH3PbI3 films by controlling vapor pressure for efficient planar perovskite solar cells. *Solar Energy* **181**, 339–344 (2019).
171. Roß, M., Stutz, M. B. & Albrecht, S. Revealing the Role of Methylammonium Iodide Purity on the Vapor-Phase Deposition Process of Perovskites. *Solar RRL* (2022) doi:10.1002/SOLR.202200500.
172. Moser, T. *et al.* Revealing the perovskite formation kinetics during chemical vapour deposition. *J Mater Chem A Mater* **8**, 21973–21982 (2020).
173. Shtein, M., Gossenberger, H. F., Benziger, J. B. & Forrest, S. R. Material transport regimes and mechanisms for growth of molecular organic thin films using low-pressure organic vapor phase deposition. *J Appl Phys* **89**, 1470 (2000).
174. Ioakeimidis, A., Christodoulou, C., Lux-Steiner, M. & Fostiropoulos, K. Effect of PbI2 deposition rate on two-step PVD/CVD all-vacuum prepared perovskite. *J Solid State Chem* **244**, 20–24 (2016).
175. Ngqoloda, S., Arendse, C. J., Muller, T. F., Magubane, S. S. & Oliphant, C. J. Controlled Deposition of Lead Iodide and Lead Chloride Thin Films by Low-Pressure Chemical Vapor Deposition. *Coatings 2020, Vol. 10, Page 1208* **10**, 1208 (2020).
176. Li, Z. *et al.* Surface-Orientation Elimination of Vapor-Deposited PbI2Flakes for Efficient Perovskite Synthesis on Curved Solar Cells. *ACS Appl Mater Interfaces* **13**, 45496–45504 (2021).

177. Koffman-Frischknecht, A. *et al.* Tuning morphological features of lead iodide by low pressure vapor phase deposition. *Thin Solid Films* **653**, 249–257 (2018).
178. Brenner, T. M. *et al.* Conversion of single crystalline PbI2 to CH3NH3PbI3: Structural relations and transformation dynamics. *Chemistry of Materials* **28**, 6501–6510 (2016).
179. Alberti, A. *et al.* Pb clustering and PbI 2 nanofragmentation during methylammonium lead iodide perovskite degradation. doi:10.1038/s41467-019-09909-0.
180. Le Corre, V. M. *et al.* Charge Transport Layers Limiting the Efficiency of Perovskite Solar Cells: How to Optimize Conductivity, Doping, and Thickness. *ACS Appl Energy Mater* **2**, 6280–6287 (2019).
181. Olthof, S. & Meerholz, K. Substrate-dependent electronic structure and film formation of MAPbI 3 perovskites. *Sci Rep* **7**, 1–10 (2017).
182. Momblona, C. *et al.* Efficient vacuum deposited p-i-n and n-i-p perovskite solar cells employing doped charge transport layers. *Energy Environ Sci* **9**, 3456–3463 (2016).
183. Roß, M. *et al.* Co-Evaporated p-i-n Perovskite Solar Cells beyond 20% Efficiency: Impact of Substrate Temperature and Hole-Transport Layer. *Cite This: ACS Appl. Mater. Interfaces* **12**, 39261–39272 (2020).
184. Kam, M., Zhang, Q., Zhang, D. & Fan, Z. Room-temperature sputtered sno 2 as Robust electron transport Layer for Air-Stable and Efficient perovskite solar Cells on Rigid and Flexible substrates. doi:10.1038/s41598-019-42962-9.
185. Qiu, L. *et al.* Rapid hybrid chemical vapor deposition for efficient and hysteresis-free perovskite solar modules with an operation lifetime exceeding 800 hours †. (2020) doi:10.1039/d0ta09007g.
186. Pérez-Del-Rey, D., Boix, P. P., Sessolo, M., Hadipour, A. & Bolink, H. J. Interfacial Modification for High-Efficiency Vapor-Phase-Deposited Perovskite Solar Cells

Based on a Metal Oxide Buffer Layer. *Journal of Physical Chemistry Letters* **9**, 1041–1046 (2018).

187. Rueda-Delgado, D. *et al.* Solution-processed and evaporated C60 interlayers for improved charge transport in perovskite photovoltaics. *Org Electron* **77**, 105526 (2020).
188. Klipfel, N. *et al.* C60 Thin Films in Perovskite Solar Cells: Efficient or Limiting Charge Transport Layer? *ACS Appl Energy Mater* **5**, 1646–1655 (2022).
189. Liu, D. *et al.* Impact of Ultrathin C60 on Perovskite Photovoltaic Devices. *ACS Nano* **12**, 876–883 (2018).
190. Wu, T., Li, X., Qi, Y., Zhang, Y. & Han, L. Defect Passivation for Perovskite Solar Cells: from Molecule Design to Device Performance. *ChemSusChem* **14**, 4354–4376 (2021).
191. Wang, R. *et al.* Constructive molecular configurations for surface-defect passivation of perovskite photovoltaics. *Science (1979)* **366**, 1509–1513 (2019).
192. Zhou, Z. *et al.* Methylamine-Gas-Induced Defect-Healing Behavior of CH 3 NH 3 PbI 3 Thin Films for Perovskite Solar Cells . *Angewandte Chemie* **127**, 9841–9845 (2015).
193. Hao, L., Zhao, Q., Wang, X., Pang, S. & Cui, G. Methylamine gas healing of perovskite films: a short review and perspective. *J Mater Chem C Mater* **10**, 2390–2399 (2022).
194. Schlipf, J. *et al.* Top-Down Approaches Towards Single Crystal Perovskite Solar Cells. *Scientific Reports 2018 8:1* **8**, 1–8 (2018).
195. Ávila, J., Momblona, C., Boix, P. P., Sessolo, M. & Bolink, H. J. Vapor-Deposited Perovskites: The Route to High-Performance Solar Cell Production? *Joule* **1**, 431–442 (2017).

196. Borchert, J. *et al.* Structural investigation of co-evaporated methyl ammonium lead halide perovskite films during growth and thermal decomposition using different PbX2 (X = I, Cl) precursors. *J Mater Chem A Mater* **3**, 19842–19849 (2015).
197. Patel, J. B. *et al.* Influence of Interface Morphology on Hysteresis in Vapor-Deposited Perovskite Solar Cells. *Adv Electron Mater* **3**, 1600470 (2017).
198. Hines, M. A. & Scholes, G. D. Colloidal PbS Nanocrystals with Size-Tunable Near-Infrared Emission: Observation of Post-Synthesis Self-Narrowing of the Particle Size Distribution. *Advanced Materials* **15**, 1844–1849 (2003).
199. Liu, L., McLeod, J. A., Wang, R., Shen, P. & Duhm, S. Tracking the formation of methylammonium lead triiodide perovskite. *Appl Phys Lett* **107**, 061904 (2015).
200. Raga, S. R. *et al.* Influence of air annealing on high efficiency planar structure perovskite solar cells. *Chemistry of Materials* **27**, 1597–1603 (2015).
201. Wang, Q. K. *et al.* Energy Level Offsets at Lead Halide Perovskite/Organic Hybrid Interfaces and Their Impacts on Charge Separation. *Adv Mater Interfaces* **2**, 1400528 (2015).